CRANFIELD UNIVERSITY

LUIS PALAFOX GÁMIR

A NEW METHOD FOR THE DETERMINATION OF THE ENTRY POSITION OF γ-RAYS IN HIGH PURITY GERMANIUM DETECTORS BY CURRENT PULSE ANALYSIS

COLLEGE OF AERONAUTICS

PhD THESIS

CRANFIELD UNIVERSITY

COLLEGE OF AERONAUTICS
DEPARTMENT OF ELECTRONIC SYSTEM DESIGN

PhD Thesis

Academic Year 1996-1997

Luis Palafox Gámir

A NEW METHOD FOR THE DETERMINATION OF THE ENTRY POSITION OF γ-RAYS IN HIGH PURITY GERMANIUM DETECTORS BY CURRENT PULSE ANALYSIS

Supervisor: Dr. D. D. Russell

August 1997

This thesis is submitted in partial fulfillment of the
requirements for the Degree of Doctor of Philosopy

Acknowledgements

This work was in part financed by a scholarship from the Spanish Ministerio de Educación y Ciencia and by a guest scholarship from the Max-Planck-Gesellschaft zur Förderung der Wissenschaft.

I wish to thank Dr. D. D. Russell for the supervision of this thesis. I am obliged to Cranfield University for promoting the collaboration under which this work has been carried out. I thank Prof. Dr. Dirk Schwalm for offering me this challenging project and for his unstinting support. I consider it an honour to have been given the opportunity of working in the CB group at the Max-Planck-Institut für Kernphysik under such stimulating conditions.

I also wish to thank Dr. Berta Rubio and Dr. José Luis Taín for their assistance in the selection of a collaborating institution for this work. The fact that the **steepest slope** method originated after I made a presentation of my work at IFIC Valencia should not be left unmentioned.

I also wish to particularly thank the members of the CB group during my time at MPI. They were always available for discussions and provided additional motivation to improve my work. I am indebted to Christoph Gund, Frank Köck and Thomas Härtlein for their help in setting up the measurements. I must acknowledge Peter Thirolf for his suggestion that the preamplifier be further developed by the Cologne nuclear electronics group while I devoted my time to writing this thesis.

I must also thank the staff at MPI and in particular those in the MPI electronics workshop, especially Manfred Hornung. I am also indebted to Thomas Schiffmann, Peter Werle and Oliver Koschorreck, whose benches and equipment I used so many times during the development of electronic circuits. Their expertise and suggestions were invaluable in overcoming the many small difficulties unavoidable when developing a low noise, discrete transistor circuit and the corresponding enclosure.

I especially thank Dirk Schwalm, Dr. D. D. Russell, John Fitzgerald, Dirk Pansegrau, Astrid Dietrich, Javier Calpe and Christoph Gund for their thoroughness in reading the manuscript of this thesis; their comments have made this text much easier to understand.

Last but by no means least, thanks to all the members of my family and my friends; without their support, this work would have never been completed.

Abstract

A new method for determining the entry point of γ-rays in closed ended HPGe detectors has been developed. Exploiting the position dependence shown by the current pulses generated when a γ-ray interacts with the detector, it is possible to electronically divide the crystal in the radial coordinate and thus increase the effective granularity of the detector.

Position resolution is particularly important for correcting the Doppler peak broadening observed in many in-beam γ-spectroscopy experiments. Position resolution within coaxial crystals is accomplished by combining the angular information gained by segmenting the outer contact with the determination of the event radius by current pulse shape analysis.

With increasing γ-energy, more than one interaction is in general required to completely stop a γ-ray in a germanium detector. The concept of a *main interaction,* defined as that depositing the largest fraction of the original γ-energy, is introduced and seen to be the dominant contribution to the event current pulses. A Monte Carlo simulation for the positions and energies of the interactions in an event has been performed in order to establish the physical limits for the position resolution that can be measured in a segmented CLUSTER module. A varying fraction of events, from 55% at a γ-energy of 400 keV to 85% at 1800 keV, have their main interaction within 5 mm from the entry point. The position of the main interaction can therefore be successfully used to measure the entry position of the γ-ray in the detector.

In order to provide high quality charge/energy and current outputs from the detector signal, a new preamplifier for large volume HPGe detectors has been developed. The intrinsic equivalent noise contribution from the preamplifier was measured at 0.65 keV + 35 eV/pF. The measured energy resolution when the input FET is operated at cryogenic temperature is 2.30 keV at 1333 keV with 3 μs shaping time.

Using this preamplifier and the first prototype of a two-fold segmented CLUSTER module, a radial resolution of ±4 mm has been measured with the new method both at 662 and 1333 keV. The method can be incorporated into an analogue electronic circuit and is therefore directly applicable in in-beam γ-spectroscopy experiments.

Contents

List of Figures

List of Tables

Chapter 1

Introduction

High Purity germanium (HPGe) detectors have been used in γ-ray spectroscopy in the last thirty years to measure the properties of photons emitted in nuclear processes. There are three basic parameters for every detection: the γ-energy, the instant in time when the detection has been made and the direction under which the γ-ray has been emitted. For in-beam nuclear physics experiments, where a beam of accelerated ions is aimed at a target in order to study selected nuclear processes between the accelerated ions and the nuclei present in the target, detectors are arranged pointing to the target position. Whenever the trajectory and the decay time of the emitting nucleus can be measured or the γ-rays can be assumed to be emitted very close to the target (typically within a couple of millimeters), the γ-trajectory can be reconstructed dependent on knowledge of the entry position of the γ-ray in the detector.

If the position of the γ-interaction within the detector cannot be determined, the uncertainty in the detection angles is only limited by the solid angle covered by the detector. Position resolution is important for measuring the angular distribution of the emitted γ-rays. It is even more relevant for the main application of the method developed in this thesis, the correction of the Doppler shift in the observed γ-energy.

When a nucleus travels at velocity $\beta = v/c$, where c is the velocity of light in vacuum, the observed energy E_γ in the laboratory reference system of a γ-ray emitted by a nucleus is subjected to a Doppler shift according to

$$E_\gamma = E_{\gamma_0}\sqrt{1-\beta^2}\frac{1}{1-\beta\cos\theta_\gamma}, \tag{1.1}$$

where E_{γ_0} is the energy in the rest reference system of the nucleus and θ_γ is the emission angle relative to the trajectory of the nucleus in the laboratory reference system. Thus, for a given detector opening angle $\Delta\theta_\gamma$, the observed γ-energy shows an energy broadening ΔE_γ according to

$$\frac{\Delta E_\gamma}{E_\gamma} = \frac{\beta\sin\theta_\gamma}{1-\beta\cos\theta_\gamma}\Delta\theta_\gamma\ . \tag{1.2}$$

Note that, for $\beta \ll 1$, the largest Doppler broadening occurs at $\theta_\gamma = 90°$. From Fig. 1.1, $\Delta\theta_\gamma = 2\arctan\frac{\mathrm{R}}{\mathrm{D}}$. As the granularity of the γ-array increases, $\Delta\theta_\gamma$ decreases and with it the Doppler broadening ΔE_γ. Detector elements with smaller frontal surfaces increase the granularity, but the volume of each element is accordingly reduced and hence also the full-energy detection efficiency.

A new, high efficiency germanium detector array covering a solid angle of almost 4π, MINIBALL [Ebe97], is currently being developed in order to perform γ-spectroscopic studies with radioactive beams and rare γ-decay measurements. The detectors being developed for MINIBALL are based on encapsulated CLUSTER modules, which were developed for the EUROBALL CLUSTER composite detector [Tho95]. In a EUROBALL CLUSTER, seven of these modules are placed in a very compact packaging in order to increase the full-energy detection efficiency at medium and high γ-energies. The CLUSTER composite detectors have been successfully employed in different γ-ray spectroscopy experiments since Autumn 1994.

Since the detection efficiency in these types of experiments is even more important than in previous 4π γ-spectroscopy germanium arrays like EUROBALL

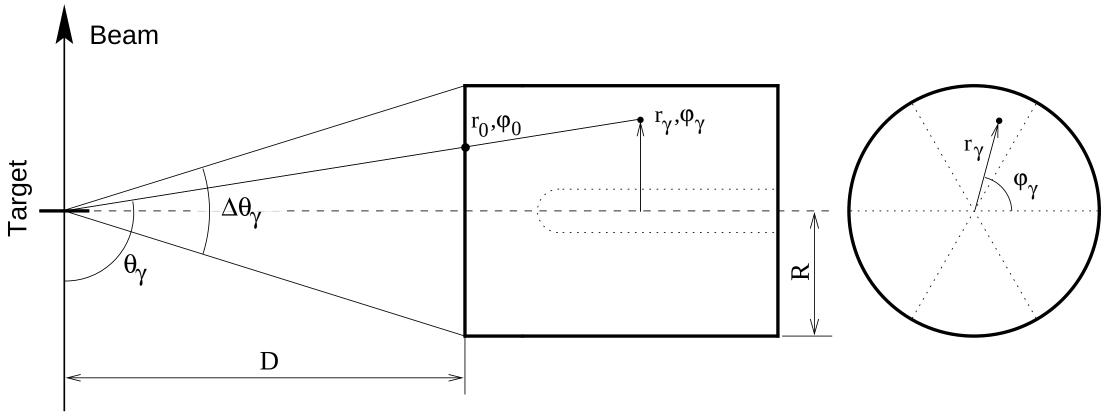

Figure 1.1: Schematic diagram illustrating the various geometric quantities used to describe the orientation of the detector and the γ-ray. The interaction point $(r_\gamma, \varphi_\gamma)$ of the γ-ray is expressed in the detector fixed coordinate system, using cylindrical coordinates.

[Eur92], the germanium crystals will be placed close to the target (D $\simeq$ 100 mm) in order to optimise the solid angle covered by germanium detectors. The granularity of MINIBALL is therefore considerably lower than that of EUROBALL (D = 430 mm) and Doppler broadening will become the dominant contribution to the energy resolution for many of the planned experiments if a sufficient granularity of the CLUSTER module itself cannot be regained.

For typical values, $\beta = 0.045$ and R/D = 0.35, the energy resolution for $\theta_\gamma = 90°$ is degraded from the intrinsic $\sim$ 2.5 keV to some 15 keV at $E_{\gamma 0} = 1333$ keV[1], and from $\sim$ 1.8 keV to 4.0 keV at $E_{\gamma 0} = 356$ keV, which would be intolerable for most spectroscopic measurements.

In order to re-establish a reasonable granularity when using large volume crystals at small detector-target distances, it is necessary to divide each crystal

---

[1] The 1332.502 keV line corresponds to the lower γ-transition in the ^{60}Co decay and is widely used as the reference energy for quoting the energy resolution of large volume γ-ray detectors and associated electronic circuits.

into subvolumes. The six-fold segmentation of the outer electrical contact for the encapsulated CLUSTER crystals is currently being developed to enable the determination of the entry angle φ_0 (cf. Fig. 1.1) of the γ-ray in the detector, once the orientation of the detector relative to the beam axis is known. The granularity of the instrument can be further increased, hence reducing $\Delta\theta_\gamma$, by determining the entry radius r_0 of the γ-ray in the crystal. This radial segmentation can be performed electronically by exploiting the dependence of the shape of the current pulses generated on the distance of the γ-interaction from the central electrode of the detector. No position resolution along the depth of the detector is foreseen; in many applications, however, it is sufficient to perform the Doppler correction using the projection of the measured position $(r_\gamma, \varphi_\gamma)$ on the frontal surface of the detector (r_0, φ_0).

The main subject of this thesis is the determination of the radius r_γ where γ-rays undergo their first interaction in germanium detectors. A Doppler correction can be performed with this information in in-beam experiments. As will be seen in chapter 2, more than one interaction is in general required in order to completely stop a γ-ray in a germanium crystal for most of the γ-energy range of interest. Although the γ-direction is defined by the position of the first interaction, in general only the position of the interaction that deposits the largest fraction of the initial γ-energy, the *main interaction*, can be determined. A thorough Monte Carlo simulation has been performed for the positions and energies of the different interactions in an event in order to investigate the position resolution that can be achieved in a CLUSTER module by determining the position of the main interaction.

The current pulse corresponding to each detector event has been calculated by combining the results of the Monte Carlo simulation with the numerical solution of the electric field in a CLUSTER crystal, as reported in chapter 3. These calculated current pulses have been processed according to different approaches for determining the entry radius of the γ-ray. Previous methods [Str72, She74, Sch92, Esc94, Krö96] have concentrated on low energies, where Doppler correction improves the measured energy resolution less than at energies around 1 MeV. A new method, the *steepest slope method*, has been developed in this thesis in order to determine the γ entry radius by measuring the time that the majority charge carriers liberated by the main interaction take to reach the central electrical contact in the detector. This drift time can be measured by analysing the shape of the event current pulse. In chapter 4, the results from the calculated event current pulses are used to evaluate the applicability of each method to in-beam experiments.

In order to study the event current pulses in detail, a new preamplifier has been designed as part of this project and is reported in chapter 5 and appendix A. In addition to the traditional "charge/energy" output, a "current" signal (both voltage waveforms) is produced, reflecting the current signal originally generated by the germanium detector. Position resolution is the main subject of this thesis but this additional information will also be used to optimise the energy resolution of the germanium detector. The "current" signal must therefore be extracted without compromising the performance at the "charge/energy" output.

In order to retain maximum flexibility for the evaluation of the different radial determination algorithms that can be employed for in-beam experiments, the event current pulses of a CLUSTER module were sampled with an 8 bit, 250 MHz flash analogue to digital converter and stored together with a 13 bit measurement of the corresponding γ-energy. As reported in chapter 6, the measurements with the steepest slope method show good agreement with the expected results and provide a robust measurement of the entry radius of γ-rays in large volume, coaxial high purity germanium detectors.

Any radial determination method should not compromise the detection rate capability of the detector. The statistical time distribution of valid events in

γ-spectroscopy experiments means that the data acquisition system that stores the relevant parameters has to achieve the highest possible event throughput. Sampling the current pulses, as done in the present test stages, and storing them for subsequent analysis is therefore impractical due to the increase in event data. For the same reasons, computer intensive methods can only be incorporated if dedicated hardware is developed. Ideally, the entry radius should be determined, simultaneously to the γ-energy, resulting in only one additional parameter for each detector in an event. As discussed in the conclusions (chapter 7), the steepest slope method is well suited to an analogue implementation that would provide simultaneously to the measurement of the γ-energy a signal that is directly proportional to the entry radius.

Chapter 2

HPGe γ-ray Detectors

Semiconductors have become the materials of choice for high resolution spectroscopy of charged particles and γ-rays. In particular, germanium offers one of the highest energy resolutions for γ-ray spectroscopy at energies between 1 keV and 10 MeV. This chapter covers the detection process of a γ-ray in a semiconductor crystal and the resulting electrical output and will present the advantages of germanium as a detector material.

The different possible interaction mechanisms that a γ-ray in the energy range from a few tens of keV to a few MeV can undergo in solid state matter are reviewed, placing special emphasis on the peculiarities of semiconductors. The signals generated in a semiconductor detector as a result of a γ-ray interaction are studied in order to establish how the event information can be extracted. The new concept of a main interaction among all comprising an event is introduced as an extension from single interaction events into multiple interaction ones. An infinitely long coaxial detector is then used to investigate how the signal shape varies according to the interaction position. A previously used method [Sch92, Gou94] for radius determination is reviewed and the parameter measured recognised to be the drift time of majority charge carriers. A new method for measuring this parameter is introduced as an extension of the γ-entry radius measurement to multiple interaction events and thus to higher γ-energies.

2.1 The detection process

The purpose of a γ-ray detector is to produce an electrical signal that contains in some way the desired information from the photon. In addition to the basic parameter, the energy it has deposited in the detector, other information that may for instance be of interest is its polarization state or the entry position in the detector. The detection of photons is an indirect process, involving an interaction between the photon and the detector material that results in all or part of the energy being transferred to one or more charged particles. It is only through the energy loss from this electron or positron that the γ-energy is converted into an electrical signal. Therefore, for a γ-ray to be detected, it must first interact with the material, but it is possible that it travels through the detector without undergoing an interaction.

In general, the detection of a γ-ray, a detector event, involves one or more interactions. The difference between single and multiple interaction events lies in the distribution of the energy in the detector volume. A further distinction can be made between full and partial energy events, according to the fraction of the initial γ-energy that is deposited in the detector. Since full energy events are the only informative events for γ-spectroscopy, the aim is to keep their ratio to partial energy events as high as possible.

For the energy range of interest in Nuclear Spectroscopy, from 1 keV to a few tens of MeV, the interaction mechanisms that a photon, in the form of an X- or γ-ray, can undergo in a solid state detector are restricted to photoelectric absorption, Compton scattering and electron-positron pair production. The relevance of each interaction mechanism as a function of energy will be investigated in section 2.1.1. It is also important for the calculation of the signals produced as a result of each detection to know how localised the γ-energy deposition is and this will be studied in section 3.3.

All interactions produce an electron much more energetic than those in the conduction band and the transfer of energy to the detector then takes place by impact ionization and Bremsstrahlung. These electrons will be referred to in the next section as fast or high energy electrons, since their energy is much higher than that of all other electrons in the semiconductor material. Section 2.1.2 will study the transfer of the interaction energy to the detector.

2.1.1 Interactions of γ-rays with detector materials

In this section, the differences between the three interaction mechanisms will be reviewed and their relevance to the number of photons detected considered. The question of whether the detector has a transfer function relating the resulting electrical signals and the γ-ray detected will be investigated.

Photoelectric absorption

In the case of photoelectric absorption, the incident photon transfers its energy E_γ to a bound electron in the detector material. The kinetic energy of the electron is

$$E_e = E_\gamma - E_b, \tag{2.1}$$

where E_b is the electron binding energy. The vacancy created is immediately filled by a valence electron and the binding energy is liberated in the form of a characteristic X-ray or an Auger electron. Due to their low energy, the range of these Auger electrons is very short (see section 2.1.2). Since the energies are comparable, the characteristic X-ray also has a very short range (see eq. 2.10). Below the characteristic X-ray energy, photons cannot interact with the shell electrons, producing the sharp edges in the probability of an interaction taking place seen in Fig. 2.1.

The probability of photoelectric absorption taking place per detector atom, the cross-section of the interaction, over the range of energies of interest and usual atomic numbers Z of detector materials can be approximated [Deb88] by:

$$\sigma_{pe} = k_{pe} \cdot \frac{Z^{4.5}}{E_\gamma^3} \ , \tag{2.2}$$

where k_{pe} is a proportionality constant. For compounds, the different atomic numbers have to be averaged according to their fractions by weight. Materials with higher atomic numbers have much larger cross-sections and therefore stop a much higher proportion of photons. It should also be noted that at constant atomic density, the probability of an interaction occurring is proportional to the path length of detector material "seen" by the photon.

Photoelectric absorption is the dominant interaction between γ-rays and semiconductors below 100 keV. For higher energies, the final interaction in a full energy event has to be of this type, since it is the only mechanism that does not produce secondary photons. For this interaction type, the full E_γ is transferred to the semiconductor material at the position where the interaction takes place.

Compton scattering

In Compton scattering, the photon transfers part of its energy to a loosely bound electron. A secondary photon γ' carries the remaining energy,

$$E_{\gamma'} = E_\gamma - E_{\text{recoil}} \ . \tag{2.3}$$

The recoiling electron transfers its energy to the crystal in a couple of millimeters while the scattered photon is equivalent to an initial γ-ray of this lower energy produced at this position, and may undergo one of the three interaction types. Depending on the relative angle θ between the trajectories of the two photons, the energy of the secondary electron takes the value

$$E_{\gamma'} = \frac{E_\gamma}{1 + \frac{E_\gamma}{m_e c^2}(1 - \cos\theta)}. \tag{2.4}$$

The path length presented to γ' is a function of θ and the position in the detector where it is generated. Small scattering angles result in secondary photons that have nearly the full E_γ and therefore have a lower probability of producing full energy events than when Compton scattering occurs with large θ. According to eq. 2.2, materials with higher atomic numbers allow fewer secondary photons to escape and, despite Compton scattering being part of the event history, produce a higher fraction of full energy events.

At $\theta = \pi$, the energy of the back-scattered secondary photon has a minimum, producing the so-called Compton edge in the energy spectrum, when this scattered photon escapes the detector. The energy of the secondary photon can take any value between this minimum and the energy of the original photon, so that a continuum is seen below the Compton edge. The shape of this continuum is determined by the probability of the corresponding secondary photon not being detected. When it is detected, the event becomes a full energy event.

The Compton cross-section can be approximated by

$$\sigma_{cs} = k_{cs} \cdot \frac{Z}{E} , \tag{2.5}$$

where k_{cs} is a proportionality constant. According to the Klein-Nishina formula (e.g. [Leo87]) large scattering angles become increasingly improbable as E_γ grows. As a result, the proportion of full energy events decreases as the energy increases. For this interaction mechanism, only part of E_γ is transferred to the detector at the position of the interaction.

Pair production

The term “pair production” refers to the creation of an electron-positron pair by a photon. This process can only take place in the close proximity of a nucleus and requires a minimum $E_\gamma \geq 1.022$ MeV, twice the rest mass of the electron. Any excess energy above this threshold is shared between the electron and positron as kinetic energy. The positron subsequently annihilates with a thermal electron into at least two 511 keV photons within a short distance of the position where pair production has occurred. Two photon annihilation is a much more probable process than that involving three photons, which can hardly be observed. The probability of these photons being detected in the crystal is directly related to the active volume they “see”. Note that the total energy detected when both secondary photons are stopped in the crystal is E_γ; one electron is produced and another taken from the material for the annihilation. With increasing detector volume, the proportion of events where one or both annihilation photons escape decreases. Furthermore, the intensity of the double escape peak, corresponding to both 511 keV photons escaping the detector, relative to the single escape line also decreases.

The cross-section for pair production σ_{pp} [Deb88] follows

$$\sigma_{pp} = k_{pp} Z^2 \ln(E) - k_{pp} Z^2 \ln(1.022 \text{ MeV}) = k_{pp} Z^2 \ln(E) - \sigma_{pp_{\mathrm{th}}}, \qquad (2.6)$$

where k_{pp} is a proportionality constant and the second term explicitly indicates the 1.022 MeV threshold. Although the probability of pair production occurring is very low below γ-energies of several MeV, the escape peaks are visible at $E_\gamma \geq 1.8$ MeV for small detectors [Pel82].

The probability of detecting a γ-ray

From the cross-section of an interaction, the corresponding linear attenuation coefficient is defined as

$$\mu_i = \sigma_i \cdot N_{\text{atom}} = \sigma_i \cdot \rho \frac{N_A}{M} \ , \tag{2.7}$$

where M, ρ, N_{atom} are the molar mass, mass- and atomic densities of the material and N_{A} is the Avogadro number. The linear attenuation coefficient gives the probability that a photon from a beam impinging on the detector interacts with the detector per unit path length. For γ-rays, using eqs. 2.2, 2.5 and 2.6,

$$\mu(E) = N_{\text{atom}} \left[k_{pe} \frac{Z^{4.5}}{E^3} + k_{cs} \cdot \frac{Z}{E} + k_{pp}(E) \cdot Z^2 \ln(E) - \sigma_{pp_{\text{th}}} \right] . \tag{2.8}$$

Fig. 2.1 (e.g. [Gun97]) shows the different attenuation coefficients for the three types of interaction in germanium and the sum over the range of energies of interest. It can be seen that Compton scattering dominates the deposition of energy between 150 keV and 8 MeV. In this range of energies, further interactions will be required to fully stop a γ-ray in a detector. Note that full energy events must include one photoelectric absorption, or more if pair production is part of the event history. When N_0 photons impinge on the detector material, the number N of photons that after a length x have not undergone an interaction is

$$N = N_0(1 - \mathrm{e}^{-\mu x}), \tag{2.9}$$

which is related to the detector efficiency as defined below.

The average distance travelled by a gamma in the detector before an interaction takes place, the mean free path λ, is

$$\lambda = \frac{1}{\mu}. \tag{2.10}$$

From Fig. 2.1, λ varies between a few tens of μm to a few cm in germanium, depending on E_γ, and is the thickness after which, on average, the intensity of an

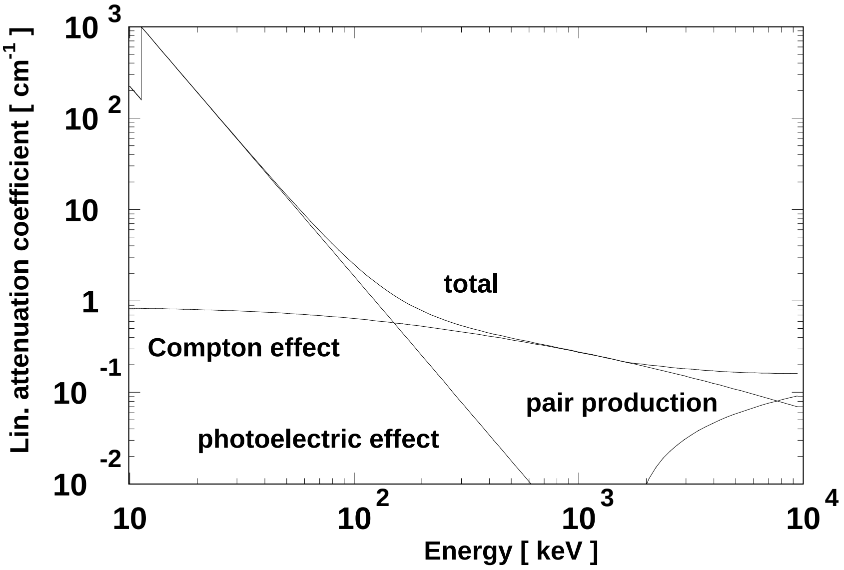

Figure 2.1: Linear attenuation coefficient in germanium and its components

incident photon beam is reduced by a factor e^{-1}. The dependence on the material density ρ can be removed by using the mass attenuation coefficient μ/ρ.

The intrinsic efficiency of a detector, defined as the ratio

$$\epsilon_{\mathrm{int}} = \frac{\text{Detected photons}}{\text{Incident photons}} \ , \tag{2.11}$$

reflects the probability of an incident photon depositing all or part of its energy in the material. It is related to the linear attenuation coefficient and the path length presented by the detector to incident photons, which is heavily dependent on the geometry of the source–detector arrangement. In general, it increases with the volume of the detector. The photopeak efficiency, defined as

$$\epsilon_{\mathrm{ph}} = \frac{\text{Full energy events}}{\text{Incident photons}} \ , \tag{2.12}$$

gives an indication of the suitability of the detector for a given energy. The proportion of full energy events at a given E_γ depends on the efficiency at and below E_γ, since the efficiency for secondary photons determines whether a scattered photon escapes the detector or not. The photopeak efficiency ϵ_{ph} decreases with increasing photon energy and is a major factor in selecting a detector for a given measurement. For detecting individual photons, ϵ_{ph} is a crucial parameter in the selection of the detector material.

The ratio of full to partial energy events can be improved if a detector is surrounded by another shield detector. The material for this shield is selected to stop as many of the secondary photons as possible. For germanium detectors, a scintillator from Bismuth Germanate (BGO) is usually chosen due to its high average atomic number. An ideal shield would not be seen by the radiation source but would stop all secondary photons generated in the detector. Then, if both detectors see a γ-ray simultaneously, it is necessarily due to a partial energy event in the shielded detector and the event is discarded for the spectrum. In practice, the geometry of the shield is optimised to enclose the detector to the largest possible extent while presenting a small volume to γ-rays from the source.

Does the detector have a transfer function?

For full energy events, there is a clear correspondence between the energy of the incident photon and the charge liberated in the detector. But it is not certain that all incident photons result in full energy events. Even at low energies, where detectors larger than a certain volume produce almost only full energy events, the position where the energy is deposited can vary from event to event. Moreover, the fraction of E_γ deposited in the detector differs among partial energy events. Again, the positions where the interactions take place can be anywhere in the detector. It is therefore not possible to establish a correlation between the incident E_γ and the signal generated by the detector that is valid for all events. For these reasons, no transfer function in the network theory sense can be established for the detector.

A further consequence of this lack of deterministic behaviour is the necessity of treating each event independently. For events of a given detected energy, the only parameter that can be assumed to remain constant is the energy deposited in the detector. But no distinction can be made between full and partial energy events that deposit the same energy when the detector is unshielded, except, in the case of known line spectra, when measured energies can be matched to the known γ-lines irradiated. Moreover, due to the statistical nature of radiation emission, there is in general no relationship between one event and the previous or the following one.

2.1.2 The transfer of the interaction energy to the detector

For all interaction types, a high energy electron, and in the case of pair production also a positron, is set free and it is only through its interaction with the material that the photon is detected. In a semiconductor, the active volume for detecting charged particles is the depletion region of a reverse biased diode. In this region, the kinetic energy of the electron is consumed in creating electron-hole pairs that are then separated by the strong field present.

The energy of the fast electron is transferred to the detector mainly by directly liberating electron-hole pairs, but at higher kinetic energies Bremsstrahlung increasingly contributes to the total energy transfer. For an electron with 1 MeV kinetic energy, Bremsstrahlung represents about 5 % of the total energy loss in germanium. The energy transferred by the fast electron to the semiconductor per unit displacement is the sum of the specific energy loss of a charged particle in a material, given by the the Bethe-Bloch formula

$$-\left(\frac{\mathrm{d}E}{\mathrm{d}x}\right)_{\text{electron}} = \frac{2\pi e^4 N_{\text{atom}} Z}{m_e v^2}\left[\ln\frac{m_e v^2 E}{2I^2\left(1-\beta^2\right)} - \ln 2\cdot\left(2\sqrt{1-\beta^2}-1+\beta^2\right) +\right.$$

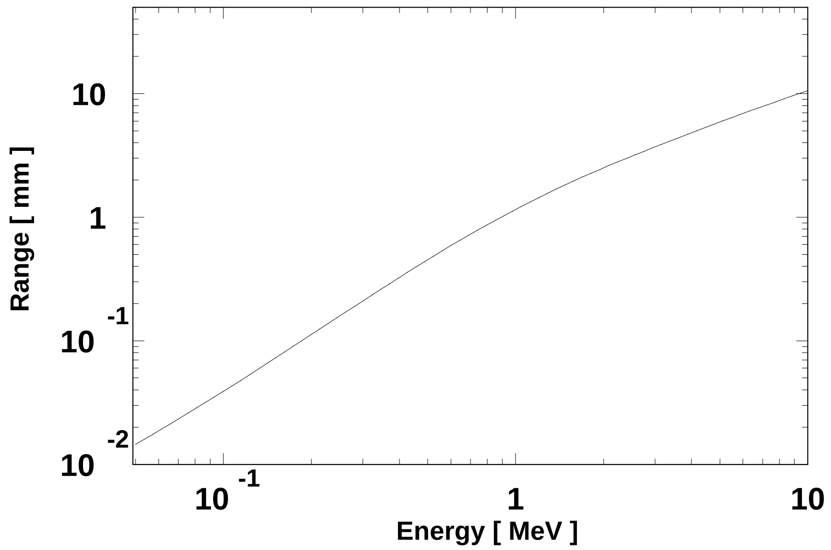

Figure 2.2: Range of electrons in germanium as a function of kinetic energy

$$+\left(1-\beta^2\right)+\frac{1}{8}\left(1-\sqrt{1-\beta^2}\right)^2\Bigg], \tag{2.13}$$

and the contribution from Bremsstrahlung,

$$-\left(\frac{\mathrm{d}E}{\mathrm{d}x}\right)_{\text{electron}}=\frac{\alpha N_{\text{atom}}EZ\left(Z+1\right)e^4}{m_e^2c^4}\left(4\,\ln\frac{2E}{m_ec^2}-\frac{4}{3}\right), \tag{2.14}$$

where α is the fine-structure constant, e, m_e are the electron charge and rest mass, c is the velocity of light in vacuum, E, v are the energy and velocity of the fast electron, β is v/c, Z, N_{atom} are the atomic number and atomic density in atoms/cm^3 of the detector material and I is the average ionization potential of the material.

Combining both equations, the average distance covered by an electron before completely depositing its kinetic energy in the detector can be calculated. Fig. 2.2 [Muk76] illustrates that in germanium the energy is transferred to the detector within a few millimeters of the electron being produced for all energies of interest.

The positron is not a stable particle and, once its energy becomes comparable to the thermal energy of electrons in the semiconductor crystal, it annihilates and at least two photons must be produced in order to conserve momentum. For the full energy of the positron to be deposited in the detector, all secondary photons must be stopped. As the positron and the fast electron lose nearly the same energy and have the same properties, their ranges are comparable.

Fig. 2.2 shows clearly that the creation of electron-hole pairs is a localised process in germanium. The energy deposited by an interaction is transferred to the detector in a small volume surrounding the position of the interaction. The number of electron-hole pairs created is given by the ratio of the deposited energy E_i to the average energy required to free an electron-hole pair,

$$N_{\text{pairs}} = \frac{E_i}{<E_{\text{pair}}>}. \tag{2.15}$$

As a result, the energy of the interaction can be measured by determining the charge it liberates. Charge carriers in detectors are not always generated independently of each other [Kno89], and a correction, the Fano factor F, for the statistical variance is introduced. The variance is thus

$$\Delta N_{\text{pairs}} = \sqrt{F N_{\text{pairs}}} \; . \tag{2.16}$$

The Fano factor becomes unity when charge carrier generation is a Poisson process but for semiconductors, $F \ll 1$ and at 77 K $F \simeq 0.06$ for germanium and $F \simeq 0.08$ for silicon. From eq. 2.15, the contribution to the energy resolution from the statistical variance in the number of charge carriers produced is

$$\Delta N_{\text{pairs}} = \sqrt{F \frac{E_i}{<E_{\text{pair}}>}}. \tag{2.17}$$

Due to the much smaller values for $<E_{\text{pair}}>$ in semiconductors than for other γ-ray detector materials, they produce a larger number of charge carriers with a smaller statistical fluctuation, leading to one of the best energy resolutions of all γ-ray detectors.

2.2 Germanium as a γ-ray detector material

The intrinsic semiconductors most widely available are silicon and germanium. The reasons why γ-ray detectors are made from germanium will be presented in this section. A detailed description of the different detector geometries commonly used in γ-spectroscopy will follow.

2.2.1 The choice between germanium and silicon

An important reason for selecting a detector material is illustrated in eq. 2.8. Due to the large difference in Z between germanium and silicon (see table 2.1), it is clear that germanium offers higher efficiency for γ-ray spectroscopy. The photoelectric attenuation coefficient for silicon is an order of magnitude smaller than in germanium (see e.g. [Deb88]). Therefore, over the low energy range, the efficiency of germanium is much larger for detectors of the same volume. As already remarked, the quality of the spectra for a given E_γ depends on the proportion of full energy events and hence, on the efficiency at energies at and below E_γ. For energies where Compton scattering dominates, a lower proportion of the secondary photons escape a germanium detector, increasing the quality of the energy spectra produced. Furthermore, the difference in energy gap is responsible for the better energy resolution in germanium, since more charge is liberated per deposited energy (see eq. 2.15).

The inconvenience caused by the necessity to cool germanium for it to become a semiconductor is often more than compensated by the superior efficiency and energy resolution offered in comparison to silicon. In practice, cooling is arranged so that the detector is placed between the radiation source and the thermal conductor or cold finger with the cryostat wall in the radiation incident direction is made as thin as possible. The energy resolution of germanium crystals has been

Property [Units]	Si	Ge
Atomic number	14	32
Atomic density [atoms/cm^3]	5.0×10^{22}	4.42×10^{22}
Intrinsic carrier concentration (300 K) [cm^{-3}]	1.45×10^{10}	2.4×10^{13}
Forbidden Energy gap (300 K) [eV]	1.12	0.66
Forbidden Energy gap (0 K) [eV]	1.17	0.74
Energy per electron-hole pair (300 K) [eV]	3.62	
Energy per electron-hole pair (77 K) [eV]	3.72	2.95
Melting point [°C]	1415	937

Table 2.1: Properties of intrinsic semiconductors (From [Sze81] and [Kno89]).

found [Tho93] to be constant for operating temperatures between 83 and 125 K, but neutron damage reduces the energy resolution by trapping charge carriers, with a strong temperature dependence due to the release time constant of the trapping centres. Therefore, an optimum range of operating temperatures has been found between 77 and 100 K.

CZT ($Cd_{0.9}Zn_{0.1}Te_{1.0}$) matches the efficiency of germanium and offers slightly worse energy resolution ($\simeq 0.5$ % at 60 keV), although without requiring low temperature operation. The present limit in the detector-quality crystal size that can be produced currently prevents using this material for energies above a few 100 keV.

In order to resolve the position where interactions occur, it is also important that, as seen in eqs. 2.13 and 2.14, in germanium the energy is deposited in a far smaller volume around at the point of interaction than in silicon as a result of the higher Z.

2.2.2 Germanium detector geometries

Apart from the atomic number Z, the other parameter that affects the efficiency and the quality of a detector is its active volume. The quality of the measured energy spectra is determined by the efficiency for secondary photons and efficiency increases with detector volume. Hence, the active volume should be as large as possible. In semiconductor detectors, the active volume for detecting radiation is the depletion region of a reverse biased diode. In this region, the high electric field separates the freed electron-hole pairs before recombination can occur. The charge carriers then drift under the influence of the field to the corresponding contacts, as indicated in Fig. 2.3.

The rectifying contact is always the outer electrode of the crystal, producing higher field strengths in the large volume corresponding to larger radii than when it is placed at the core hole. Therefore, n-type detectors have the n^+ contact on the central electrode and the p^+ on the outer surface, whereas p-type crystals have the location of the contacts exchanged. The amount of material removed from the active volume is thus smaller in an n-type detector, making a slight difference in the efficiency for the same dimensions. At the same time, the thicker outer contact increases the threshold for the lowest γ-energy that can be detected from 5 keV in n-type closed ended coaxial detectors to 40 keV in p-type crystals. Note that majority charge carriers drift towards the central electrode and minority carriers to the outer contact for both semiconductor types.

The only mechanism relevant for charge to be lost is trapping. Some of the other elements and any lattice defects present in the crystal create deep impurities or traps [Hal74, Wic74]. The difference with shallow impurities from donor or acceptor atoms is that the energy levels they introduce do not lie at the edges of the forbidden band, hence are “deep”. These deep impurities capture a conduction electron or hole for a certain period of time, eventually releasing it according to a relaxation time constant. For germanium at 77 K, this time constant is much longer than the duration of the signal from a detection event ($\lesssim$ 500 ns) effectively removing the trapped charge from the event. The probability of trapping taking place shows a sharp temperature dependence and detectors subjected to high neutron or proton fluxes should be kept below 100 K [Tho93, Koe95], in

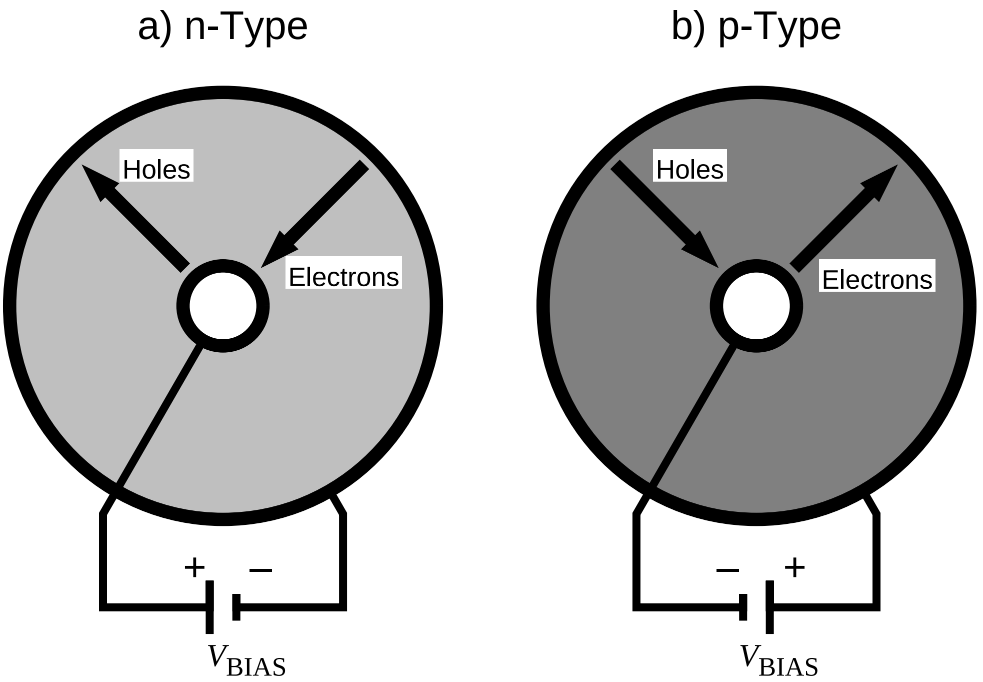

Figure 2.3: Cross-section of n- and p-type semiconductor detectors with the corresponding charge carrier drift directions

order to minimise the loss of energy resolution.

The charge lost by trapping is reflected in a detected energy lower than E_γ. The shape of the peaks in the energy spectra presents a non-symmetric contribution: a low energy tail. In γ-ray detectors, lattice dislocations can be due to fast neutrons or protons. These trapping centres can be removed by annealing: the crystal is slowly heated until the cryostat reaches about 100 °C, and is let to slowly cool off after a period of between 48 and 72 hours.

The active volume

The simplest detector geometry is planar: a cuboid of semiconductor material with parallel contacts on two opposing sides. For an intrinsic semiconductor material with impurity concentration N and dielectric constant ϵ, applying a reverse biasing voltage V_{BIAS} produces a depletion region of depth

$$d = \sqrt{\frac{2\epsilon V_{\mathrm{BIAS}}}{eN}}. \tag{2.18}$$

When the whole block of material can be depleted, the minimum voltage that accomplishes full depletion is called the depletion voltage. If the distance between contacts is large, reverse breakdown in the proximity of the rectifying contact will occur [Sze81] before the depletion region has reached the other electrode. The depletion region can be enlarged by decreasing the impurity concentration in the semiconductor.

The impurity concentration in semiconductor materials can be reduced by zone refining, as explained in [Ort95]. This process exploits the large difference in impurity concentration between the liquid and the solid phase of a semiconductor. One end of a semiconductor ingot is melted and the material is then moved so that the melted slice eventually reaches the opposite end. This process is repeated until the desired impurity concentration in the bulk of the ingot is achieved. The end where the process always finishes is then discarded due to its high impurity concentration. The impurities are dissolved in the melted slice and collected at the end of the ingot that is discarded. Due to the lower melting point of germanium, zone refining is much more successful than for silicon. So-called High Purity germanium (HPGe) has impurity concentrations $\lesssim 1 \times 10^{10}$atoms/cm^3, corresponding to one part in 10^{12}, making HPGe one of the highest purity materials available today commercially. The single crystal used for the detector is then pulled from this high quality material [Cor74].

Another approach for increasing the depletion depth is to compensate the level of impurities by drifting an appropriate element into the semiconductor crystal. Before the advent of today's advanced refining techniques, the largest volume germanium detectors were manufactured in this way, by drifting lithium atoms. HPGe fabrication was found to be a much more reproducible process than the steps leading to the production of a lithium drifted germanium detector and displaced them once large HPGe crystals were produced.

Nowadays, HPGe detectors used in nuclear structure studies are usually n-type, due to their lower sensitivity to neutron induced damage. Annealing restores the original energy resolution and no limit has yet been observed to the number of times that an n-type detector can be subjected to this process. Annealing however causes the lithium atoms, which form the rectifying contact in an n-type and the central contact in a p-type crystal, to drift into the crystal by a variable rate (101 μm after the first cycle, 409 μm after 5, 698 μm after 10 and 3369 μm after 100 annealing processes) [Gut97]. This results in a progressive loss of efficiency in p-type, but no effect in n-type detectors.

For a given impurity concentration, there is a limit to the depletion depth that can be achieved by applying reasonable biasing voltages ($\leq$ 5000 V). Large active volumes can still be achieved for detectors with coaxial geometry (see in Fig. 2.4) simply by making longer crystals of the maximum depletion thickness. The volume is limited by the maximum length of the single crystals of detector quality that can be manufactured.

The **true coaxial** configuration (see Fig. 2.4a), where the central core is removed all along the length of the crystal, was the first to be developed. Surfaces between contacts, however, need to be passivated and the quality of the resulting layer is directly reflected in the detector leakage current, sometimes even short-circuiting the diode, as reported in [Arm74]. Despite the finite length, the field is almost the same as for an infinitely long detector due to the large difference in dielectric constant between germanium ($\epsilon = 16 \cdot \epsilon_0$) and the surrounding vacuum.

Closed ended detectors (see Fig. 2.4b) have only one passivated surface and are therefore less prone to developing problems at the passivation surfaces. The electric field lines are no longer purely radial and a region with reduced field

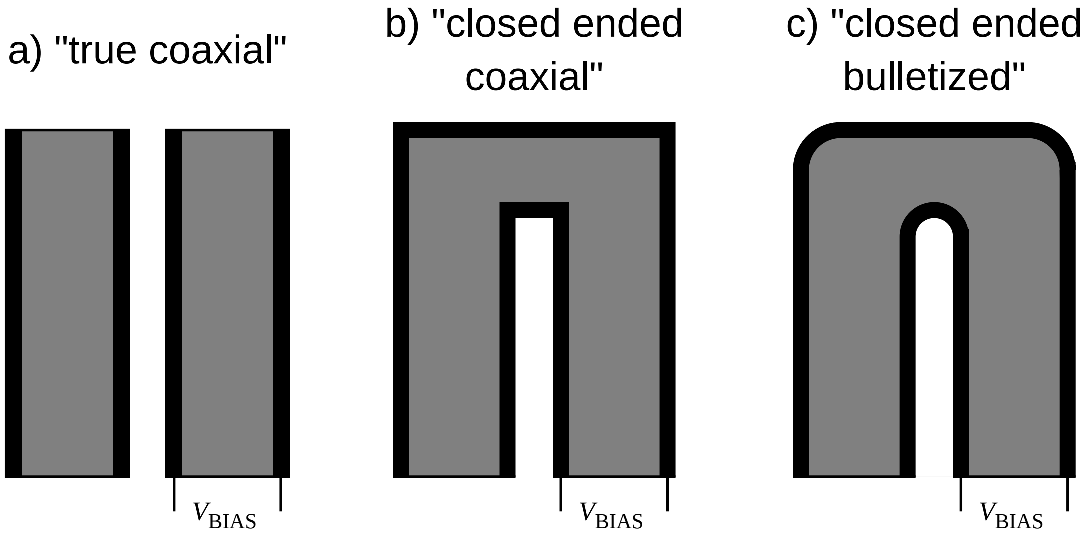

Figure 2.4: Cross-section of different geometries of coaxial germanium detectors with rotation symmetry. The electrical contacts are indicated by thick lines.

strength is produced near the front corners of the crystal, leading to lower drift velocities and thus to longer collection times for interactions occurring there. This region has a relatively large volume and a considerable fraction of photons are detected in it.

Most large volume γ-ray detectors nowadays are of the **closed ended bulletized** geometry (Fig. 2.4c). The frontal corner of the detector and the core hole are bevelled out before implanting the contacts, re-establishing a strong electric field over the whole detector volume. As the electric field varies with the inverse of the distance to the contact for cylindrical and with the inverse square law for spherical geometries, the amount of material that needs to be removed is small, leaving the efficiency of the detector unaffected.

Both closed ended geometries can be divided into two parts, a true coaxial detector and a round planar detector at the front. In the following chapters, these parts will be referred to as the geometric coaxial part and the geometric planar part. It should be noted, however, that the region of the detector where the electric field is the same as for a true coaxial detector with the same radius is somewhat shorter than the geometric coaxial part.

The impurity concentration is so low in HPGe that the contacts needed to implement a *p-i-n* diode from this material are very thin, resulting in a depletion region that covers nearly the whole crystal. Typically [Ort95], the n^+ contact is made by drifting lithium ions and results in some 600 μm thickness, whereas the p^+ contact is created by boron ion implantation and is about 0.3 μm thick. Depending on whether donor or acceptor impurities dominate in the bulk material after the refining process, the detector is said to be of *n*- or *p*-type.

2.3 Current Pulse Generation

The result of a γ-ray interacting with an HPGe detector is a localised cloud of electron-hole pairs produced around the position of the γ-interaction. The electric field in the active region is very strong, typically above 1000 V/cm, separating the charge cloud into two before recombination can take place. Under the influence of the field, these clouds drift to opposing contacts and induce a mirror charge on the electrodes. In order to establish this mirror charge, a current flows at each electrode.

The electrostatic field in the detector can be calculated by solving Poisson's equation for the electrostatic potential ϕ,

$$\nabla^2\phi(\vec{r}) = -\frac{\rho(\vec{r})}{\epsilon}, \tag{2.19}$$

where ϵ and ρ are the dielectric constant and charge density of the material. The electric field can then be calculated by solving

$$\vec{E}(\vec{r}) = -\vec{\nabla}\phi(\vec{r}). \tag{2.20}$$

In the depletion region of an HPGe diode, the charge density is a result of the impurities present in the material. The shallow levels introduced by these impurities are emptied as the reverse biasing voltage is applied, leading to $\rho = e(N_A - N_D)$, where N_A and N_D are the acceptor and donor concentrations and ρ is positive for n-type and negative for p-type crystals. In an n-type HPGe detector, the impurity concentration is typically 7×10^9 atoms/cm^3, resulting in a charge density of $+1.1$ nC/cm^3. Eq. 2.19 can thus be rewritten as:

$$\nabla^2\phi(\vec{r}) = -\frac{e(N_A - N_D)}{\epsilon_0\epsilon_r}, \tag{2.21}$$

where ϵ_r is the relative dielectric constant of the material, 16 for germanium. The boundary conditions for solving ϕ are the voltages at the electrodes: 0 V and V_{BIAS}. It should be pointed out that the charge liberated, 0.11 pC/MeV, is too low to have an effect on the strong field.

It has long been established [Rau82] that the drift velocities of charge carriers $({}_{\nu=e,h})$ depend on the electric field according to

$$\vec{v}_{d_\nu}(\vec{E},\vec{r}) = \frac{\mu_{0_\nu}\vec{E}(\vec{r})}{\left[1 + \left(\frac{|\vec{E}(\vec{r})|}{E_{0_\nu}}\right)^{\beta_\nu}\right]^{\frac{1}{\beta_\nu}}}\ , \tag{2.22}$$

where μ_0 is the mobility at low field strength and the parameters E_0 and β are empirically determined and listed in table 2.2. Note that μ_0 is negative for electrons due to their drifting opposite to the field direction. At high field strengths, a saturation velocity is reached, so that further increases in field strength have no effect on v_d. Along the <111> direction of germanium crystals, these saturation

Carrier	E_0 [V/cm]	β	μ_0 [cm^2/Vs]
Electrons	275	1.32	-3.6×10^4
Holes	210.5	1.36	4.2×10^4

Table 2.2: Parameters for the drift velocity in Germanium at 77 K.

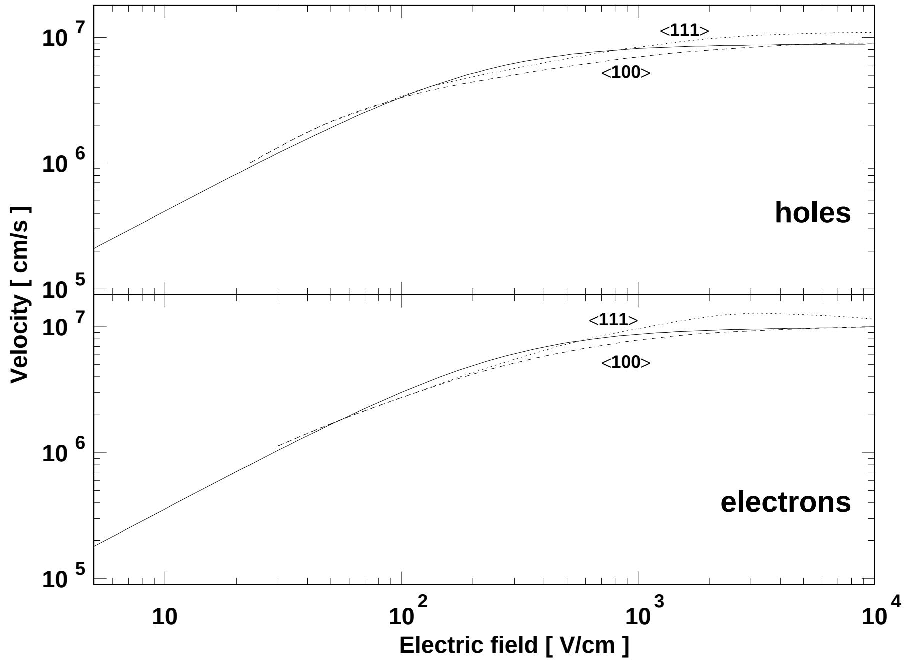

Figure 2.5: Charge carrier drift velocities in germanium as a function of electric field strength. The values measured in the <100> (dashed line) and the <111> (point line) crystal directions and the empirical equation, eq. 2.22 (solid line) are shown.

velocities are 1.0×10^7cm/s for electrons and 0.9×10^7cm/s for holes. Contrary to the situation at low field strengths, both charge carriers drift with nearly the same velocity. The variation of the drift velocities with the electric field strength is shown in Fig. 2.5, where it can be seen that the saturation velocities are reached above 500 V/cm.

In general, μ_0 is a tensor reflecting the anisotropic properties due to the crystalline structure of germanium. The variations in $|\vec{v}_d|$ with the orientation of the crystal for which it is measured are about 30 %, a factor that must be taken into account when comparing calculations of the detector signals with measurements, as the orientation of the detector crystal is usually not known.

Since the electrodes are held at constant potential, the moving charges induce a mirror charge on the contacts. When the charge cloud arrives at the electrode, the mirror charge is immediately balanced and the current that was flowing into the contact ceases abruptly. The magnitude of the charge, and thus the energy deposited by the interaction, can be measured by integrating the current at the contact. Between interactions, only the much smaller leakage current flows at the electrodes, so that its integral over the duration of the signal is negligible.

As recognised in [Tov61], but using the notation introduced by [Rad88], the current induced by a charge Q moving with velocity $\vec{v}_d$ is

$$i(t) = -Q\vec{E}_w(\vec{r}(t)) \cdot \vec{v}_d(\vec{r}(t)), \tag{2.23}$$

where $\vec{E}_w(\vec{r}\,)$ is the so-called weighting field in units of cm^{-1} and measures the electrostatic coupling between the moving charge and the sensing contact. It is dependent on the geometry of the detector and can be calculated from

$$\vec{E}_w(\vec{r}\,) = \frac{1}{V_{\mathrm{BIAS}}}\,\vec{E}(\vec{r}\,)\Big|_{\rho=0,\epsilon=\epsilon_0} = \frac{1}{V_{\mathrm{BIAS}}}\vec{E}_{\mathrm{geom}}(\vec{r}\,). \tag{2.24}$$

$\vec{E}(\vec{r}\,)\Big|_{\rho=0,\epsilon=\epsilon_0}$ does not depend on the material and is thus called the geometric field $\vec{E}_{\mathrm{geom}}(\vec{r}\,)$. The field present in the detector $\vec{E}(\vec{r}\,)$, calculated with the space charge due to the impurity concentration, will be referred to as the space-charge field in the remainder of this thesis.

As is always the case for semiconductors, the different charge polarities of electrons and holes are cancelled by the opposing drift directions, so that both current contributions have the same polarity at one electrode. Since it does not affect the validity of the arguments presented, the overall polarity of the current will be taken as positive at the core electrode.

2.3.1 Determination of the interaction radius r_i

It has long been known (e.g. [Str72]) that the shape of the signal generated by a germanium detector as a result of a γ-interaction depends on the position

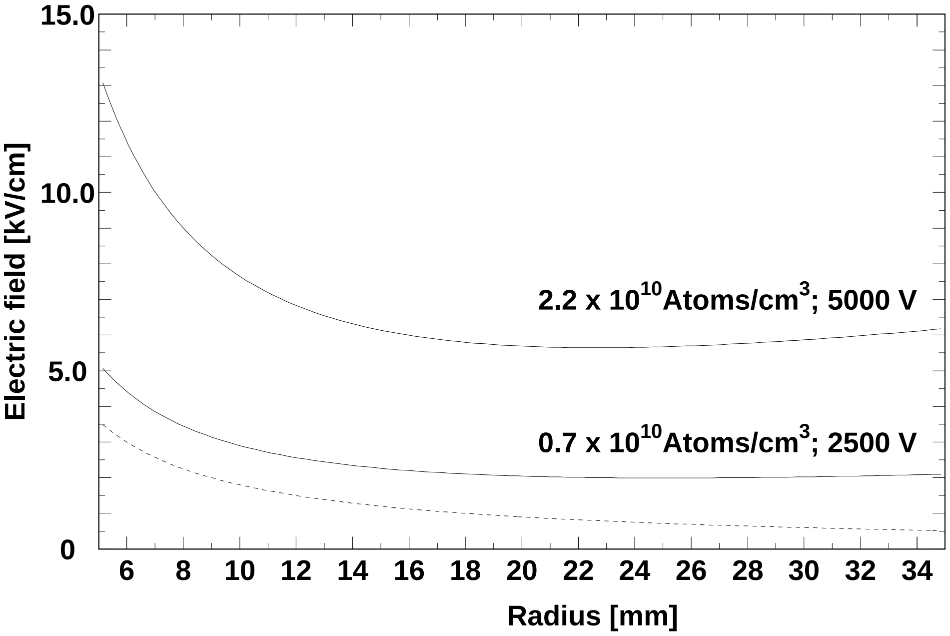

Figure 2.6: Electrostatic fields for a true coaxial detector of 35 mm outer radius and 5 mm core radius for the indicated impurity concentrations and biasing voltages. The geometric field for 2500 V is shown by a dashed line.

where the energy has been deposited. In this section, the case of an infinitely long true coaxial detector is considered to examine two techniques for extracting the distance r_i, between the position of the interaction and the the symmetry axis of the crystal, from the current pulses generated in the detection of a γ-ray. A more complete calculation for the geometry of the detector used in the measurements will be presented in chapter 3. An n-type detector has been used for the calculations, but the discussion will be kept general since the arguments do not depend on whether electrons or holes are the majority charge carriers. The small difference between the drift velocities only introduces a slight increase in the drift times of the majority carriers when they are holes.

For an infinitely long true coaxial detector, the electric fields can be solved analytically and the current pulses produced by interactions taking place at different radii calculated. The fields for a detector of outer radius b with a core hole of radius a $(V(a) - V(b) = V_{\mathrm{BIAS}} > 0)$ are

$$\vec{E}_{\mathrm{geom}}(\vec{r}) = \frac{V_{\mathrm{BIAS}}}{\ln(b/a)} \frac{\vec{r}}{r^2} , \tag{2.25}$$

$$\vec{E}(\vec{r}) = -\frac{eN}{2\epsilon}\vec{r} + \frac{V_{\mathrm{BIAS}} - \frac{eN}{4\epsilon}(b^2 - a^2)}{\ln(b/a)} \frac{\vec{r}}{r^2} . \tag{2.26}$$

Both fields are radial in direction and their variation for a 35 mm outer radius and 5 mm core radius n-type HPGe detector can be seen in Fig. 2.6. The space-charge field only affects the current through the drift velocity.

Fig. 2.6 also shows the fields resulting at both extremes of impurity concentration and biasing voltages for the CLUSTER crystals delivered up to August 1996, according to data provided by EURISYS Mesures [Gut96]. As can be observed, the electrostatic field is high enough over the whole detector for both drift velocities to be saturated (cf. Fig. 2.5). Note that a p-type crystal with the same value of impurity concentration has the same field strength, as the polarities of the charge density and biasing voltage are reversed.

The position of the charge cloud must be known as a function of time in order to calculate the current induced on the sensing electrode. Since the drift velocity depends on the electrostatic field, it is also position dependent, resulting in

$$\vec{r}(r_i, t) = \vec{r}_i + \int_0^t \vec{v}_d(\vec{E}(\vec{r}(\tau)))\, \mathrm{d}\tau, \tag{2.27}$$

where the direction of $\vec{v}_d$ determines whether the charge carriers drift towards the core or the outer electrode. For the current, the scalar product in eq. 2.23 can be substituted by the product of the magnitudes, since both fields are radial.

Single interaction events

Fig. 2.7 shows the current pulses corresponding to three interaction radii. Since the current is directly proportional to the drifting charge (eq. 2.23), it scales with

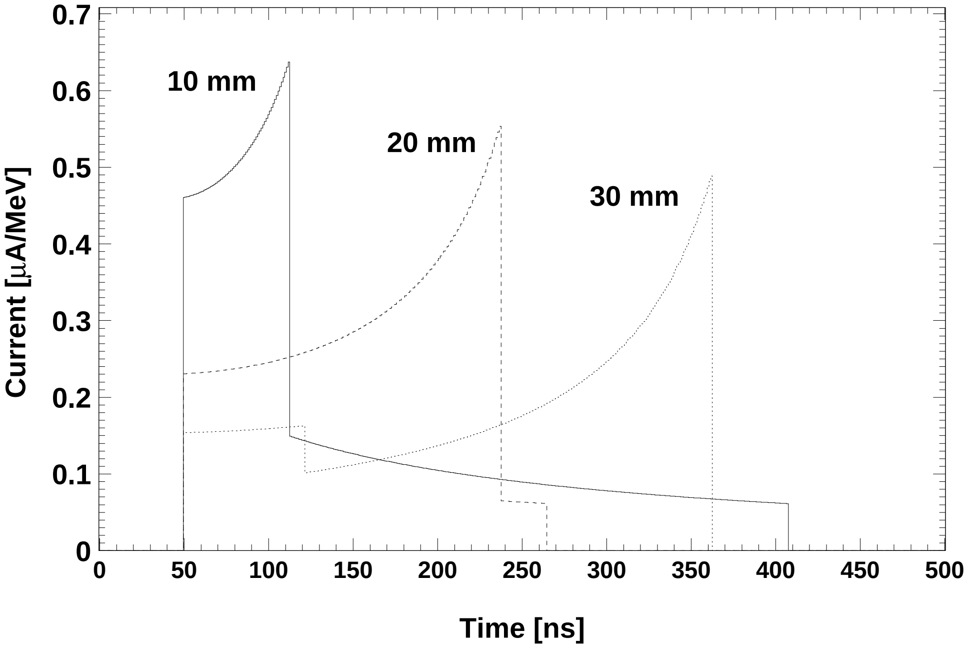

Figure 2.7: Current pulses for three interaction radii in a true coaxial detector of 35 mm outer radius and 5 mm core radius. For clarity, the pulses have been offset 50 ns.

energy for single interaction events and a γ-energy of 1 MeV has been chosen as a convenient reference energy. Note that in reality, it is highly improbable that an event of this energy consists of only one interaction. The charge clouds are assumed to be point charges.

As shown in Fig. 2.7, each current pulse has three abrupt edges. The starting edge corresponds to the liberation of charge carriers by the γ-interaction and the other two are due to the minority or majority charge carriers reaching the corresponding contact. The mirror charge influenced on the contact is then immediately compensated and the flow of current due to the corresponding carrier stops. The majority carriers, electrons in an n-type detector, drift towards the central contact and the electrostatic coupling increases, leading to a continuously rising current. Minority carriers, holes, drift away from the central electrode and their current is a continuously decreasing function of time. Moreover, for small interaction radii, the minority carriers drift a greater distance and therefore generate a longer pulse than the majority carriers. For larger radii, they reach their contact much earlier than the majority carriers and their pulse is accordingly the shorter of the two.

The final value of the majority ($_{\nu=\ maj}$) or minority ($_{\nu=\ min}$) current corresponds to the time t_{drift_ν} when the charge carriers ν reach the contact r_{cont_ν}. It is given by

$$i_\nu(t_{\mathrm{drift}_\nu}) = |Q_i| \frac{E_{\mathrm{geom}}(r_{\mathrm{cont}_\nu})}{V_{\mathrm{BIAS}}} \cdot v_{d_\nu}(E(r_{\mathrm{cont}_\nu})). \tag{2.28}$$

The maximum is proportional to the strength of the geometric field at the electrode and to the charge $Q_i = |Q_{maj}| = |Q_{min}|$ liberated by the interaction and will be taken as positive for the current pulse calculation. As seen in eq. 2.15, Q_i is directly proportional to the interaction energy. In this detector, the field strength at the outer or inner electrode of the detector is constant for the whole length, which is not in general true for closed ended coaxial crystals. It should also be noted that if the drift velocities are not saturated, then $v_{d_{min}}(b) \lessapprox v_{d_{maj}}(a)$.

There are two reasons for not combining all constants together in eq. 2.28. First, the dependence on Q_i is explicitly stated in order to extend the validity of the equation to multiple interaction events. Secondly, in contrast to this ideal detector, a closed ended detector does present a variation in the field strength along a contact.

From Fig. 2.7, the absolute maximum of the event current pulse results from the carriers drifting to the central electrode, i.e. the majority carriers as discussed in section 2.2.2. From eq. 2.28 and the values of E_{geom} at the contacts (Fig. 2.6), it is clear that the maximum of the majority charge carrier current is much larger than that from the minority carrier pulse. Thus, the majority carrier drift time $t_{\mathrm{drift}_{maj}}$ can be determined by measuring the time taken by the total current pulse to reach its absolute maximum,

$$\begin{aligned}\max i_{\text{total}}(t) = i(t_{\text{drift}_{maj}}) &= \frac{1}{V_{\text{BIAS}}} \cdot Q_i \cdot v_{d_{maj}}(a) E_{\text{geom}}(a) + i_{\min}(t_{\text{drift}_{maj}}) = \\ &= Q_i \cdot \frac{v_{d_{maj}}}{\ln(b/a)} \cdot \frac{1}{a} + i_{min}(t_{\text{drift}_{maj}}) \ , \qquad (2.29)\end{aligned}$$

and the variation in value observed in Fig. 2.7 is due to the minority carrier current still flowing at that instant. Though not explicitly stated in the literature on radial determination by measurement of the time taken by current pulses to reach their absolute maximum, it is clear that the parameter measured is the drift time of majority charge carriers.

If the drift velocity of majority carriers is constant in the whole detector, which is a good approximation under standard detector operating conditions, eq. 2.27 yields

$$t_{\text{drift}_{maj}} = \frac{r_i - a}{v_{d_{maj}}} \ . \qquad (2.30)$$

The drift time is hence a direct measure of the distance covered by majority carriers before reaching the central contact, and hence the radius at which the interaction has taken place. When the drift velocities are not saturated, the lower values occur close to the outer electrode. Given a constant minimum measurable time, this would result in a radial resolution improvement for large radii, in other words for the part of the detector with the greatest volume and therefor where detections take place.

The algorithm used for measuring the interaction radius r_i by determining the time t_{max} that the event current pulse requires to reach its absolute maximum will be denoted the **time to maximum method.** This results in a sufficiently unique determination of the interaction radius r_i whenever the total γ-energy is deposited in a single interaction.

A particular case contradicts the t_{max}/r_i correspondence in eq. 2.30: when the minority carriers reach the outer contact a short time $\mathrm{d}t$ before the majority carriers arrive at the central electrode. The total current at $t = t_{\mathrm{drift}_{\mathrm{min}}} = t_{\mathrm{drift}_{\mathrm{maj}}} - \mathrm{d}t$ is larger than the current at $t = t_{\mathrm{drift}_{\mathrm{maj}}}$. The condition can be written as

$$\begin{aligned} v_{d_{min}} \cdot Q_i \cdot E_{\mathrm{geom}}(b) + v_{d_{maj}} \cdot Q_i \cdot E_{\mathrm{geom}}(a + v_{d_{maj}}\mathrm{d}t) > \\ > v_{d_{maj}} \cdot Q_i \cdot E_{\mathrm{geom}}(a) \ , \end{aligned} \tag{2.31}$$

which is only true for a very small interval

$$\frac{b-a}{2} - \mathrm{d}r \leq r_i < \frac{b-a}{2}. \tag{2.32}$$

Subtracting the final value of i_{min} from the maximum of i_{maj} gives an upper bound for $\mathrm{d}r$

$$\mathrm{d}r \leq \frac{v_{d_{min}}(b)}{v_{d_{maj}}(a)} \frac{a^2}{b - \frac{v_{d_{min}}(b)}{v_{d_{maj}}(a)}a} < \frac{a^2}{b-a} \ , \tag{2.33}$$

which is 0.8 mm for this ideal detector. It is therefore smaller than the typical radius of the charge cloud and hence is smaller than the radial resolution that can be achieved in a real detector.

Multiple interaction events

For multiple interaction events, the total current pulse is the sum of the current pulses from each interaction $i_i(t)$,

$$i(t) = \sum_i i_i(t). \tag{2.34}$$

The current generated as a result of an interaction (2.23) can be separated into a geometric current normalised to unit energy and a weighting factor, the charge liberated by the interaction. Substituting the the geometric field (eq. 2.25) in eq. 2.23 yields

$$i_\nu(t) = Q_i \frac{1}{\ln(b/a) r(t)} v_{d_\nu}(r(t)), \tag{2.35}$$

which can be rewritten as

$$i_\nu(t) = Q_i \, i_{\mathrm{geom}_\nu}(r_i, t) \ , \tag{2.36}$$

where i_{geom_ν} is the electron or hole current pulse for a given interaction that liberates unity charge at the position r_i.

The duration of the energy transfer process is very short [Tov61] and the maximum time between interactions is much shorter ($<$ 350 ps for a detector of 35 mm outer radius and 70 mm length) than the charge collection times ($\lesssim$ 400 ns). Therefore, the individual interaction pulses can be assumed to be generated simultaneously and the first interaction in an event cannot be determined by measuring the time difference to the other interactions.

From eq. 2.35, each interaction current is proportional to the energy deposited by the corresponding interaction. The **main interaction** is defined as that depositing the largest fraction of the original γ-energy. Note that the main interaction is still defined in single interaction events. In general, though, the main interaction need not be the first interaction in a multiple interaction γ-event and therefore does not necessarily define the direction of the γ-ray.

The current pulse from the main interaction has the largest weighting factor and will therefore dominate the event current pulse. It is however by no means clear that the absolute maximum of the event current pulse is due to the absolute maximum of the main interaction pulse. The maximum from a lower energy interaction pulse can, added to intermediate values from the other interaction pulses, produce the absolute maximum of the event current pulse. An example of such an event current pulse is presented in Fig. 2.8, where the absolute maximum of the current pulses is due to the interaction depositing the lower fraction of the original γ-energy.

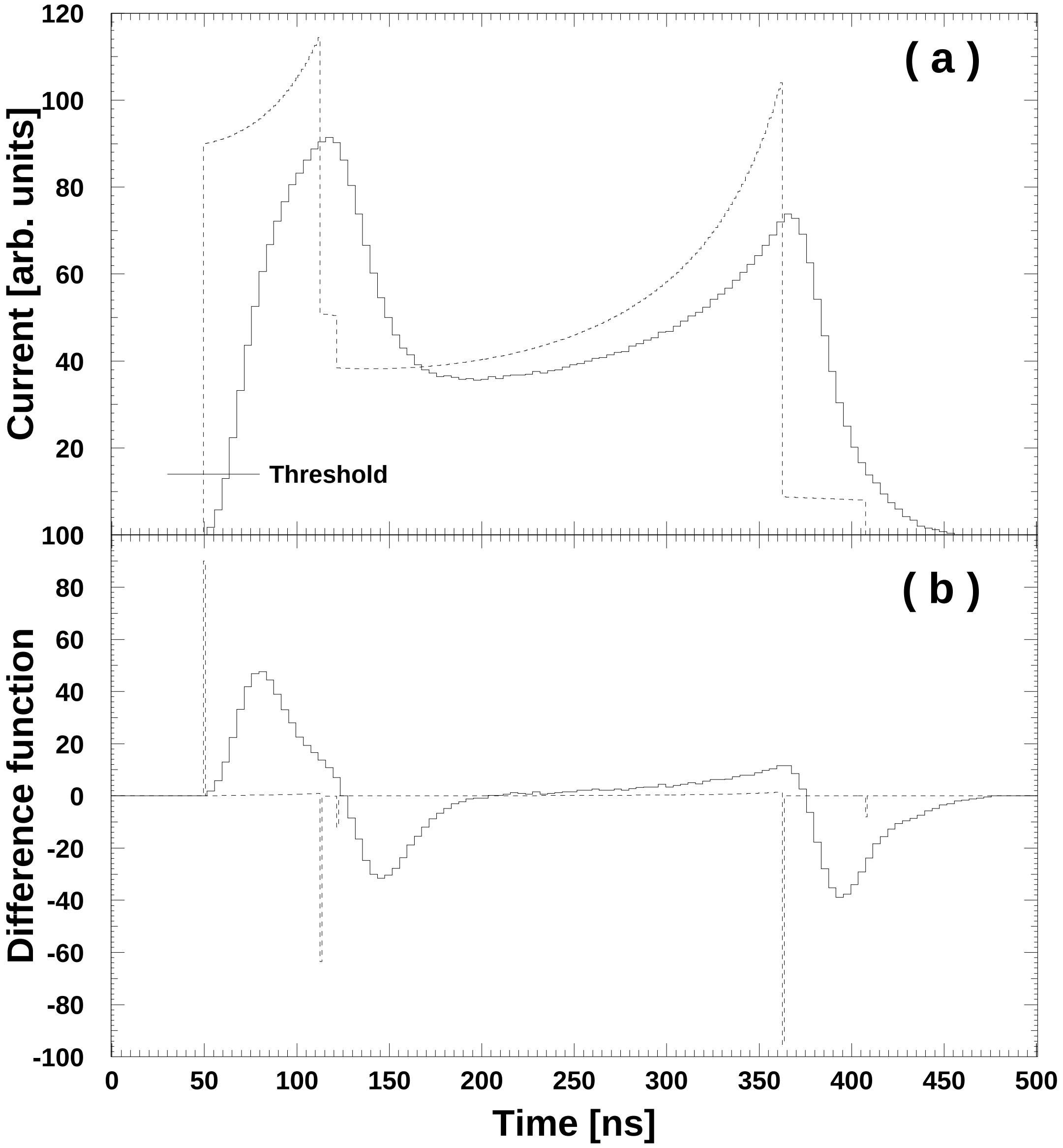

Figure 2.8: Ideal (dashed line) and real current pulse (a) and difference function (b) for an event depositing 40% of the γ-energy at $r = 10$ mm and 60% at $r_m = 30$ mm. The real pulse is obtained by convoluting the the ideal pulse with the transfer function of the electronics used to digitise the current pulse, see chapter 5. Also shown is a possible threshold for detecting the beginning of the current pulse.

The steepest slope method

In order to extract the drift time of majority charge carriers from the main interaction, a new method is proposed in this thesis. This method determines the time when the largest drop in the current signal per constant time interval Δt takes place. For simplicity, the method will be discussed with ideal current pulses and a (backward) difference function $d(t, \Delta t)$ is defined as

$$d(t, \Delta t) = \frac{i(t) - i(t - \Delta t)}{\Delta t} \;, \tag{2.37}$$

where $\Delta t > 0$, to overcome the fact that ideal current pulses are non-differentiable at t_{drift_ν}. From the three possible difference functions (forward, centred and backward), only eq. 2.37 can be evaluated electronically in real time.

As shown in Fig. 2.8, the largest drop in $i(t)$ and the absolute minimum of $d(t)$ occur simultaneously. Note that all characteristic times of the signals are measured relative to the time when the pulse starts (e.g. when the signal exceeds the threshold indicated in Fig. 2.8). It is obvious that when $i(t)$ is differentiable, $d(t, \Delta t)$ reduces to the derivative from the left of $i(t)$ as $\Delta t \to 0$. The new method for the determination of the drift time of majority charge carriers from the main interaction is therefore referred to as the **steepest slope method.** When evaluating the difference function, Δt is kept constant and therefore t becomes the only variable. The difference function is thus an approximation of the first derivative of $i(t)$ and will be denoted as $d(t)$ in the remainder of this thesis.

For simplicity, the method will be first explained for single interaction pulses. In this case, there is a majority carrier and a minority carrier current, both originating at r_i. For reasonably small Δt ($\Delta t \ll t_{\mathrm{drift}_\nu}$), the minima of $d_{maj}(t)$ and $d_{min}(t)$ are reached at the respective drift times, namely

$$\min d_{maj}(t) = d_{maj}(t_{\mathrm{drift}_{maj}}) = -Q_i \frac{v_{d_{maj}}(a)}{\ln(b/a)} \frac{1}{a} \frac{1}{\Delta t} \tag{2.38}$$

and

$$\min d_{min}(t) = d_{min}(t_{\mathrm{drift}_{min}}) = -Q_i \frac{v_{d_{min}}(b)}{\ln(b/a)} \frac{1}{b} \frac{1}{\Delta t} \ . \tag{2.39}$$

Note that the minima depend only on the liberated charge Q_i and the geometric field at the contacts. For this detector,

$$\frac{\min d_{maj}(t)}{\min d_{min}(t)} = \frac{b \cdot v_{d_{maj}}(a)}{a \cdot v_{d_{min}}(b)} \simeq 7 \ . \tag{2.40}$$

Therefore, the minimum of the total difference function occurs when the majority charge carriers reach the core electrode ($t = t_{\mathrm{drift}_{maj}}$) and takes the value

$$\min d(t) = d(t_{\mathrm{drift}_{maj}}) = -Q_i \frac{v_{d_{maj}}(a)}{\ln(b/a)} \frac{1}{a} \frac{1}{\Delta t} + d_{min}(t_{\mathrm{drift}_{maj}}) \ . \tag{2.41}$$

In general, $t_{\mathrm{drift}_{maj}} \neq t_{\mathrm{drift}_{min}}$ and the difference function for minority charge carriers at $t_{\mathrm{drift}_{maj}}$ takes the value

$$d_{min}(t_{\mathrm{drift}_{maj}}) = \frac{\mathrm{d}i_{min}(t)}{\mathrm{d}t} = Q_i \frac{i_{\mathrm{geom}_{min}}}{\mathrm{d}t}. \tag{2.42}$$

While the maximum of the event current pulse (eq. 2.29) can be strongly modified by the minority current still flowing at $t_{\mathrm{drift}_{maj}}$, the minimum of the total difference function (eq. 2.41) depends only on the derivative of the minority current at $t_{\mathrm{drift}_{maj}}$. Since the minority current is only a slowly decreasing function of time, the contribution of $d_{min}(t_{\mathrm{drift}_{maj}})$ to the minimum of $d(t)$ can be neglected. Even when $t_{\mathrm{drift}_{maj}} = t_{\mathrm{drift}_{min}}$, the contribution of $d_{min}(t_{\mathrm{drift}_{maj}})$ is much smaller than that of $d_{maj}(t_{\mathrm{drift}_{maj}})$ (eq. 2.40). Therefore, the determination of $t_{\mathrm{drift}_{maj}}$ by detecting the absolute minimum of the difference function $d(t)$ is largely unaffected by the minority carrier contribution.

For multiple interaction events, $t^{\mathrm{main}}_{\mathrm{drift}_{maj}}$ is in general different from all other drift times. Therefore, the contribution of the derivatives of the majority and minority currents from the other interactions has to be examined at $t^{\mathrm{main}}_{\mathrm{drift}_{maj}}$. Due to the small values taken by the difference functions at $t \neq t_{\mathrm{drift}_\nu}$, the remaining contributions tend to cancel and the absolute minimum of $d(t)$ will be determined by the arrival at the central electrode of the majority charges from the main interaction. Hence,

$$\min d(t) = d(t^{\text{main}}_{\text{drift}_{maj}}) = -Q_i \frac{v_{d_{maj}}(a)}{\ln(b/a)} \frac{1}{a} \frac{1}{\Delta t}. \tag{2.43}$$

Therefore, the distance r_{main} from the central electrode of the point at which the main interaction has taken place can be determined by measuring the time, relative to the beginning of the pulse, when the difference function reaches its absolute minimum.

No general estimate for the percentage of events where the absolute minimum of the event difference function is not determined by the main interaction can be given. Moreover, since the range of secondary photons depends on their energy, the only way of establishing the quality of the improvement of the steepest slope method over the determination of the absolute maximum is by performing a Monte Carlo simulation (see chapter 3).

So far, only ideal current pulses have been considered. The finite bandwidth of the electronics needed to process the detector signals will lead to a loss of information. The difference function can nevertheless then be replaced by the derivative of the current pulse and the steepest slope method can be relatively easily realised electronically using an updating peak detector after differentiating the event current pulses. Due to the loss of information, the accuracy of the drift time $t^{\text{main}}_{\text{drift}_{maj}}$ determination will be somewhat lower than predicted. It is nevertheless clear from Fig. 2.8 that the radius of the main interaction is correctly determined by the steepest slope algorithm in events where the time to maximum method would give a false value.

In a true coaxial detector, only the radius of the main interaction can be determined. In general, position resolution by measuring the majority carrier drift time can only be achieved in the direction parallel to the electric field. The steepest slope method is only dependent on the geometric field values at the contacts, making it suitable for all detector geometries. The calculated position resolution that can be achieved in a CLUSTER module by both methods will be presented in chapter 4.

Chapter 3

Position Resolution

Almost all modern large volume HPGe coaxial detectors are based on the closed ended bulletized geometry. In the previous chapter, it was shown that the shape of the electrical field is directly reflected in the current pulses generated by the detector and therefore affects the position resolution that can be achieved. Moreover, the importance of the Doppler broadening correction increases with γ-energy. The distribution of the event energy in the detector and its effects on the position resolution must be investigated for the energy range of interest. The methods described in chapter 2 can yield the position of the main interaction, but in order to measure the γ-entry point, the position of the first interaction is needed. The relationship between first and main interaction in an event must be investigated to establish the position resolution that can be expected, since the only position that can be determined for most events is that of the main interaction.

When evaluating a method for measuring the entry point of γ-rays, a collimator is used to restrict the crystal volume irradiated and to establish a correlation between the results delivered by the algorithms and the position of the collimator. Care must be exercised while establishing this correlation to avoid possible ambiguities when the whole frontal surface of the detector is irradiated, as is the case in in-beam experiments. On-line, the entry position has to be determined unambiguously from the parameters extracted. When the collimator is used, a given parameter may seem to provide radial resolution, but it would be of little use if slight variations in the parameter yield completely different radii. Moreover, the measurements performed with a collimator have to take into account that no collimator material can stop all γ's at all energies, affecting the resolution that can be measured.

All studies on position resolution found in the literature use only qualitative descriptions of the structure of events. The concept of a main interaction introduced in this thesis has proved very helpful for establishing the percentage of events whose entry point can be determined satisfactorily. A thorough study of the generation of current pulses as a result of γ-ray interactions in HPGe detectors is reported in this chapter. In order to evaluate the radial resolution that can be expected in MINIBALL, the exact geometry of a CLUSTER crystal was used for solving the electric fields required for calculating the event current pulses. The space-charge field directly determines the drift time of majority carriers, which is the parameter that can be resolved by the methods introduced in section 2.3.1. Furthermore, due to the energy dependent amplitude of the individual interaction current pulses, both methods can in general only determine the position of the main interaction from the event current signal.

The position resolution that can be obtained using a CLUSTER module can be investigated by performing a Monte Carlo simulation and studying the distribution of energy among the event interactions. The correlation between the main interaction and the entry position of the γ-ray can be quantified from the results of this simulation. Furthermore, the interaction positions and energies output by the Monte Carlo simulation can be used to calculate the event current pulses and therefore establish a target for the measurable radial resolution.

3.1 Geometrical effects

The geometry of the detector

Detectors constructed from several crystals, composite detectors, have been produced recently in order to achieve efficiencies beyond those possible with single crystals. The CLUSTER detector [Tho95, Ebe92] uses individually encapsulated n-type crystals, or “modules” to isolate the crystal vacuum from that of the cryostat, simplifying the handling of HPGe detectors significantly. Its efficiency at high energies benefits from the arrangement of seven large crystals in very close proximity, so that partial energy events in one crystal become full energy events when two neighbouring modules are considered as one detector. In order to obtain a compact packaging with little dead volume in-between, the closed ended crystals are machined as shown in Fig. 3.1. The CLUSTER frontal surface consists of a central hexagon surrounded by a further six hexagons. The flat lateral surfaces enable a much closer packaging than would be possible with cylindrical crystals.

As indicated in chapter 1, the correction that can be made for the Doppler shift of a γ-ray is dependent on the precision to which its trajectory is known. Ideally, the frontal surface of each detector in an array should be as small as possible in order to increase the granularity of the array. However, reducing the volume of the crystals causes an efficiency loss, due to the rise in dead volume, and increases the complexity of the array, as each detector needs to be cooled and the signals read out individually. Alternatively, each detector can be divided into subvolumes, incurring in no loss of efficiency and no increase in the complexity of the cooling arrangement. The CLUSTER detector does not offer a particularly high granularity for the array, since it uses crystals close to the largest presently available. The granularity can nonetheless be increased by segmenting the outer contact, dividing the detector into wedge-shaped subvolumes. A further increase

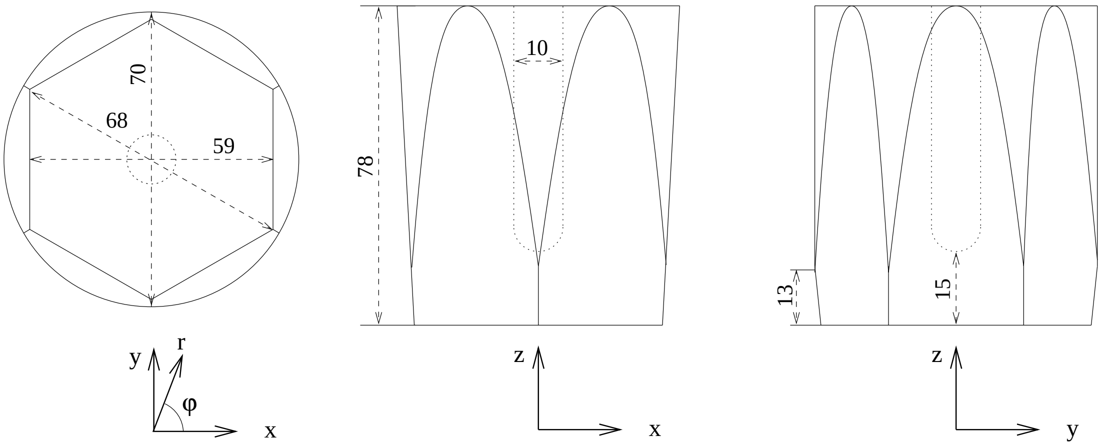

Figure 3.1: Geometry of the CLUSTER crystal. The core hole is indicated with a dotted line. All measures are indicated in mm. The Cartesian and cylindrical coordinate systems used for the interaction positions are also introduced, with their origins at the frontal hexagon. Note the lack of rotational symmetry around the z axis, unlike the detector geometries shown in Fig. 2.4. The electric and thermal connections (not shown) are made at the back of the detector (largest z).

in the granularity of the array can be achieved by dividing the detector into radial regions, e.g. by using the methods described in chapter 2. Fig. 3.2 shows the increase in granularity between an unsegmented crystal and a segmented detector divided into four radial regions. For a recoil velocity $\beta = 4.5\%$, typical for MINIBALL experiments [Ebe97], an improvement in the energy resolution from 15 to 7 keV at 1333 keV, for detectors placed at 90° relative to the emitting nucleus trajectory, is expected as a result of the increase in granularity achieved with a radial resolution of 10 mm and the six-fold segmentation. While this improvement does not completely re-establish the intrinsic resolution of germanium detectors ($\simeq$ 2 keV at 1333 keV) at these high recoil velocities, it nevertheless represent an improvement by a factor of two.

A first attempt at dividing the outer electrode into multiple contacts [She74] achieved the division by cutting out material between contacts in a true coaxial

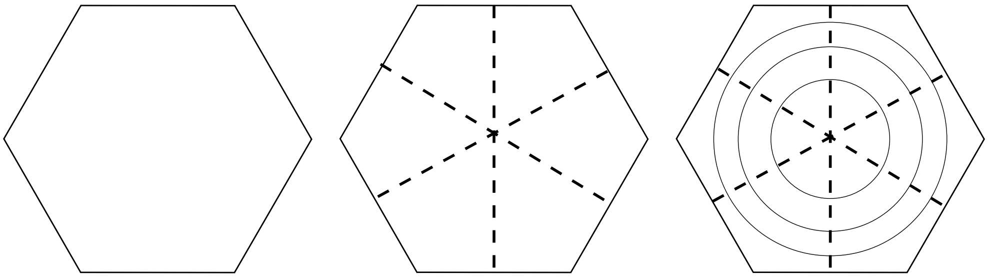

Figure 3.2: Increase in granularity as a result of segmentation and radial resolution in a CLUSTER crystal

Ge(Li) crystal. This solution removes a significant detector volume and thus diminishes the efficiency of the crystal. Furthermore, the segmentation was not retained after a few annealing cycles, performed to re-establish the energy resolution after neutron damage.

With HPGe detectors, it is possible to exploit the high resistivity of the intrinsic material between segments to achieve the isolation between contacts. A mask prevents the ions used for implanting the outer contact from impinging onto the material between segments. Since this subdivision involves little dead volume ($\lesssim 10$ mm^3) between subdetectors, it does not imply a loss of efficiency or quality in the energy spectra. The distance between outer contacts is small enough to leave the fields unaffected for the vast majority of the crystal volume. The lithium atoms used for implementing the p^+ contact drift into the intrinsic volume when the detector is annealed, establishing electrical contact between segments after several temperature cycles. Therefore, p^+ contacts are not suitable for segmentation and thus only n-type crystals can have their outer contact segmented.

The CLUSTER modules have been chosen as a firm candidate for the MINIBALL project, and were selected for the development studies of the outer electrode segmentation with a distance between contacts of a few 100 μm. Photolithographic processes of the type used in the manufacture of integrated circuits cannot be employed, since the residues left in the material compromise not only the purity of the crystal but also the vacuum needed to operate the detector. Therefore, this process has been replaced by a cleaner method. The isolation between the outer electrodes and the capsule as well as the high vacuum feed-through connectors required for the additional six signals also need to be developed.

As a first step in the evaluation of their suitability for MINIBALL, a two-fold segmented detector was commissioned by the Max-Planck-Institut für Kernphysik and delivered by the company EURISYS Mesures in November 1995. A six-fold segmented prototype was delivered to the group at the Ludwig-Maximilians-Universität in Munich in March 1997 and is currently being tested [Fis97].

The collimator

In order to limit the detector volume irradiated, a collimator has to be used. As seen in chapter 2, no material completely stops all γ-rays for any energy. Therefore, a number of compromises have to be met in the design of the collimator [Gun97]. A short reminder is given in this section.

There is always a non-zero probability that a γ-ray will traverse the collimator unaffected. The more energetic the γ, the higher the probability becomes. The unavoidable fraction of events that reach the detector outside the desired positions is the parameter that must be minimised. Furthermore, the beam exiting the collimator is not parallel but conical and the minimum distance to the front of the detector, as dictated by the cryostat geometry, is 7 mm. The collimator will be used with energies up to 1333 keV and will necessarily be rather thick and very heavy. Due to its weight, the collimator cannot be rested on the thin cryostat wall and the minimum distance is thus larger than the ideal value of 7 mm. A reduction in the divergence of the beam can be obtained by increasing the distance between the source and the frontal surface of the detector, at the expense of count rate at the detector. A higher activity source can be used in principle to increase the count rate, but radiation doses above 10 μSv were avoided for radiation protection reasons.

The collimator designed concentrates 60% of the 1333 keV γ-rays that reach the detector on a circular spot of 4 mm radius at the front of the detector and 85% on a 6 mm spot. The percentages increase to 89% (4 mm) and 100% (6 mm) for 662 keV γ-rays. Count rates of several hundred Hertz have been measured with 100 μCurie sources.

3.2 Electric field calculation

Due to the complex geometry of the crystal, Poisson's equation (2.21) can only be solved numerically. In contrast to the traditional closed ended coaxial geometries, CLUSTER crystals do not have rotational symmetry; they do however present six planes of symmetry. The aim of the calculations described in this chapter is to produce the event current pulses for different energies, tracking the charge clouds set free by the interactions. The symmetry of the crystal would allow solving just a sixth of the total volume. The program used to solve the electric fields, however, works with a Cartesian mesh and the quadrant defined by $x \geq 0,\ y \geq 0$, according to the coordinate system defined in Fig. 3.1, was selected to perform the calculations. The boundary surfaces are thus parallel to the axes and when the charge cloud crosses one of the boundary planes, the symmetry of the problem enables simply mirroring the corresponding coordinate relative to the boundary crossed. The detector is made from n-type material and will be considered as such for the solution, but a p-type detector with the same impurity concentration would have the same electric field strengths. Only the field direction would be reversed, meaning that holes drift to the central electrode and electrons towards the outer contact. The biasing voltage was applied at the central contact and the outer electrode held at 0 V, reproducing the operating conditions of the encapsulated CLUSTER modules.

A number of approximations have been made to simplify the solution of Poisson's equation. They are described in the following two subsections. Their relevance for the calculations that use the fields has been tested by comparing the results with those of a set of two dimensional solver programs [Gun97]. The calculated sections by these solver programs correspond to the planes at $x = 0$ and $y = 0$ and a circle and a hexagon for the cross-sections perpendicular to the z axis. The results for other cross-sections with more complicated geometries, can be considered intermediate between two of these cross-sections.

3.2.1 Basic approximations for solving Poisson's equation

A number of programs were considered for solving the two electric fields required in order to calculate the current pulses generated as a response to a γ-detection. Only Poiscr [CER84] and Mafia [Wei93] were found to accept both a charge density and the electrode voltages as input. Poiscr is restricted to two dimensional problems, so Mafia was selected to perform the calculations, as CLUSTER crystals do not present rotational symmetry.

An approximation regarding the contacts was made for the solution of Poisson's equation due to the limitation in Mafia of accepting just one charge density for the whole volume studied: the contacts were considered surfaces of ideal conductors. In reality, both contacts present a concentration of donors in the n^+ contact, or acceptors in the p^+, much higher than the carrier concentration in the intrinsic region of the crystal. When the crystal is completely depleted, the charge on the rectifying contact is equal to the space charge induced in the intrinsic region. The consequences of this approximation became apparent when the concentration of impurities in the active region was increased and even voltages much higher than the corresponding operating voltages of existing detectors [Gut96] failed to deplete the whole crystal. In the calculation, a detector with $N_D = 2.0 \times 10^{10}$ atoms/cm^3 impurity concentration could not be completely depleted even with 8000 V. The non-depleted regions were located in the middle of the active volume and the calculation therefore led to a completely distorted electric field. For all N_D values that could be depleted within the Mafia restriction, the two-dimensional calculations, which included real contacts, resulted in the same regions of saturated drift velocities. Outside of these regions, the difference in field strength translated into a slight decrease in the drift velocity.

3.2.2 Compromises introduced by the solver program

The core hole is circular in section and has a rounded corner. There is a transition from a planar geometry directly in front of the hole ($z < 15$ mm; $r \leq 5$ mm) through a rounded contact to a cylindrical contact (see Fig. 3.1). As established in section 2.3, eqs. 2.29 and 2.43, the product $Q_i \cdot E_{\mathrm{geom}}(r_{\mathrm{contact}})$ determines the value of the maximum current and the minimum of the difference function. If the field strength along the contact varies, as is the case for a varying electrode geometry, the product becomes ambiguous. Hence, the current maximum and the slope minimum depend on the position where majority charge carriers reach the central contact. The field is constant for the coaxial part of the central contact and a charge Q arriving at positions where E_{geom} is higher than in the coaxial part are indistinguishable from a correspondingly larger charge arriving in the coaxial part. The space-charge field in the proximity of the core contact is always above the value that saturates the drift velocities, which are therefore left unaffected.

Mafia is a finite integral program, where the mesh elements are fixed. The geometry of the problem has to be mapped onto a Cartesian mesh and any round surfaces have to be approximated by a succession of cuboids. In order to obtain a realistic result for the fields at the central contact, the sides of the mesh elements close to the rounded surfaces in the detector should be kept as small as possible. The square corners introduced will produce artificially high values for the electric field strength. These artifacts can be kept small if the relevant dimensions of the cuboids are small. The mesh spacings in any one direction are constant over the entire range of the other two fixed dimensions; in other words, the x spacing has no dependence on y and z, and correspondingly for the other axes. A small sided cube at x_1, y_1, z_1 can only be produced by setting the spacing of all elements at x_1, all elements at y_1 and all elements at z_1 to the corresponding length. At the same time, the memory capacity of the computer where the calculation is run limits the total number of mesh elements that can be defined and the 260 MByte memory available for the process running Mafia slightly limited the number of elements that could be defined. The effect on the current pulses generated was checked to be negligible.

At the central contact, the effect introduced by the bevelled surface is amplified by the artifacts due to the Cartesian mesh required by Mafia. As noted above, the square corners introduced in the central contact by the mesh directly affect the amplitude of the electron current. For events that include an interaction with electrons arriving at the bevelled part of the contact, these electric field "spikes" can lead to a false identification of the main interaction. The increase in the space-charge field strength has no effect, since the drift velocity is already saturated.

The complicated geometry of the outer contact is also approximated by a series of rectangular mesh elements. The corresponding increased values of field strength (see Figs. 3.3, 3.4, 3.5) affect the initial current pulse amplitudes for interactions occurring very close to the outer contact or the final values of the hole current when they arrive at one of these steps. The effect on the event current pulses due to the outer surface is however negligible and the considerable increase in mesh elements that would have implied using a finer spacing is not justified.

In order to limit the influence of the mesh spacing on the solution, a spacing of 0.5 mm was chosen for the volume and reduced to 0.1 mm at the rounded surfaces of the core contact. All elements at $x < 6.0$ mm, $y < 6.0$ mm have a square cross section of 0.1 mm side. For 15.0 mm $\leq z <$ 19.0 mm, the side of the elements along the z axis is reduced from 0.5 to 0.1 mm; the cuboids become cubes.

3.2.3 The electrostatic fields

In order to solve the electric fields, an impurity concentration of $N_D = 7.0 \times 10^9$ atoms/cm^3 and a biasing voltage of 3500 V were used. These data correspond to the first segmented crystal delivered by EURISYS. The second crystal was also quoted at 7.0×10^9atoms/cm^3, but only required an operating voltage of 2500 V. The agreement with the measurements was however as good as for the first crystal.

It should be noted that approximating the contacts with ideal conductors resulted in all impurity concentrations requiring depletion voltages in the calculation comparable to their corresponding operating voltages, which are between 200 and 1000 V higher. This increased biasing voltage results in higher electric field strengths for both the geometric and the space-charge fields. The effect of the higher geometric field is a current pulse amplitude slightly larger than that measured and is therefore not qualitatively important. The space-charge field only affects the drift velocities. Since the operating voltage is selected in order to achieve consistent time resolution with the crystal, which implies that the drift velocities are saturated over the whole active volume, the difference in saturated drift velocity regions can be considered minimal. Furthermore, the calculated current pulses have durations in very close agreement with the measured pulses and it can therefore be assumed that the effect of the biasing voltage difference is minimal.

From the field results produced by Mafia it became evident that the mesh spacing is not expected to change along any one axis. But while the fields Mafia calculated presented discontinuities along each axis where the spacing changed, the potential did not suffer such an effect. Therefore, a program was written in the C programming language to calculate the field components from the potential solved by Mafia, see Appendix B, calculate_E. The potential $V(x, y, z)$ is read into a three dimensional matrix and the gradients for each direction calculated on a regular 0.5 mm mesh with a nested loop that scans the z axis for each position of the y axis, in turn scanned for each x position. The transitions on each axis are handled by modifying the distances from the field mesh position to the positions where the potential has been calculated. The "spikes" in the electrostatic fields induced by the mesh are thus smoothed out at the central contact. Depending on the input potential, the program calculates the geometric or space-charge electric field and stores the components in a three dimensional matrix. These fields are then used to calculate the current pulses and the drift times of majority carriers to the central electrode.

In order to examine the fields, two C programs, see r_cut_field and z_cut_field, Appendix B, were written to extract the components and magnitude of the field on surfaces normal to the z axis and for the planes $x = 0$ and $y = 0$. In zcut_field, interpolation is included in order to investigate the field variations along the depth of the detector. The interpolation is performed between the closest eight neighbouring points, the same method used when tracking the charge clouds.

The space-charge field is shown in Figs. 3.3, 3.4. The granularity in the plots is due to the 0.5 mm distance between mesh points. The artificially high values when a round surface is approximated can also be clearly seen at the outer contact. As expected, the sharp corners at the front of the detector ($z \leq 5$ mm, $r \geq 30$ mm) produce volumes with field strengths below the saturation value. These volumes are nevertheless very small (cf. Fig. 3.4) and affect few events. The space-charge field determines the drift velocity, both in direction and magnitude (eq. 2.22). The effect of the artificially high values for the space-charge field strength cannot be observed, since they represent an increase beyond the saturation value for the drift velocities.

The region of the detector where carriers drift only radially can be established by examining E_z (Fig. 3.5). Note that all majority carrier clouds generated at $z \leq 22$ mm drift along the z direction (a non-zero projection of v_d onto the z axis) at some point on their way to the central contact. Conversely, minority carrier clouds will stop drifting in the z direction when they enter the low E_z region of the detector.

Charge carriers drift under under the influence of the space-charge field, but the current induced on the electrodes is dependent on the electrostatic coupling, as described by the so-called geometric field. This field is calculated with the same biasing voltage but setting the charge density $\rho = 0$. The results are shown in Figs. 3.6, 3.7. Fig. 3.6 would suggest that the geometric field takes the values from a true coaxial detector for $z > 30$ mm. The influence of the flat side surfaces extends nevertheless much deeper along the z axis, as can be seen in Fig. 3.7. The field is exclusively radial only close to the end of the detector ($z \gtrsim 68$ mm). Therefore, the coaxial part of the detector for the electric fields starts further along the z axis than the geometric coaxial part. From Fig. 3.7, the influence of the sharp hexagon corners is only visible at the very front of the detector.

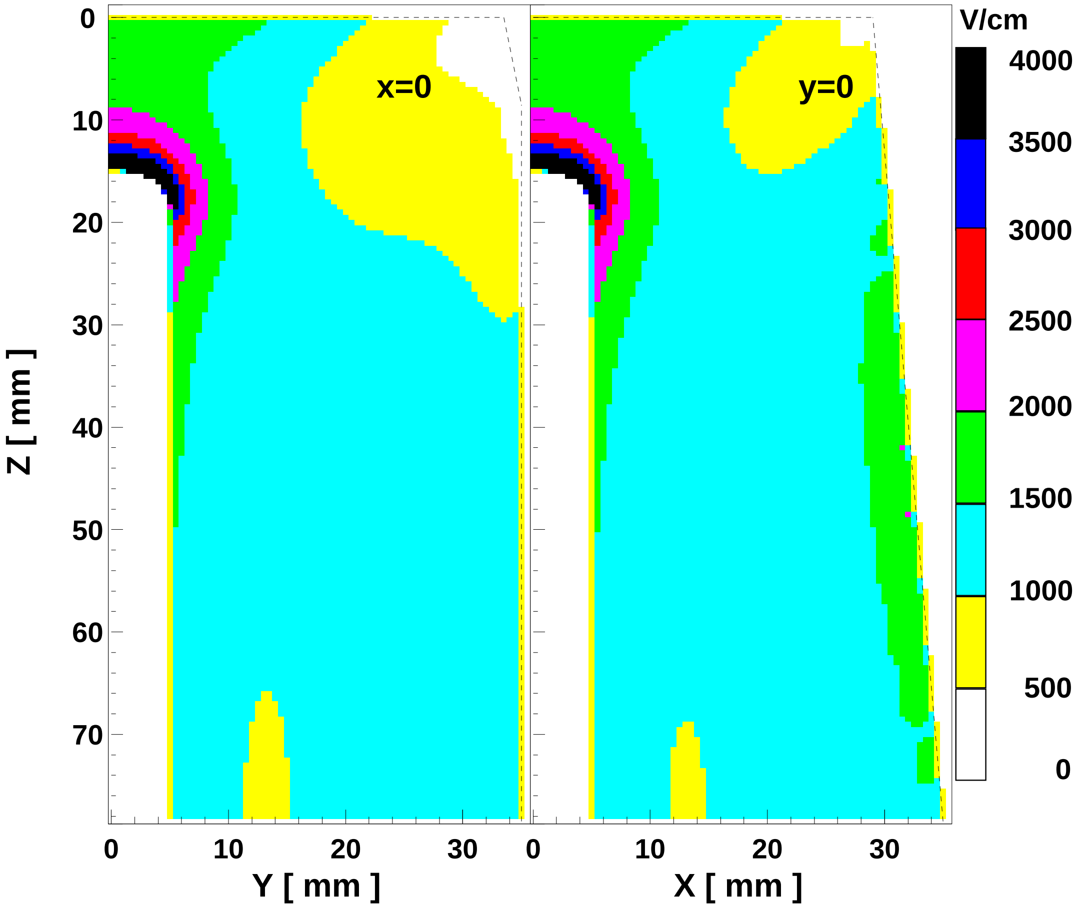

Figure 3.3: Space-charge field for the planes $x = 0$ and $y = 0$ for a biasing voltage of 3500 V and an impurity concentration of 7×10^9 atoms/cm^3. The shape of the detector is indicated with a dashed line.

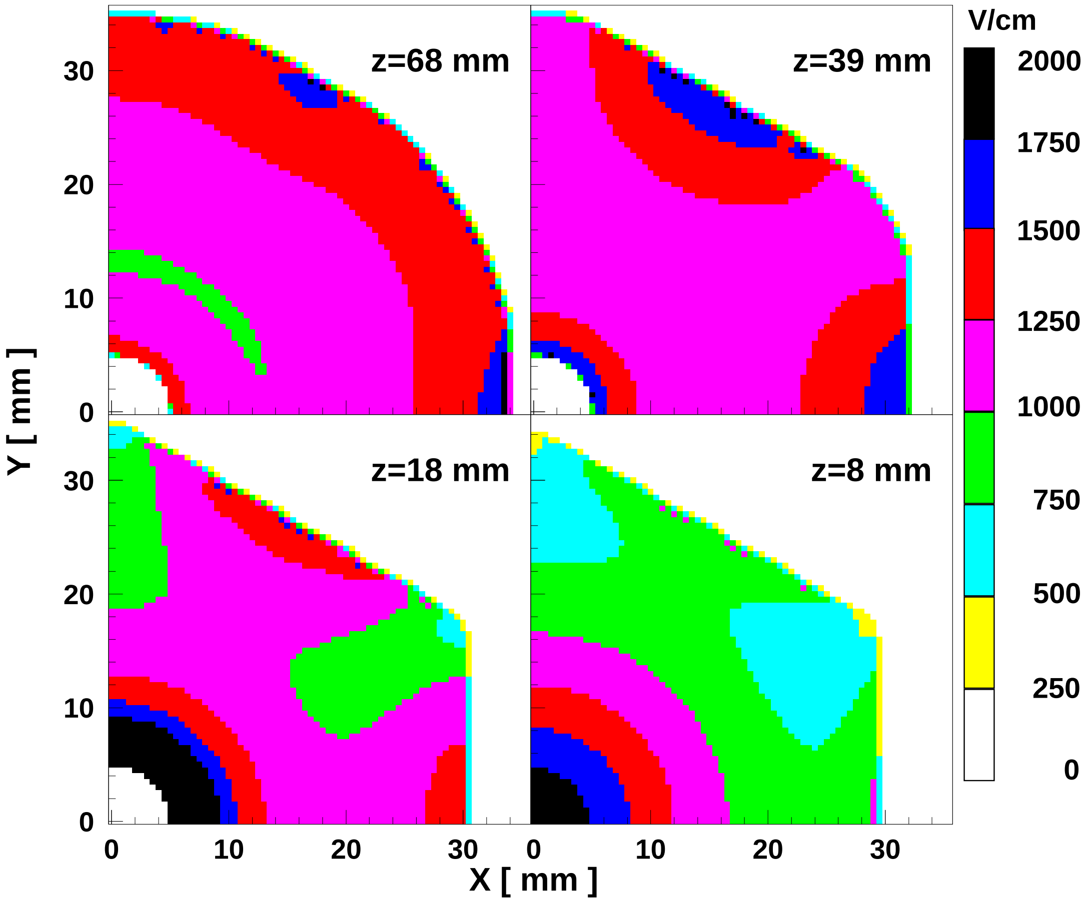

Figure 3.4: Space-charge field for four planes of constant z for a biasing voltage of 3500 V and an impurity concentration of 7×10^9 atoms/cm^3.

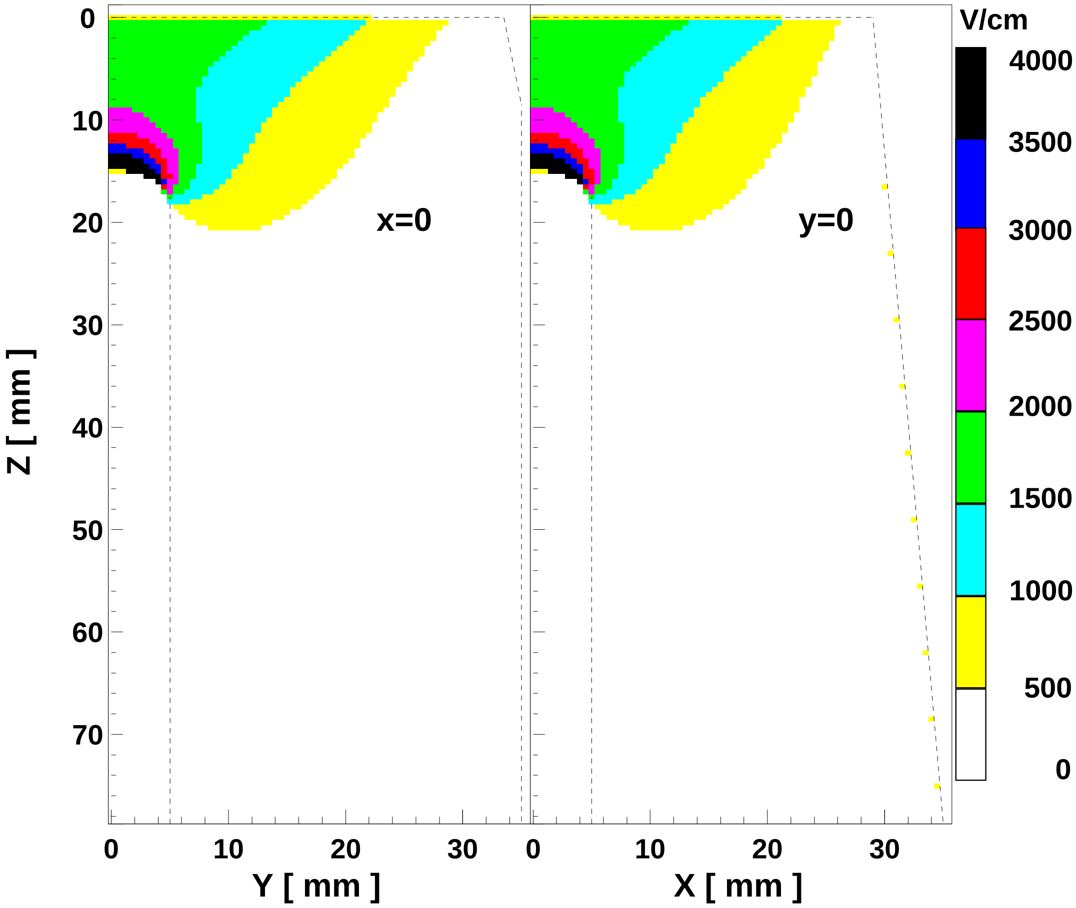

Figure 3.5: Axial component of the space-charge field ($V_{\mathrm{BIAS}} = 3500$ V, $N_D = 7 \times 10^9$ atoms/cm^3) for the planes $x = 0$ and $y = 0$. The physical shape of the detector is indicated with a dashed line.

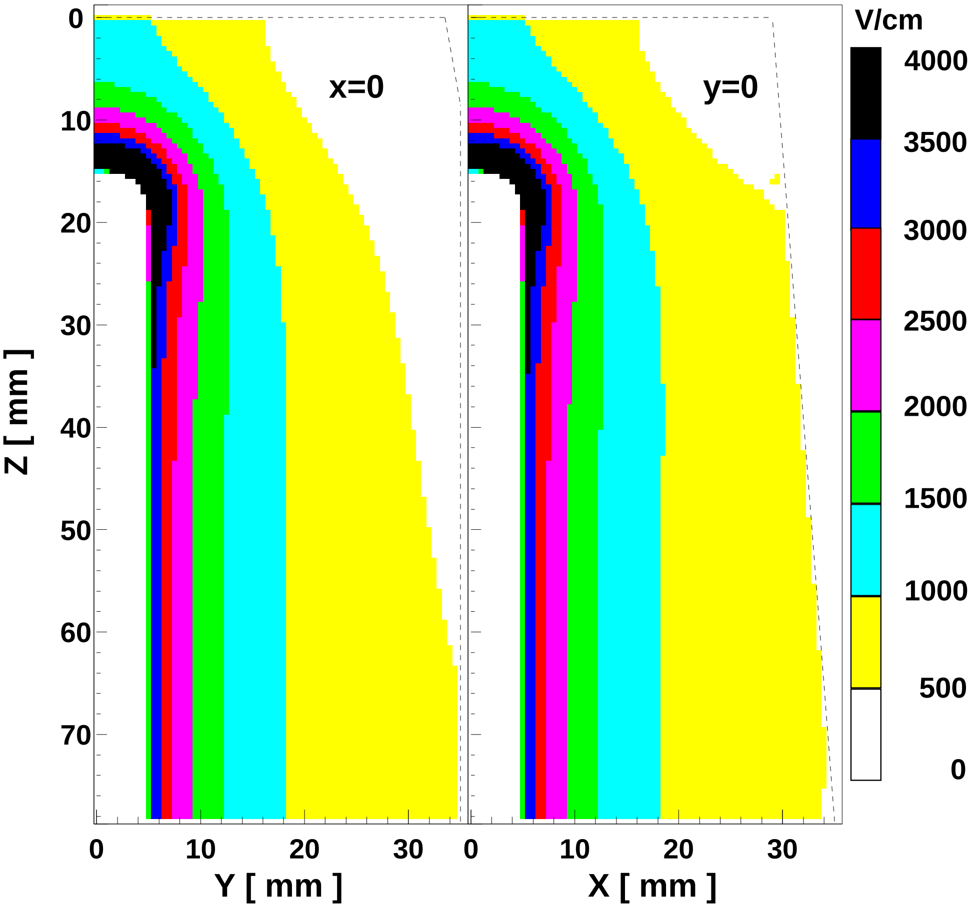

Figure 3.6: Geometric field for the planes $x = 0$ and $y = 0$ ($V_{\mathrm{BIAS}} = 3500$ V).

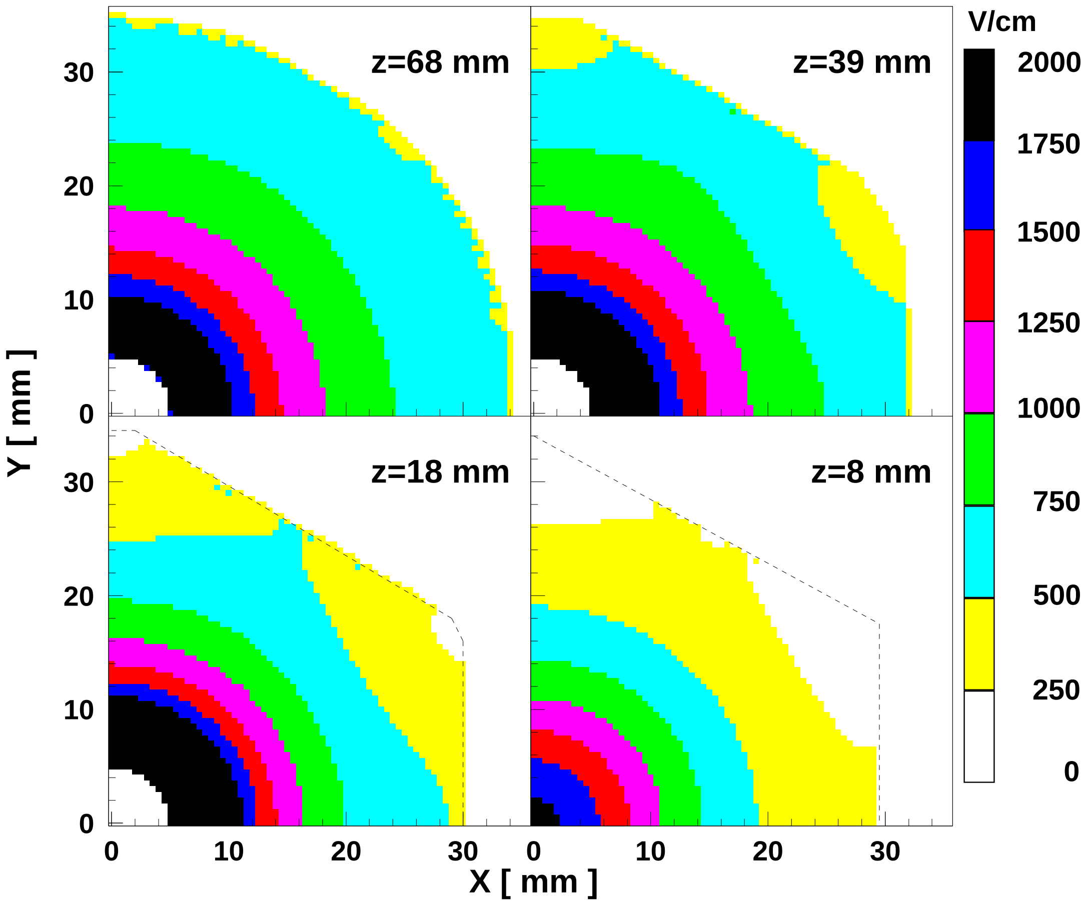

Figure 3.7: Geometric field for four planes of constant z ($V_{\mathrm{BIAS}} = 3500$ V). The dashed line indicates the boundary of the detector where low field strength regions are present.

3.2.4 Calculation of the drift times

The parameter that yields radial resolution is the drift time of majority charge carriers from the interaction point to the central contact. For the CLUSTER modules, the majority charge carriers are electrons and the corresponding drift times will be denoted as t_{drift}. A program, `t_drift` in Appendix B, has been written to calculate the electron drift time distribution in the detector for a given space-charge field. The electron drift times are calculated for a 1 mm Cartesian mesh by tracking a point-like cloud of unitary charge set free at each mesh point. The data are written into a three dimensional matrix $t_{\mathrm{drift}}(x, y, z)$, from where they can be extracted by two programs similar to those already used for examining the electric fields. The results are shown in Fig. 3.8.

Allowing a 2 mm uncertainty for the radial determination, the coaxial part of the detector coincides with the geometric coaxial part. The difference with the coaxial region of the fields indicates that the drift times are rather insensitive to variations in the field strength. Examining the drift times on a plane of constant z, the lines of constant drift time are radial for all z values. Since the drift velocity is saturated over nearly the whole detector, the drift times are almost linearly related to the distance from the central contact.

During an in-beam experiment, the drift time of majority carriers from the main interaction of the detected γ-ray will be measured and the entry radius of the γ-ray r_0 has to be determined from t_{drift}. The curvature of the lines of constant drift time makes this determination ambiguous to a certain extent. In the case of irradiation with an ideal line beam perpendicular to the detector frontal surface, the penetration length of the γ-rays determines the distribution of first interactions in the z coordinate. Events with their first interaction at small z produce a tail in the drift time distributions to larger times and result in an ambiguity when the whole frontal surface of the detector is irradiated:

interactions taking place in the part of the detector where the lines of constant drift time are curved are assigned to radii larger than r_0.

For the small volume in front of the core hole ($z < 15$ mm, $r < 5$ mm), this ambiguity is even more pronounced. This part of the detector requires the same majority carrier drift times as the radial interval $[5, 18]$ mm and in this volume, z_γ is mapped onto that radial interval almost linearly. For uncollimated irradiation, however, this volume subtends a small solid angle relative to the target compared to the rest of the detector. Therefore few events when the whole frontal surface is irradiated will have their first interaction in this volume and it can be considered unimportant for in-beam experiments.

With a collimated source, the beam divergence will also contribute to the shape of the drift time distributions. At higher energies, more γ-rays traverse the collimator material unaffected and scattering dominates an increasing fraction of full energy events. The different contributions to the calculated t_{drift} distribution for a given collimator position can be evaluated with the aid of the distribution for an ideal line beam of the same γ-energy positioned at the same radius. An approximate linear correlation between the drift time and the interaction radius of 10 ns/mm can be established for the coaxial part of the detector and the indicated operating conditions. The next step is to investigate the dependence of the majority carrier drift time on the impurity concentration and the biasing voltage.

Neutron damage introduces lattice defects in the germanium crystal. These defects are equivalent to an increase in impurity concentration, and the effect of this parameter on the drift times was investigated in order to evaluate the possible changes in drift times when the detector is exposed to neutrons. Due to the approximation for the contacts, the increase in charge density had to be matched with a higher biasing voltage (see section 3.2.3). This limited the impurity concentrations that could be studied without compromising the validity

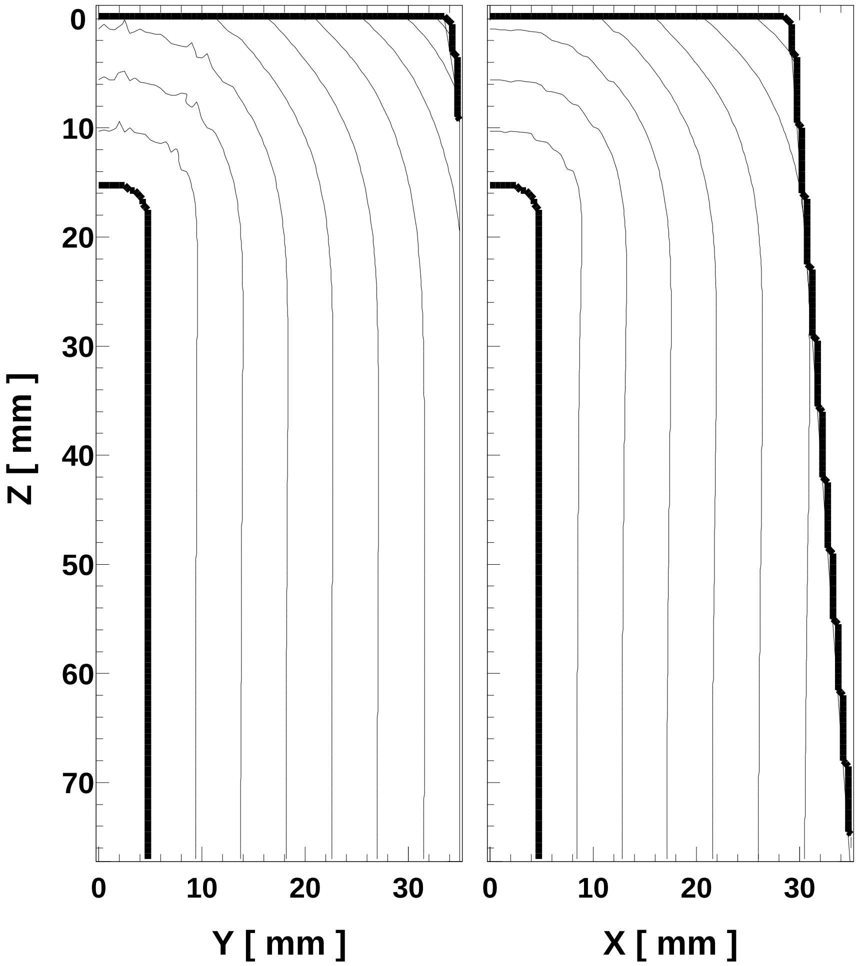

Figure 3.8: Calculated electron drift times for the planes $x = 0$ and $y = 0$ in an n--type CLUSTER crystal with 7.0×10^9 impurities/cm^3 and 3500 V biasing voltage. The lines are 50 ns apart. The contacts are indicated by thick lines.

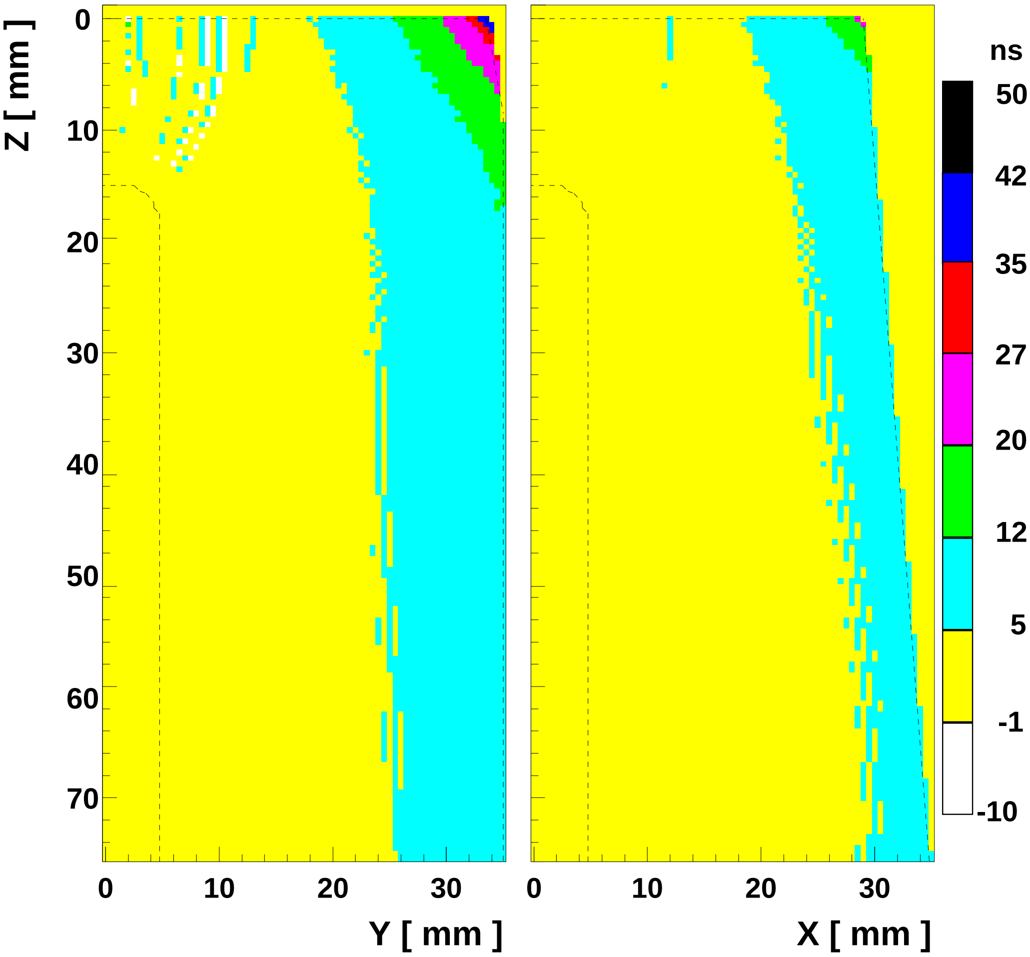

Figure 3.9: Maximum difference in electron drift times between 0.7 × 10^{10} atoms/cm^3, 2500 V and 1.1 × 10^{10} atoms/cm^3, 4500 V. The shape of the detector is indicated with dashed lines.

of the results to $N_D = 1.1 \times 10^{10}$ atoms/cm^3.

For $N_D = 7.0 \times 10^9$ atoms/cm^3, the lines of constant drift time become parallel to the central contact in the coaxial region for voltages above 2500 V. The differences between 2500, 3000 and 3500 V biasing voltages are minimal, with the constant drift time lines being displaced by less than 0.5 mm and a minimum decrease in t_{drift} values. For a concentration $N_D = 1.1 \times 10^{10}$ atoms/cm^3 and biasing voltages of 4000 and 4500 V, the calculated drift times become only slightly longer by at most 10 ns, roughly equivalent to a 1 mm displacement. Fig. 3.9 shows the differences in electron drift times for detectors with $N_D = 7.0 \times 10^9$ atoms/cm^3, 3500V and $N_D = 1.1 \times 10^{10}$ atoms/cm^3, 4500 V, respectively. The maximum difference is 40 ns, roughly equivalent to 4 mm; typical differences are about 10 ns, leading again to a radial uncertainty of less than 1 mm.

The low sensitivity to impurity concentration variations indicates that neutron damage will hardly affect the drift times and thus the position resolution. In fact, assuming a homogeneous distribution of lattice defects, trapping will be proportional to the distance covered by the charge carriers and may be compensated through radial determination. The differences in the calculated drift times suggest that the same calibration can be used for a number of detectors, provided that their impurity concentrations are similar. Furthermore, the calibration for the radial position, a necessarily time-consuming process, must only be carried out once for each detector.

Measuring the drift time of majority charge carriers therefore provides a linear correlation to the radius of the interaction, even though the field profile in the crystal produces small ambiguities. The next step required in order to establish the radial resolution that can be expected is to examine the distribution of the event energy among the different interactions, which will be done in the following section.

3.3 Monte Carlo simulation

Despite the importance of the energy distribution among the individual interactions in an event, no detailed study is available in the literature. Therefore, a thorough Monte Carlo simulation using the GEANT 3.21 code [CER93] has been carried out. The simulation outputs the energy and coordinates of each interaction involved in an event. These data will be used to produce the corresponding event current pulses in the next section. In this section, they will be analysed to study the distribution of energy among interactions as a function of γ-energy and irradiation position in order to establish a target for the number of events whose entry position in the detector can be reconstructed within a certain accuracy.

The calculations can be divided into two parts: using an ideal line beam and using a point source together with a collimator. In both cases, the γ-rays are perpendicular to the front face of the detector. The calculations were performed for various energies corresponding to different γ-source lines between 122 and 1836 keV and a minimum of 10^4 full energy events were recorded for each position and energy. The results are restricted to full energy events, since they are the only events of spectroscopic relevance.

3.3.1 Simulation with ideal line beams

The results obtained by irradiating the detector with an ideal line beam perpendicular to the frontal surface are analysed in this section. These results reflect the underlying physics involved in the detection of a γ-ray and set a target for the best position resolution that can be achieved.

The distribution of the event energy among the different interactions is related to the average number of interactions that a full energy event requires. It varies between 1.4 interactions at 122 keV to 4.5 at 1836 keV and shows little dependence on the irradiation radius r_0. The number of interactions however contains little information about how localised the energy deposition is: Two interactions occurring close to one another will count as separate interactions, even though they will be very difficult to resolve in reality.

In order to reconstruct the direction of a γ-ray of known origin, it is sufficient to determine the coordinates (r_0, φ_0) or (x, y) where the gam-ray crosses the frontal surface of the detector. For γ-rays impinging perpendicular to the front face, (r_0, φ_0) will be identical to the coordinates (r_1, φ_1) of the first interaction. The methods discussed in section 2.3.1, however, determine the position of the main interaction. It is therefore important to investigate how well (r_1, φ_1) can be determined in principle by measuring the main interaction coordinates $(r_{\text{main}}, \varphi_{\text{main}})$. The parameter that can be resolved by measuring the majority carrier drift time is the distance to the central electrode is r_{main}. If a γ-ray is scattered at one position and the secondary photon undergoes a photoelectric absorption at exactly the same distance from the central contact, the current pulse produced is indistinguishable from that resulting from a photoelectric absorption for the full E_γ at one of the positions. Only in combination with the φ resolution from the segmented outer contact can the entry point of these events be determined.

Fig. 3.10 shows the localisation of the energy deposition for full energy events as a function of energy. The fraction of events where the first is also the main interaction is presented in Fig. 3.10(a). This fraction depends on the energy of secondary photons and the detector efficiency for stopping them. As the γ-energy increases, the range of secondary photons decreases and the largest fraction of the event energy can be deposited in the second or third interaction. For even larger energies, the efficiency for detecting those high energy secondary photons decreases and only events where the first interaction deposits a large fraction of E_γ become full energy events. The fraction of events with coinciding first and main interactions present no problem for the determination of their entry position.

For events where the first interaction is not the main interaction, Fig. 3.10(b) displays the fraction of main interactions that take place less than $\Delta_{xy} = \sqrt{(\Delta x)^2 + (\Delta y)^2} = 5$ mm away from the entry point[1]. The total fraction of events that can ideally be resolved within 5 mm of their entry point is shown in Fig. 3.10(c). This fraction is obtained by adding the fractions shown in Fig. 3.10(a) and (b) and remains above 60 % except between 200 and 500 keV and reaches values about 80 % for energies ≥ 800 keV. For the volume in front of the core hole ($r < 5$ mm) the fraction is smaller, but due to the small solid angle it subtends and to its low γ-detection efficiency, this part of the crystal has little significance for in-beam experiments. The events with main interactions further than 5 mm away from the entry point cannot be easily characterised and the Doppler correction that they will receive will be less correct as Δ_{xy} increases. The quality of the correction is however also dependent on the the detector-target distance and angle and γ-energy, therefore preventing a meaningful general assessment of the correction.

This work is mainly concerned with the determination of the entry radius r_0 and the radial resolution for events with separate first and main interactions is limited by the average radial distance for full energy events with separated main and first interactions, as shown in Fig. 3.11. The distance rises steeply with energy but settles at about 5 mm for most irradiation radii r_γ. For large radii, it rises again to 6 mm due to the limited solid angle covered by the rest of the detector as seen from the entry position.

---

[1] The largest Doppler peak broadening is observed when the detector is positioned at 90° relative to the target and takes the value $(\Delta E/E) = \beta \cdot \Delta\theta_\gamma$, where $\Delta\theta_\gamma$ is the opening angle of the detector element. The value of $\Delta_{xy} = 5$ mm corresponds to less than $0.1\,\beta$ in a CLUSTER module under the foreseen MINIBALL detector–target distance and is chosen as a tentative aim for the position resolution.

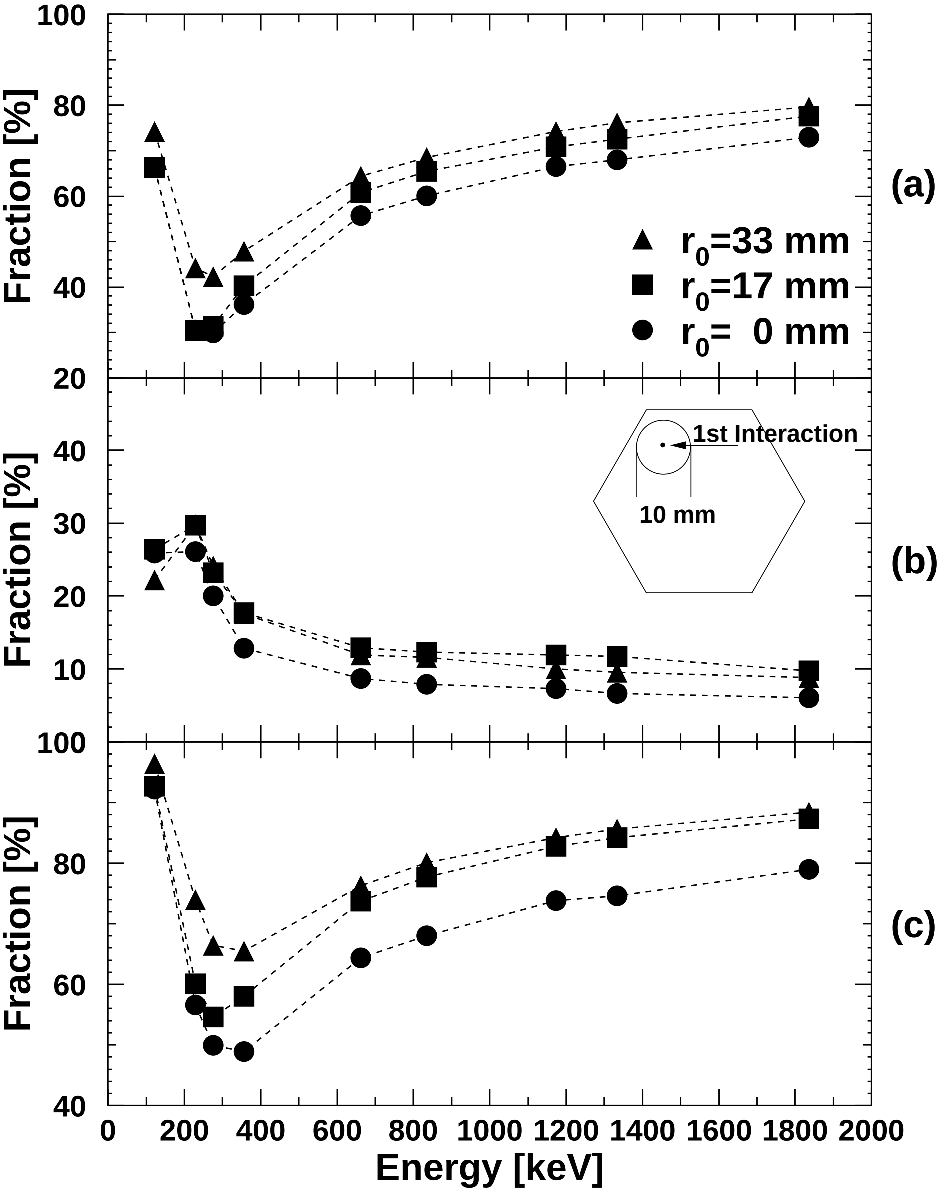

Figure 3.10: Distribution of the energy for full energy events in the xy plane for ideal line beams positioned at the indicated radii r_0: (a) shows the fraction of total events where the first is also the main interaction, (b) depicts the fraction of total events where the first interaction is not the main interaction and the distance between the first and main interactions is $\Delta_{xy} \leq 5$ mm and (c) shows the fraction of events whose entry radius can be determined with 5 mm resolution by determining the radius of the main interaction.

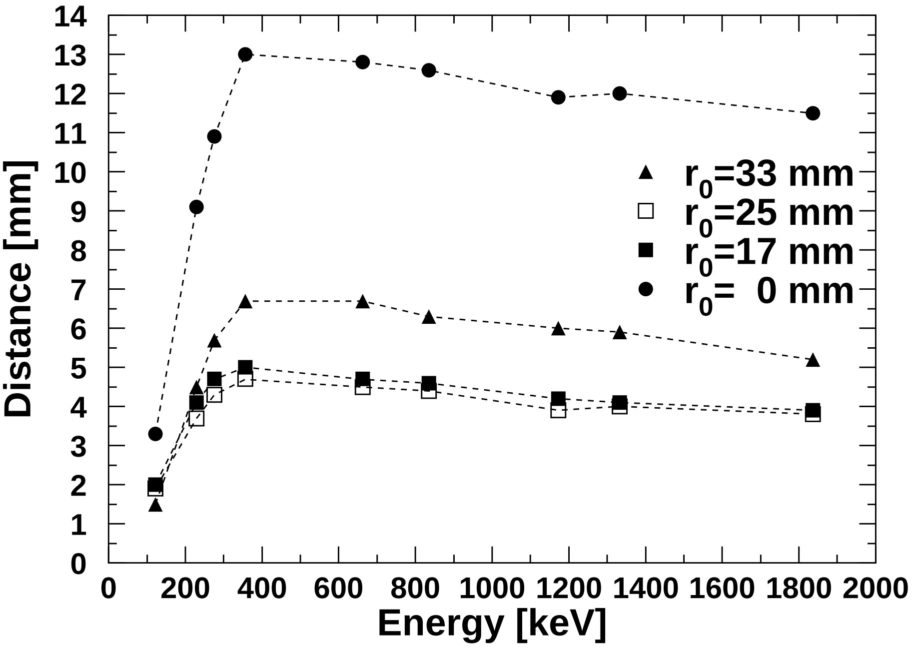

Figure 3.11: Average radial distance $<|r_1 - r_m|>$ between first and main interactions for different irradiation radii r_0 for events where the first interaction is not the main interaction.

3.4 Current pulse calculation

The events output by the Monte Carlo simulation can be used to calculate the corresponding current pulses generated by the detector. A program was written (see pulses_3D in Appendix B) that reads the files output by GEANT and calculates the corresponding current pulse for each event.

In this program, the electric fields are read into two three-dimensional matrices that are used to interpolate the values for each position of the charge clouds. Then, the file with the interaction positions and energies for each event is read, one event at a time. Each interaction is treated separately and the two corresponding currents calculated. The point charge clouds are followed as they drift to the electrodes with a time step $T = 1$ ns. From the values of the saturated drift velocities, this time step corresponds to a displacement below 0.1 mm, an order of magnitude smaller than the expected position resolution of a few millimetres. This displacement corresponds to small variations in the space-charge field and the drift velocity can be assumed to remain constant between the positions where it is calculated. The fields are calculated for the coordinates of the cloud at time $t = kT;\ k \in \mathbb{N}$, $\vec{r}(kT)$, and used to determine the drift velocity according to eq. 2.22. The program then solves

$$i_\nu(kT) = Q_i \frac{1}{V_{\mathrm{BIAS}}} \vec{E}_{\mathrm{geom}}(\vec{r}(kT)) \cdot \vec{v}_{d_\nu}(\vec{E}(\vec{r}(kT))) \ , \tag{3.1}$$

$$\vec{r}((k+1)T) = \vec{r}(kT) + \vec{v}_{d_\nu}(\vec{E}(\vec{r}(kT))) \cdot T \tag{3.2}$$

and iterates further until the cloud has reached the corresponding contact. The initial condition is $r(0) = r_i$. At the same time, a record of the electron drift time is kept. Once all the interactions in an event have been processed, the main interaction is determined and the electron drift time histogram correspondingly incremented. The event current pulse is then processed according to the methods explained in chapter 5. Since up to 10^4 events may be processed, a monitoring mode has been included that stores the first 100 current pulses for the plotting program. The accuracy of the current pulse calculation is tested by integrating the event current pulses and producing a histogram for the ratio of the charge thus measured to the event energy. The fraction of events with less than 5% error is greater than 95% for all positions and energies.

A few current pulses at the central contact are shown in Fig. 3.12 for events produced by an ideal line beam of 1333 keV impinging at a radius of 25 mm. There is a strong variation in the duration of the event pulses shown, as a result of the variety of interaction positions involved in the events. The low field regions present close to the outer contact are clearly visible in the small values of the decreasing slopes in the minority carrier currents (e.g. between 265 and 275 ns). The minority carrier currents do not end abruptly as expected but present a slowly

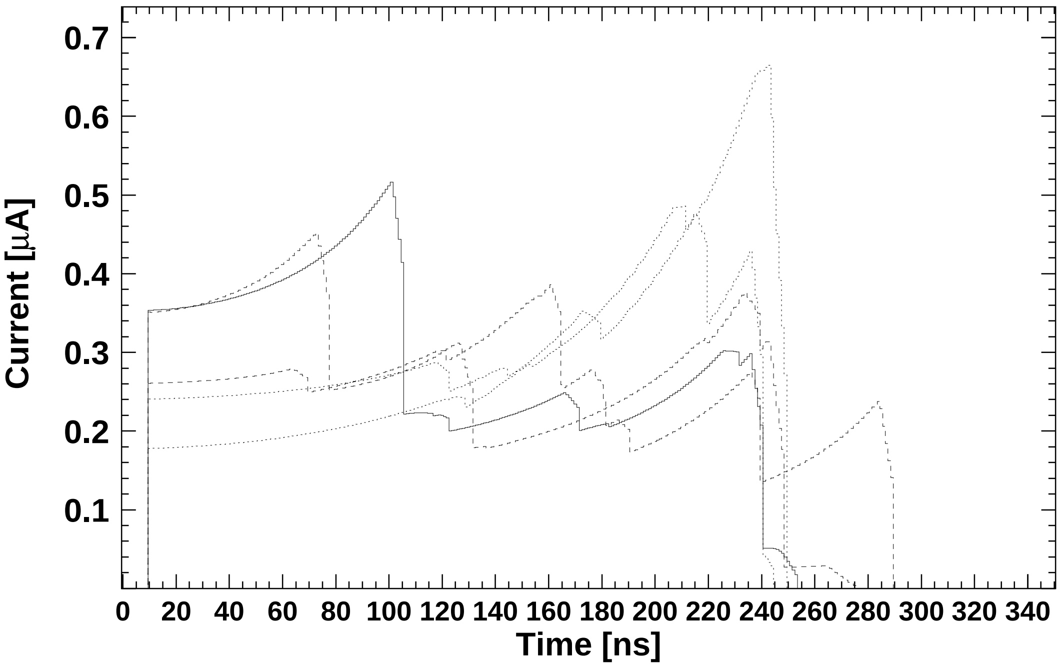

Figure 3.12: Sample current pulses at the central contact for an ideal line beam of 1333 keV incident at a radius of 25 mm when the full γ-energy is deposited in the detector. For clarity, the pulses have been offset by 10 ns.

decreasing slope due to the low drift velocity for minority charge carriers close to the outer electrode. The common characteristic is that all pulses include a contribution that stops after around 240 ns, in close agreement with the expected drift times of majority charge carriers created at $r = 25$ mm ($(t_{\text{drift}}/r) = 10$ ns/mm as established in section 3.2.4). The steepest slope algorithm would either determine the correct entry radius or a neighbouring radius.

Note the wide variations in the position of the absolute maximum. In those pulses where the absolute maximum does not correspond to the irradiation radius, it occurs earlier in the pulse and a radius smaller than the entry radius is assigned to this event. The radial distribution of events for uncollimated irradiation will therefore be biased towards small radii.

The main interaction electron drift time distributions corresponding to irradiation radii of 0, 9, 17, 15 and 33 mm with an ideal line source can be seen in Fig. 3.13. The tails in the distributions towards longer drift times are larger than to shorter t_{drift} due to two factors. There is a contribution from the curvature of the constant t_{drift} lines, since majority charge carriers from main interactions occurring outside the coaxial region require longer drift times before reaching the contact. For higher γ-energies, the fraction of events whose main interaction takes place in the coaxial part of the crystal increases and with it the fraction of events at the median t_{drift}. Furthermore, the contribution from scattered events is biased towards larger drift times as a result of the larger detector efficiency at larger radii.

The shape of the distributions at 122 keV reflects the penetration depth of the γ-rays. At 8 mm, an "island" of constant drift time is formed close to the contact surface, leading to the clear peak. At all other energies, the distributions of events corresponding to placing the ideal line source at 0 mm are hardly visible between 0 and 40 ns. The penetration depths of these events correspond to drift times in a radial interval close to the central contact and present a maximum value much smaller than the peaks visible at other impinging radii.

Fig. 3.14 shows the distribution of calculated drift times for two energies when the collimator is employed. In addition to the tails resulting from the distribution of main interaction positions, the principal effect of the collimator is to broaden the peaks as a result of the radiation beam divergence.

The distributions in Fig. 3.14 are the target for the measurements described in chapter 6. Setting the borders between four radial zones every 100 ns, the irradiation positions would be correctly assigned for about 70 % of the events, varying between 67 % at 9 mm and 662 keV to 75 % for 25 mm and 1333 keV.

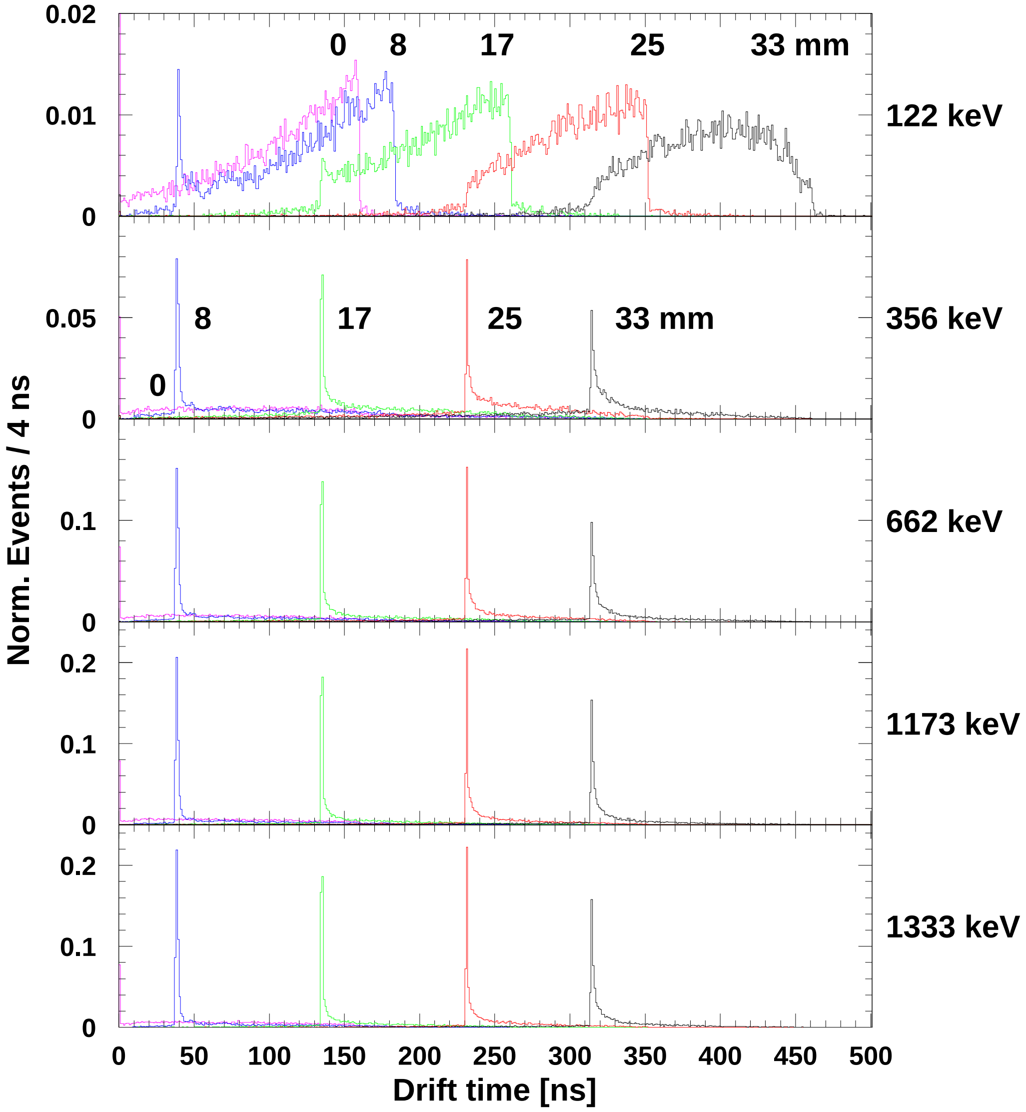

Figure 3.13: Distribution of electron drift times from the main interaction using an ideal line source placed at five different radii and perpendicular to the frontal crystal surface. Only events depositing the full γ-energy are shown.

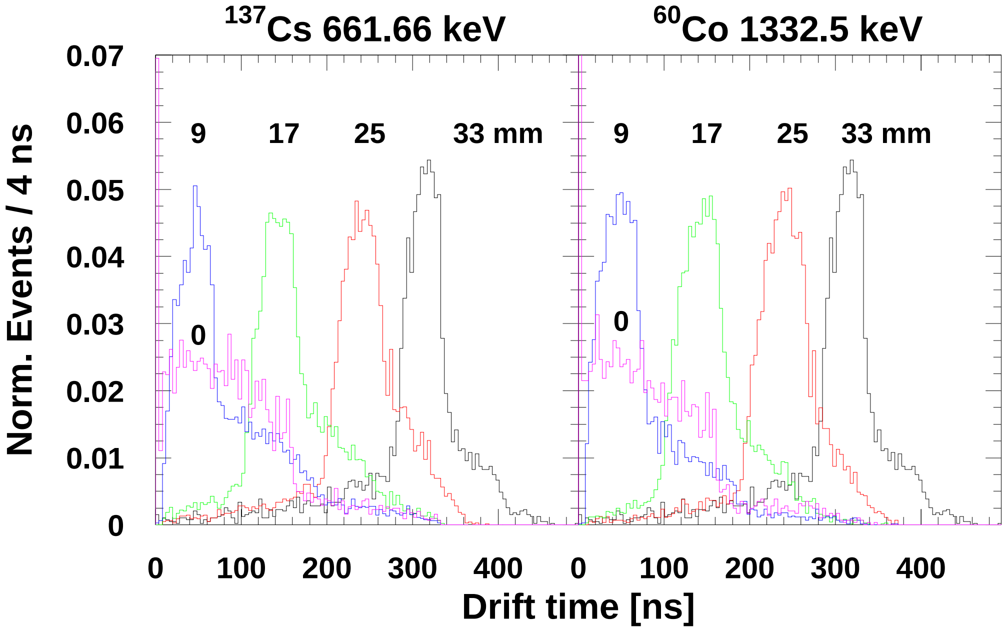

Figure 3.14: Distribution of main interaction drift times for five positions of the collimator and two energies. Only full energy events are shown.

The frontal surface of the whole detector can thus be divided into a disc of 9 mm radius and three 8 mm rings as indicated in Fig. 3.2. The desired increase in granularity can therefore be achieved by measuring the drift time of electrons from the main interaction to the central electrode, although the influence of the electronics has not been considered.

Chapter 4

Signal processing for position determination

Before presenting the results of applying the new steepest slope algorithm (introduced in section 2.3.1) to the calculated event current pulses (see section 3.4), other methods described in the literature for position resolution in coaxial germanium detectors must be considered. Older reports [Str72, She74] studied the use of a germanium crystal for medical in-vivo imaging of organs, whereas more recent research [Esc94, Krö96] has been directed towards exploiting position resolution to improve the energy resolution of HPGe detectors in γ-spectroscopy studies.

Chapter 3 introduced the steps required to establish a target for the position resolution that can be achieved with a CLUSTER module. A Monte Carlo simulation was performed and the positions and energies of the interactions in an event used to calculate the corresponding event current pulses. The same data is used in this chapter to test the applicability of the different methods available for determining the entry position of γ-rays in a germanium detector. The calculated event current pulses with the collimator positioned at $r = 0$, 9, 17, 25 and 33 mm and ^{57}Co, ^{137}Cs and ^{60}Co sources, with lines at 122.0614, 661.660, 1173.238 and 1332.502 keV, are processed according to the reproducible algorithms presented in the literature and to the steepest slope method (`pulses_3D` in Appendix B), enabling a preliminary comparison. The methods that can in practice be used in in-beam experiments will be compared in chapter 6 with measured events.

4.1 Previous work

4.1.1 Medical Imaging

The work by Strauss and Sherman [Str72, She74] is the first study in the literature of position resolution in germanium detectors. They used true coaxial, lithium drifted germanium detectors (50 mm diameter and 20 mm length), with grooves of material close to the outer contact removed in order to provide angular resolution. For this application, the distribution of the event energy among interactions is crucial for the quality of the resulting images and therefore only low energy sources, ^{57}Co and ^{99m}Tc with lines at 122.0614 and 140.511 keV, where photoelectric absorption dominates, were employed.

The parameter measured for extracting the entry radius of the γ-ray was the difference between the fall- and rise-times of the event current pulse. A fixed amplitude (V) pulse is started when the current pulse crosses a threshold and stopped when it reaches a higher threshold. A pulse of amplitude $-V$ is produced while the decreasing current pulse falls between the same two threshold values. Integrating both pulses after each other, the final result is proportional to the difference between the event current pulse rise- and fall-times. The distribution of events as a function of the measured time shows a peak with FWHM $\leq$ 1 mm, which is approximately the width of the collimator spot used, and these peaks are completely separated from one another when the collimator radius is incremented in 5 mm steps. The linearity of this method for the energies studied is very good with a maximum deviation from a straight line of only 0.5 mm. No interdependence between the radial and angular resolution could be established, as would be expected from the electric field present in a true coaxial crystal.

At the limit when the thresholds are set to 0 and 100 % of each single interaction event current pulse, the measured rise-time would become the drift time of majority charge carriers $t_{\mathrm{drift}_{maj}}$. When minority charge carriers drift for a longer time than majority carriers, the fall-time would measure the difference between minority $t_{\mathrm{drift}_{min}}$ and majority carrier drift times. This method could therefore be expected to partly differentiate between the planar and coaxial part of a closed ended crystal (see Fig. 3.8). The meaning of the fall-time is however unclear for positions where $t_{\mathrm{drift}_{min}} < t_{\mathrm{drift}_{maj}}$, since the measured rise-time then also becomes the duration of the event current pulse, which theoretically stops abruptly at $t = t_{\mathrm{drift}_{maj}}$.

Although the method was implemented using analogue electronics and a simultaneous determination of the entry radius and the event energy would thus be possible, the extension to multiple interaction events, which dominate for the γ-energy range of interest for Doppler correction, is by no means clear. Furthermore, having to deal with more than one energy would require establishing a number of threshold values bearing in mind the several edges present in multiple interaction events. For these reasons, this method was not included in the tests reported in chapter 6.

4.1.2 The time to maximum method

Position determination in germanium detectors by measurement of the time t_{max} taken by the event current pulse to reach its absolute maximum (see section 2.3.1) was investigated by the nuclear structure group at the Max-Planck-Institut für

Kernphysik in Heidelberg [Sch92] and independently at the Lawrence Berkeley Laboratory [Gou94]. The two groups used different methods for measuring the t_{max} parameter: Schwebel [Sch92] sampled the current pulses and performed the digital pulse shape analysis off-line while the Berkeley group designed an analogue circuit to determine the absolute maximum of the event current pulse and measured t_{max} with a time-to-amplitude converter. Unfortunately, no results regarding the radial resolution achieved have so far been published by the Berkeley group and both approaches cannot be compared.

The time to maximum method reported in [Sch92] achieved a resolution of $\simeq 8$ mm at 356 keV with a 50 mm diameter detector. Using commercial electronics, the detector current pulses were integrated by the charge sensitive preamplifier and then differentiated with a timing filter amplifier. The integrated–then–differentiated current pulses were sampled with an ADC at 250 MHz and stored on tape as part of the event data. Off-line, the absolute maximum of the pulses was determined by fitting a parabola to the sampled data and measuring the maximum of the fitted function relative to the beginning of the pulse. This method cannot realistically be implemented on-line and was simplified to scanning the ADC values for the tests reported in chapter 6. Even though the processing time was therefore reduced considerably, the method would still require dedicated hardware, digital as opposed to the analogue solution from Berkeley, in order to deliver the radial information within the 10 μs available for measuring the event information. Due to the high resolution needed for the energy measurement and the inherent high bandwidth of the channel trigger module, it is extremely difficult to design a mixed (simultaneously functioning digital and analogue parts) germanium channel in the dimensions currently allocated for the electronics.

In order to understand the limitations in principle of this method, the calculated, noise-free event current pulses were processed according to this simplified, nevertheless using an amplitude resolution that is only restricted by numerical

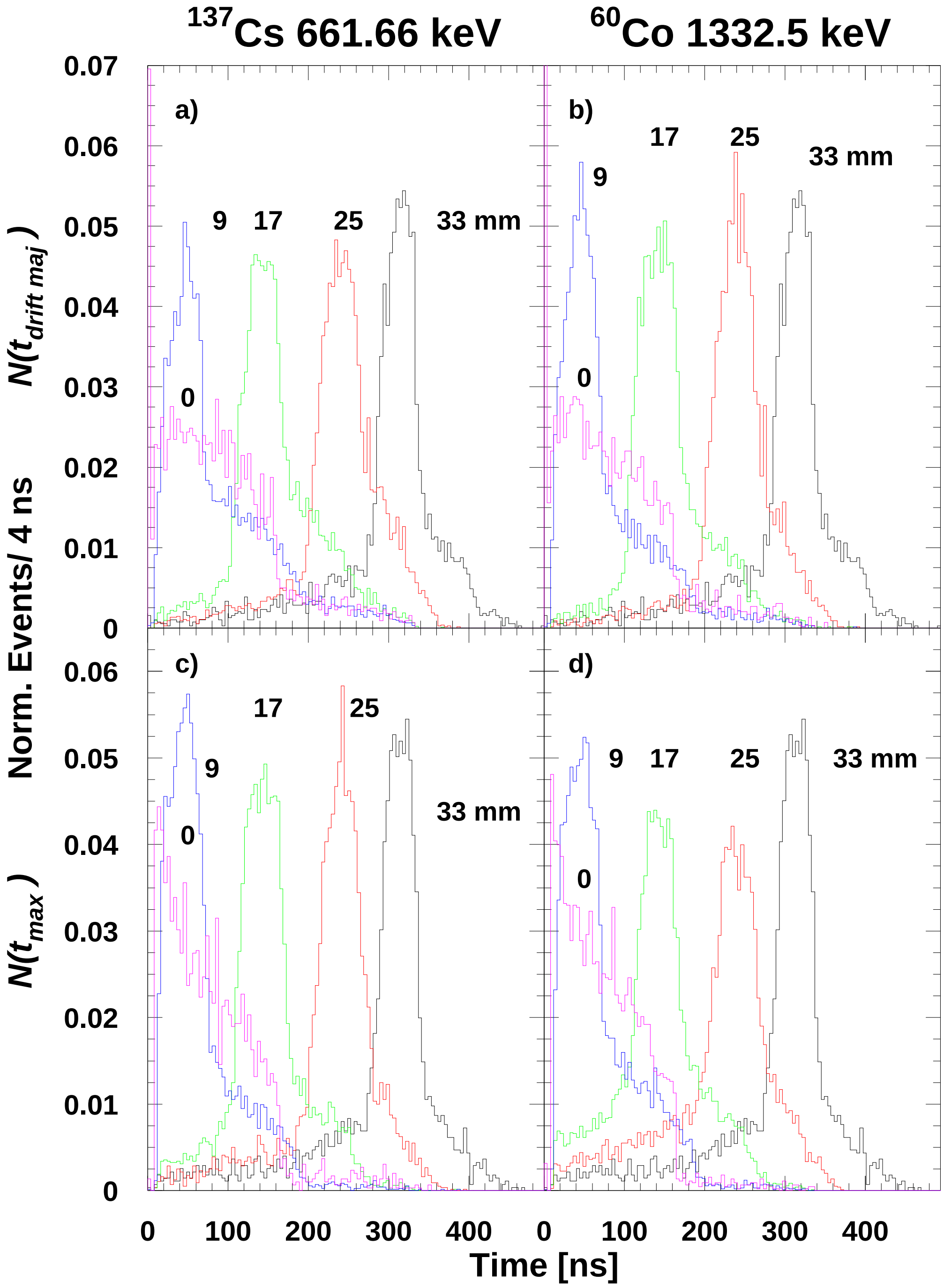

Figure 4.1: Calculated event distributions of majority carrier drift times $N(t_{\mathrm{drift}_{maj}})$ for the main interaction (a,b) and of the time-to-maximum $N(t_{\max})$ (c,d) at the shown energies and irradiation radii.

rounding errors and therefore is close to ideal, time-to-maximum algorithm and the results are shown in Fig. 4.1 for 662 and 1333 keV. The distributions have been plotted with 4 ns bin width, which is the sampling period of the ADC employed in the measurements reported in chapter 6. The distributions closely follow those of the drift time for electrons with a slight increase in the number of events assigned to shorter drift times and thus to radii smaller than the entry position. Note that there is little difference between the distributions corresponding to $r = 0$ and 9 mm, as expected from the position dependence of the drift time of majority carriers (see section 3.2.4).

4.1.3 The method by Eschenauer

A paper from the nuclear physics group at the University of Cologne [Esc94] presents a method for correcting trapping losses in HPGe detectors by determining the entry radius of the γ-ray. The method is explained as based on the time taken by the charge pulse to reach a given fraction of its final amplitude (see Fig. 4.2), but the block diagram of the experimental set-up (Fig. 2 in [Esc94]) shows that a differentiated charge pulse, i.e. a current pulse, was used as input at the Constant Fraction of amplitude Discriminators (CFDs).

It is pointed out in the paper that the fraction and delay used for measuring the radius are dependent on the particular detector and preamplifier used. Furthermore, the time-radius correlation must be recalibrated if the neutron damage, equivalent to the charge density due to the impurity concentration, varies during an experiment. Therefore, this method cannot be easily extended to multiple crystal arrays such as MINIBALL.

The method was tested with calculated, noise-free event current pulses (see Fig. 4.3), according to the explanation given in the article and using the fractions (20% and 50%, giving T_{20} and T_{50}; see Fig. 4.2) indicated in the block diagram

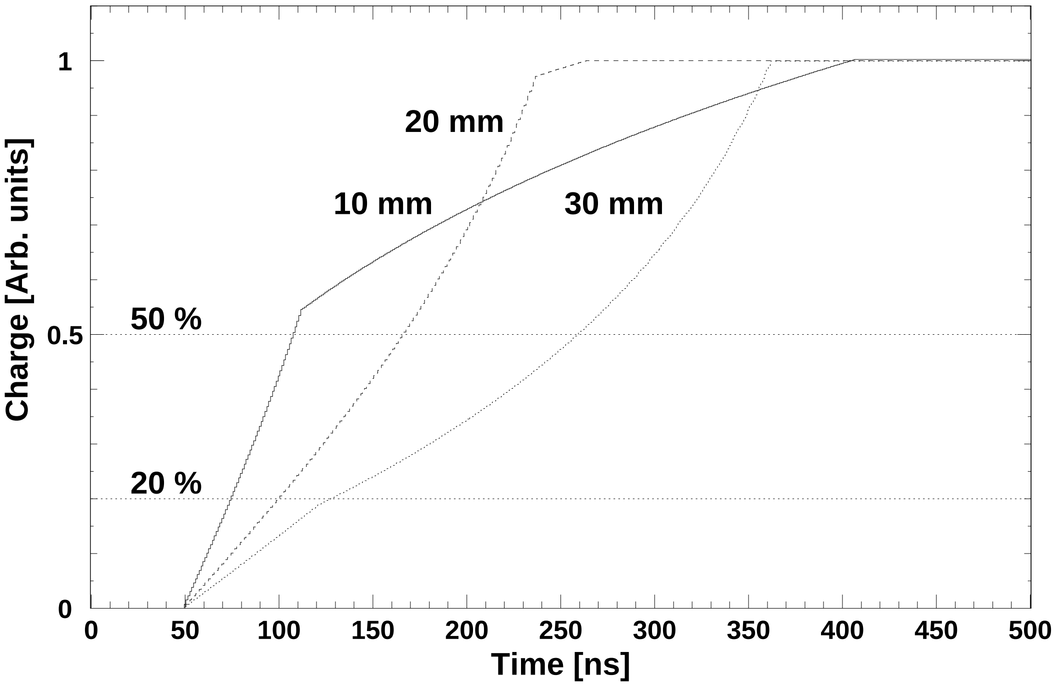

Figure 4.2: Normalised calculated charge pulses for single interaction events taking place at the indicated radii in the coaxial part of a CLUSTER module.

for the electronics employed. As the energy decreases, the overlap between distributions from neighbouring radii becomes larger and at 662 keV, nearly as many events (47 %) are assigned to other radii as to the collimator position at 33 mm. At 122 keV, the distributions for 26 and 33 mm become nearly indistinguishable as their median values are only separated by 4 ns. The radial resolution attainable with this method thus seems to be limited to higher energies, where determining the position of the main interaction also gives a very good measurement of the γ-ray entry point (see section 3.3). Furthermore, the validity of the method is strongly dependent on the exact values of the fractions. If a large difference is chosen between thresholds, for instance T_{30}–T_{90} as in section 4.1.4, the centroid of the distribution shifts to longer time differences as the irradiation radius is in-

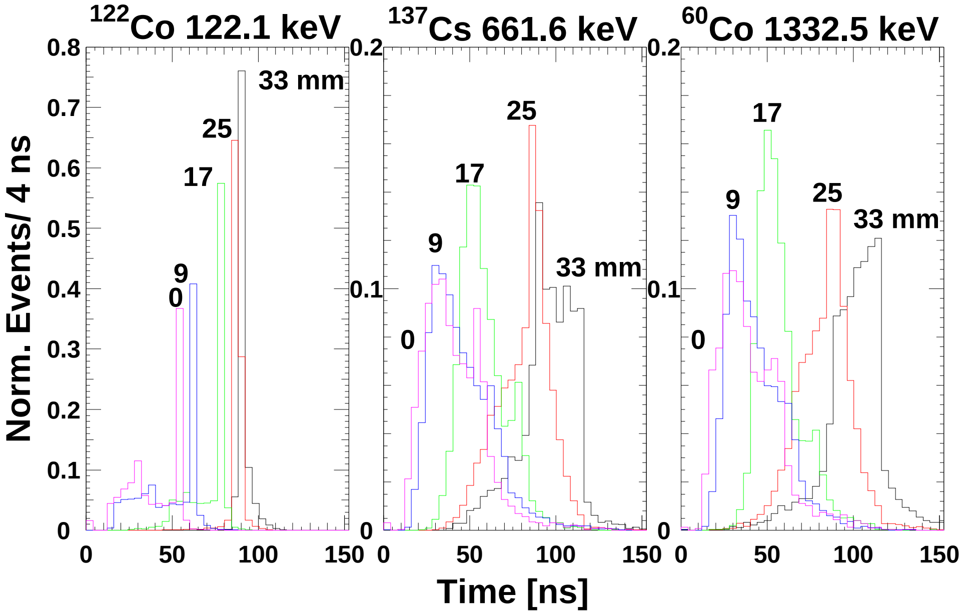

Figure 4.3: Calculated event distributions for the time difference $T_{50} - T_{20}$ at the shown energies and irradiation radii in mm.

creased, but then starts to shift towards shorter time differences for larger radii. A given time difference then corresponds to two possible irradiation radii and the method would yield little radial resolution when the whole frontal surface of the crystal is irradiated.

4.1.4 The T_{30}–T_{90} method

The paper by Kröll et al. [Krö96] describes a method for establishing the entry radius of a γ-ray by measuring the times at which the charge pulse reaches 30 % and 90 % of its final amplitude, with a time origin set at 10 % of the final amplitude (see Fig. 4.2). The system described used a digital oscilloscope to sample the charge pulses with 10 bit dynamic range, 100 MHz sampling frequency and an analogue bandwidth of 250 MHz. Energies up to 662 keV were measured and a radial resolution of between 4 and 8 mm achieved.

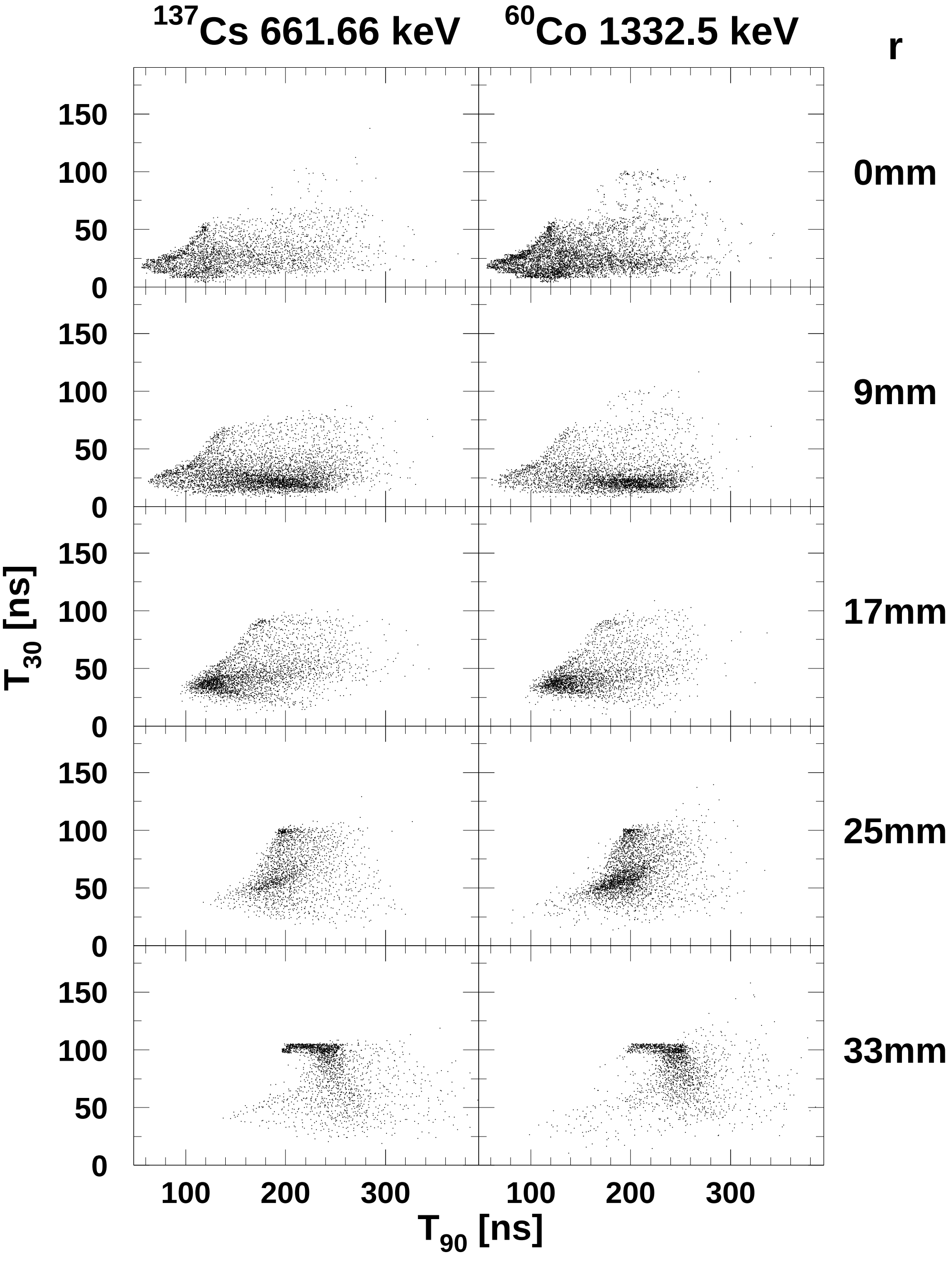

Figure 4.4: Calculated distributions of the T_{30} and T_{90} parameters at the shown energies and radii.

It is however not clear how this method could be implemented without using a fast ADC to sample the charge signals. Using CFDs to extract time points from CLUSTER module charge pulses requires delays of up to 400 ns, or the expected time difference between the final value of the pulse edge and the instant when the desired fraction is reached (see [Leo87]). The time resolution that can then be achieved seriously limits the radial resolution to considerably lower than the 10 ns from the system used in the paper. Even if the charge pulses are sampled, the dynamic range imposed by the energies requiring radial resolution would necessitate more than one ADC per detector. Moreover, the volume of data produced would need to be reduced on-line in order to avoid limiting the event throughput of the data acquisition system.

With sampled charge pulses, determining the time when a fraction of the final amplitude is exceeded requires a comparatively large number of samples. The three charge pulses shown in [Krö96], acquired for 1 μs, have a considerable level of ringing after the integration and the determination of the final value, and therefore of the fraction thresholds, requires additional processing of the pulses.

To a lesser extent, the same problem applies to the determination of the amplitude before the integration has begun. As the count rate increases, more and more events arrive before the preamplifier output has reached its DC value and an offset from the previous integration is the “baseline” for the new charge pulse. If the charge signal is sampled, each charge pulse can only cover a reduced fraction of the ADC dynamic range and a loss of resolution for the sampled amplitude is inevitable. A “baseline restorer” (see e.g. [Nic74]) must then be incorporated either in the analogue or digital domain in order to determine the real charge pulse amplitude and therefore the fractions.

A further problem of this method when used without a collimator is the distribution of the measured parameters. The distribution of the measured parameters $(\mathrm{T}_{30}, \mathrm{T}_{90})$ does vary in shape depending on the event energy, but this could be corrected since the event energy is always available. In an in-beam experiment, a given pair $(\mathrm{T}_{30}, \mathrm{T}_{90})$ has to be assigned to a corresponding entry radius, but in Fig. 4.4 many points are present in more than one irradiation radius, often for positions that cannot be due to a γ-ray let through unaffected by the collimator. The measured "rise-time" distribution for 662 keV and $r = 7$ mm (Fig. 3 in [Krö96]) has at least one common border with all other radii investigated (0, 15, 22 and 30 mm). A minimal noise amplitude on the signals would make one parameter cross a border and the event would be assigned to a radius far away from the real γ-entry radius.

4.2 The steepest slope method

A new method for measuring the entry radius of γ-rays employing the first derivative of the current pulse in order to determine the majority charge carrier drift time, even for multiple interaction events is proposed in this thesis (see section 2.3.1). The distribution of the steepest slope times t_{slope} where the difference function has its absolute minimum are shown in Fig. 4.5. No noise was superimposed to the calculated signals and no filtering was performed on the event current pulses. Furthermore, the amplitude resolution for the current pulses and the corresponding difference functions was only limited by numerical errors and is hence close to ideal. Under these ideal conditions, the agreement with the corresponding majority carrier drift time distributions is only slightly better than when using the time to maximum method. As expected, fewer events are assigned to interaction radii smaller than that of the main interaction. The corresponding measured distributions will be reported in chapter 6.

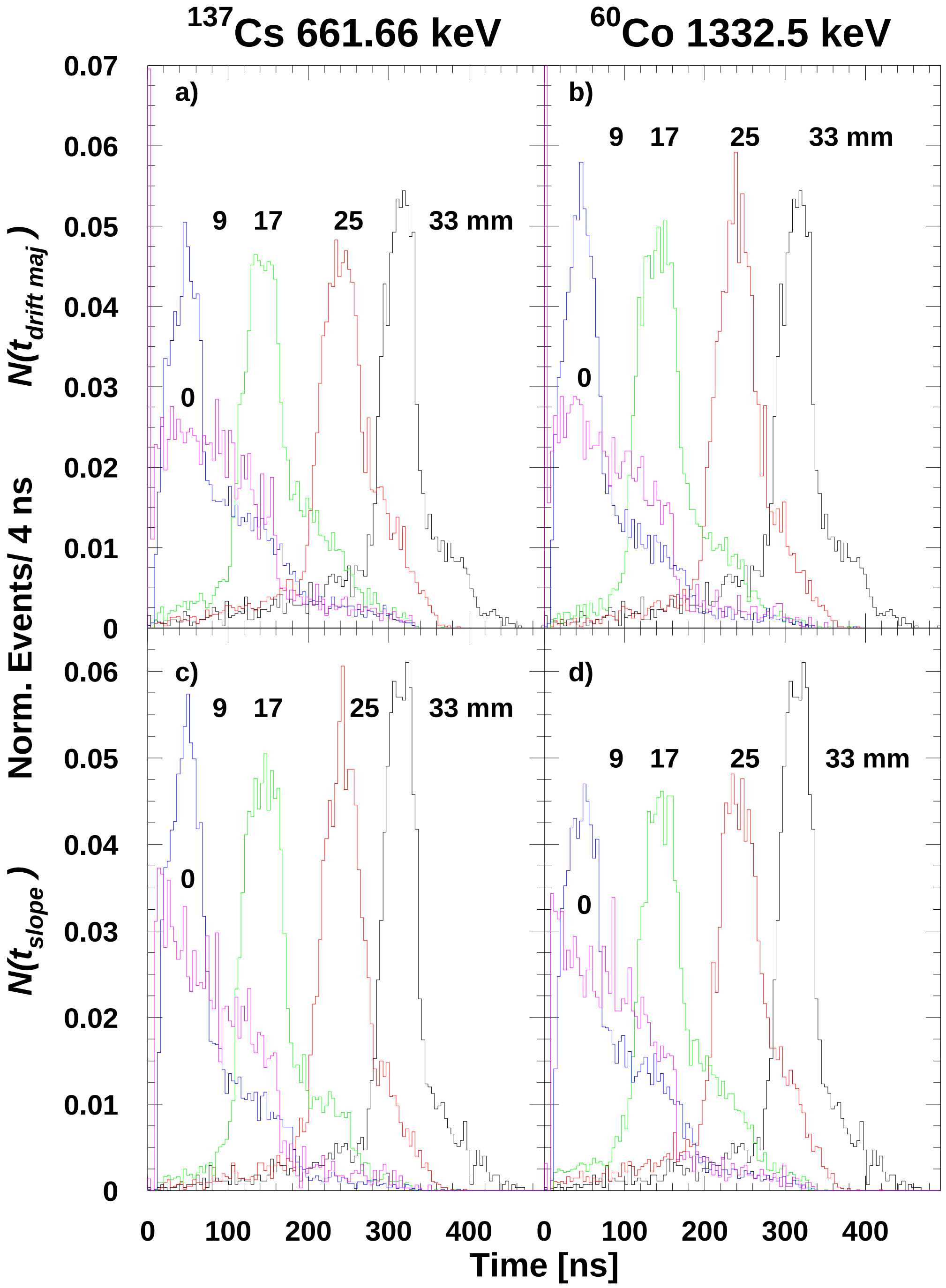

Figure 4.5: Calculated event distributions of majority carrier drift times $N(t_{\mathrm{drift}_{maj}})$ for the main interaction (a,b) and of the steepest slope times $N(t_{\mathrm{slope}})$ (c,d) parameter at the shown energies and irradiation radii.

Chapter 5

Preamplifiers for Ge Detectors

Chapters 2 and 3 have presented in detail the generation of an electric signal as a result of a γ-ray interaction in the detector. In chapter 4, the interaction data from the Monte Carlo simulation were used to establish a target for the position resolution that can be measured in a CLUSTER module with a collimator. Before reporting the measured performance of the methods considered for the determination of the entry radius of γ-rays, the different possibilities for amplifying the detector signal must be studied. The most important information in the detector signal is the γ-energy, which can be measured by integrating the event current pulse and measuring the final value, proportional to the liberated charge. This integration can be performed in the first electronic stage and a voltage waveform mirroring the detector current pulse reconstructed by differentiating the "energy" signal. Alternatively, the detector current pulse can be amplified or converted to a voltage waveform and then integrated.

A review of nuclear electronics beyond the possible scope of this chapter can be found in [Nic74] and to a smaller extent in [Leo87, Rad88]. The peculiarities of instrumentation electronics used with germanium detectors also need to be considered. Moreover, the different noise contributions present in a germanium channel must be studied in order to guarantee that the energy resolution is not degraded by the radial determination. The performance of the preamplifier designed in this project, which is described in detail in appendix A, is also reported in this chapter.

5.1 Electronics for Ge data acquisition

Germanium γ-ray spectroscopy detectors require instrumentation electronics tailored for their particular characteristics. A much more thorough review of germanium electronics than the length of this section allows can be found in [Sun92].

When a γ-ray interacts with a germanium counter, a current pulse is generated. In γ-ray spectroscopy, the basic information that must be extracted from the current pulse is the event energy. The energy deposited in the detector liberates a charge (see chapter 2), which can be measured by integrating the resulting current pulse. In most cases, this energy is then converted to a digital value and analysed using a computer. When using a detector array, or an instrument with several germanium detectors, the necessary analysis is nearly always so complicated that the computer carrying out the analysis is only able to accept new data for a small fraction of time. Furthermore, in-beam experiments run uninterruptedly for several days and it has proven fruitful to store the large volume of data (produced at rates between 4 and 40 MByte/s) for subsequent off-line analysis in order to extract the maximum possible information from the experiment data. Hence, the highest priority of the data acquisition system is to establish the fastest possible connection to the data storage units where the events are recorded. In order to monitor the experiment that produces the data, an on-line analysis is performed with a fraction of the events acquired.

The emission of radiation is a process whose distribution in time is characterised by Poisson statistics. Therefore, the signals produced by the detectors are randomly distributed in time. This random nature requires determining the instant in time when a valid event has taken place, a task performed by the experiment "trigger" module for the data acquisition system. The trigger signal is then used to control the Analogue to Digital Converters (ADCs) that measure the relevant event parameters: e.g. energies, delays between one detector and the trigger signal, delays between detector signals.

In order to achieve maximum event throughput, channels employing digital signal processing to perform the measurements sample the relevant signals continuously and the trigger pulse is used to stop the sampling. The sampled signals are then processed and the event data gathered. Despite the continuous advances in digital electronics, better results are still today produced by performing this triggering in the analogue domain as a result of the detector signals short duration and their random distribution in time. Furthermore, the combination of dynamic range, high resolution and data throughput complicates the transfer of this electronic instrumentation application into the digital domain. The advantages of the signal processing traditionally employed in nuclear electronics become evident in [Sch91], where a similar technique was used to implement an 8 GHz ADC system.

Due to the statistical nature of radiation arrival at a detector, the time difference between signals can be very short and a second signal can sometimes overlap with that of the first event, presenting an amplitude at the input of the ADC that does not correspond with either of the events. So-called pile-up can be detected by monitoring if a second detector trigger has been produced before the ADC starts its conversion and pile-up events rejected. Obviously, the duration of the signals has to be chosen, whenever possible, to provide minimum pile-up at the expected count rate. After the arrival of an event, the electronic channel

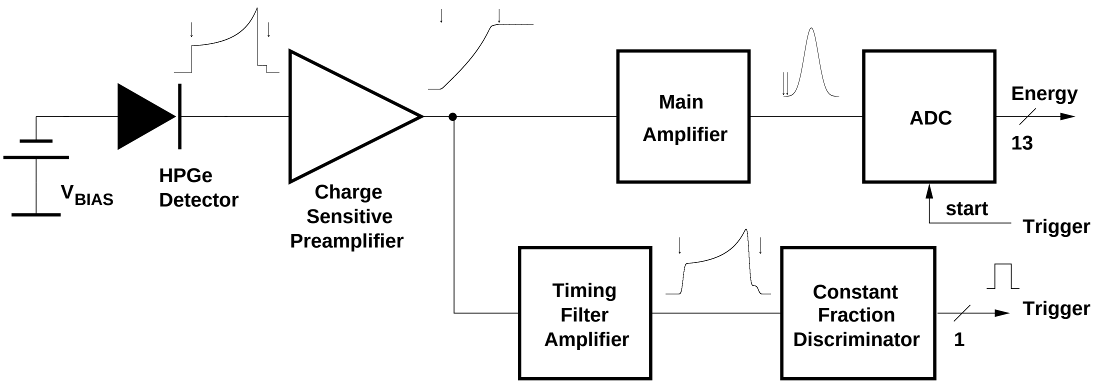

Figure 5.1: Block diagram of a germanium channel. A time difference of 250 ns has been indicated on the analogue waveforms.

becomes unavailable for new signals during a certain time, the so-called dead time, which is the main limitation for the data throughput that can be achieved. In order to acquire the maximum number of events, the dead time should be kept short, meaning that each event must be processed as quickly as possible while maintaining the desired high resolution.

For germanium detectors, the signal is generated in $\lesssim 0.5$ μs, much shorter than the typical time needed by electronic circuits to deliver a precise measurement of the liberated charge. Present performance requires a total processing time of about 10 μs, when 4 μs conversion time ADCs are used. The resolution of large volume HPGe detectors is typically 2.5 keV at 1332.502 keV, or 0.15 %, so the voltages and currents have to settle to this precision in less than 6 μs. Furthermore, the width of one Least Significant Bit (LSB), the ADC channel width in nuclear spectroscopy terms, has to remain constant over the whole energy range, typically 13 or 14 bits. The differential non-linearity of the complete electronic channel that can therefore be deemed acceptable is typically below 0.1 %.

The block diagram for a typical germanium detector channel is presented in Fig. 5.1. The current pulse from the detector is integrated in the charge sensitive preamplifier, producing a voltage proportional to the collected charge and thus to the detected energy. The two branches after the preamplifier serve two purposes: the acquisition of the voltage carrying the energy information and the extraction of a time origin. The time origin is necessary as a result of the random distribution in time of events. It can be determined by comparing the preamplifier output with a fixed voltage, the so-called leading edge method, or by a less energy dependent Constant Fraction Discriminator (CFD) [Nic74]. This time origin signal is also used in multi-detector set-ups to measure the time relationship between the different detector signals. The timing filter amplifier employed before the CFD performs a differentiation of the charge signal in order to recover the radius independent, sharp initial edge of the current pulses.

The energy information contained in the maximum amplitude of the charge pulse is filtered at the so-called main amplifier. This amplifier produces an output pulse for each integration in the preamplifier and the resulting maximum is proportional to the energy deposited in the detector. Note that the output of the main amplifier reaches its maximum after a few microseconds compared to the 250 ns duration of the detector pulse. The ADC is designed to convert the maximum amplitude of its input pulse into a digital word and the distribution of measured values corresponds to the energy spectrum (see Fig. 5.8). The CFD output can be used for measuring the time when the detector has generated its signal, relative to a reference or to another detector.

Including the radial information required the addition of a third branch to those in the block diagram presented. The greatest flexibility for current pulse processing is obtained by using a fast ADC to sample the current pulses and processing them in the digital domain. In order to avoid introducing a time delay for the data acquisition system, the on-line processing time is limited to 10 μs, which indicates that an analogue implementation of the processing method chosen is today the faster alternative if the radial information is to be produced synchronously with the energy measurement. Since at least 25 samples are needed per pulse, sampling the current pulses and storing them on tape results in a data volume that seriously compromises the event throughput of the data acquisition system and thus the dead time of the instrument.

5.2 The amplification of Ge signals

The two methods presented in chapter 2 for determining the entry radius of a γ-ray in a germanium crystal use the original current pulse generated as a result of the interaction. Traditionally, only the event energy is measured and the necessary integration is performed in the first electronic stage, the preamplifier. If the current pulse is needed for pulse shape analysis, it can be first amplified and then integrated, or recovered after an initial integration. In the latter case, any further filtering performed on the charge signal would compromise the quality of the current waveform that can be eventually reconstructed. The preamplifier described in appendix A integrates the detector current pulse in the cryostat and this charge signal is immediately differentiated. It should be noted that the detector current pulse is converted to a voltage waveform in both alternatives.

This section will present the different alternatives for Ge-detector preamplifiers and the reasons for the design produced. Before evaluating different circuit possibilities that can be used for germanium preamplifiers, the general considerations regarding the signal source and all circuit configurations will be reviewed.

5.2.1 General considerations

The signal generator

Considered as a signal generator, a germanium detector is a pulsed current source. As a reverse biased diode, its output impedance is very high, making it a nearly ideal current generator. The magnitude of the current delivered is comparatively small, so that some sort of amplification is needed. This amplification is best carried out either by employing a transresistance amplifier or by using an active integrator. Both approaches employ an operational amplifier and any current that does not flow into the feedback network does not contribute to the production of the output signal. Hence, the input impedance of the operational amplifier should be as high as possible.

Stability of the electronic parameters

The basic information that has to be measured from the current pulse generated as a result of a γ-ray interaction is the energy deposited in the counter. The integration that measures the charge set free in an event must be very stable in order to achieve the desired energy resolution. Any gain drifts between calibrations will broaden the peaks in the energy spectrum and will result in a decrease in resolution with increasing measuring time as they will be indistinguishable from poor energy resolution. Once temperature effects are removed, typical systems present shifts in gain lower than 1 LSB, corresponding to $\simeq 0.3$ keV, over a period of two weeks. In traditional germanium electronics, this level of stability is mainly due to the constant environment provided by the detector cryostat, where the high quality integrating capacitor is placed. The temperature is thus kept almost constant and the high vacuum necessary for maintaining the low temperature further prevents variations in the integrating gain. The high vacuum, however, requires very careful selection of the components that are placed in the cryostat, since outgassing is unavoidable and the pumping power available is limited. If the γ-energy is measured by a different method, this same level of stability must be maintained.

Noise figure of merit

Contrary to common practice in electronic engineering, the noise performance of nuclear electronics systems is hardly ever quoted as the equivalent input noise spectral densities. The information measured is the charge liberated by a γ-ray. Therefore, the relevant parameter for studying noise contributions in a given channel is the Equivalent Noise Charge (ENC), defined as the charge that would generate a signal equal in amplitude to the noise present in the channel. As opposed to the equivalent noise generators or the Signal to Noise Ratio (SNR), the equivalent noise charge is a figure of merit independent of the detected energy. Care must be taken when comparing the noise performance between different systems in order to maintain comparable bandwidth, i.e. shaping time constants. Furthermore, as a result of the reference being an energy spectrum, the resolution is usually specified as the Full Width at Half Maximum (FWHM), instead of the variance σ. For a Gaussian distribution, FWHM $= 2\sqrt{2\ln 2}\,\sigma = 2.355\,\sigma$. For an energy E that liberates a charge Q and results in a signal of amplitude V at a circuit node where V_n is the noise amplitude, it follows that

$$\frac{\mathrm{ENC}}{Q} = \frac{V_n}{V} = \frac{E_{fwhm}}{2.355\,E}\ , \tag{5.1}$$

where E_{fwhm} is the full width at half maximum of the peak at energy E. The resolution can be directly calculated from the ENC as

$$E_{fwhm} = 2.355\ E_{\mathrm{pair}}\ \frac{\mathrm{ENC}}{|e|}\ , \tag{5.2}$$

which explains the common practice of quoting ENC in keV. For germanium, $E_{\mathrm{pair}} = 2.9$ eV, leading to

$$E_{fwhm}\ (\mathrm{eV}) = 4.27 \cdot k_{\mathrm{gain}} \cdot V_n\ (\mathrm{V}), \tag{5.3}$$

whose proportionality constant, k_{gain}, can be removed by injecting a calibrated charge at the preamplifier input and adjusting the gain of the channel to produce the amplitude corresponding to the injected charge.

Bandwidth

Due to the pulsed nature of the signals, the channel bandwidth must be high. Furthermore, the requirement to treat each event independently from all preceding and subsequent ones further increases the bandwidth specification. The position information can be extracted from the detector current pulses by analysing their structure, further increasing the bandwidth specification for the "current" waveforms. The high resolution needed for the charge signal means that the bandwidth at this output should be kept as low as possible. The ADC used to digitise the current waveforms has a 250 MHz sampling frequency, so that a tentative target for the pulse bandwidth was set in the region of 100 MHz.

A common apparent misconception about the concept of bandwidth should be clarified here. The -3 dB frequency of an amplifier is usually interpreted as the highest frequency that can be studied at its output and frequencies above it are considered irrecoverably lost. However, provided the frequency response of the amplifier is time-invariant and therefore remains the same for all pulses, the attenuation effected above $f_{-3\mathrm{dB}}$ can be corrected up to frequencies where the signal and noise amplitudes become comparable. If the current pulse is integrated and then differentiated, the bandwidth of the reconstructed current signals is not directly limited by the $f_{-3\mathrm{dB}}$ of the integrator.

Filtering

Contrary to common established practice in almost all other areas of electronic engineering, filters employed in nuclear electronics are usually specified in the time domain. For instance, a first-order, low-pass RC filter is always referred to as an integrator of time constant $\tau = \mathrm{RC}$. The time taken by the main amplifier output to reach the energy proportional value is normally called the peaking time t_p and in the case of Gaussian shaping is related to the shaping time by $t_p = 2.2\ t_{sh}$, where t_{sh} is the dominant integration time constant for the germanium channel.

5.2.2 Current sensitive preamplifiers

The original current pulse can be amplified with a current preamplifier, but better results are obtained if the current is converted to a voltage waveform, which requires a transresistance amplifier like that shown in Fig. 5.2. This is the most common solution adopted for photodiodes and a very thorough review of this kind of amplifier can be found in [Gra96]. Straightforward reasoning would imply that since the detector delivers a current pulse and the radial resolution is best extracted from this pulse, this current should be amplified or alternatively converted to a voltage pulse. This approach would perform the required current to voltage conversion, but the stability of the integration then needed in order to measure the energy deposited in the detector would be compromised. Furthermore, electronically integrating a current is much more accurate than integrating a voltage. The correction to the measured energy would not be limited by the radial resolution but by the energy resolution, restricting the application of such a preamplifier only to experiments presenting noticeable Doppler peak broadening.

A further objection to this approach is the impedance presented to the detector. As first pointed out in [Rad74], the input impedance Z_{in} of a transimpedance amplifier (Fig. 5.2) is

$$Z_{in} = \frac{Z_f}{1 + A_{ol}} \ , \tag{5.4}$$

where Z_f is the generalised feedback impedance and A_{ol} is the open loop voltage gain of the operational amplifier. For most of the frequency range, the operational amplifier open loop gain can be described by a single pole and the input

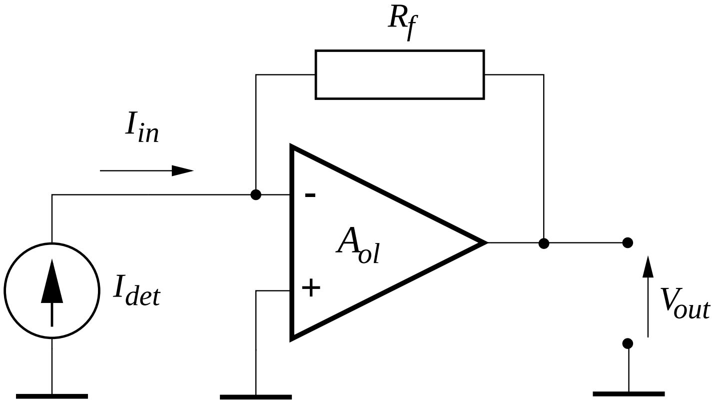

Figure 5.2: Schematic circuit of a transresistance amplifier where $V_{out} = I_{det} \cdot R_f$.

impedance becomes

$$Z_{in}(j\omega) = \frac{Z_f(j\omega)}{1 - \frac{\omega_1}{j\omega}} , \tag{5.5}$$

where ω_1 is the frequency at which $|A_{ol}| = 1$. For $\omega \ll \omega_1$, the input impedance can be rewritten as

$$Z_{in}(j\omega) = -j\omega \cdot \frac{Z_f(j\omega)}{\omega_1} . \tag{5.6}$$

A transresistance amplifier providing a current to voltage conversion accordingly presents an inductive input impedance, far from optimal for a current generator.

Implementations in the literature

In order to achieve large current to voltage gains, the value of the feedback resistor should be large. Any parasitic capacitance between the output and input connections of the operation amplifier then combines with this high value resistor to form an RC feedback network, in practice integrating the short pulses delivered by the current source when a γ-ray is detected.

All current sensitive preamplifiers for semiconductor detectors found in the literature either differentiate the integrated input current pulse [Mil67, Mil72, Gou94] or amplify the voltage at the input terminal of the operational amplifier [Gat75, Gat78]. In all cases except [Gou94], the published noise performance at the energy output lies below that obtainable with a traditional charge sensitive preamplifier for coaxial germanium detectors. Furthermore, the other designs employing differentiators use several integrating stages, each followed by a passive differentiator. The component values in the integrating and differentiating networks must be accurately matched in order to achieve a reasonably clean transfer function and thus retain the radial information in the pulses.

As a result, a single stage active differentiator was designed and tested with a commercial germanium preamplifier for reconstructing the detector current pulses. This differentiator was then incorporated immediately after a newly designed charge sensitive amplifier (see appendix A) and used to perform the measurements reported in chapter 6.

5.2.3 Charge sensitive preamplifiers

Before presenting the performance of the preamplifier designed as part of this project, the general specification that an active integrator used for producing the charge signal must fulfill will be presented. A charge sensitive preamplifier, as depicted in Fig. 5.4, integrates the input current pulse, producing a voltage output proportional to the charge that has previously drifted in the detector. When the current source is pulsed, the output of the preamplifier rises for the duration of the pulse and decays exponentially with time constant $\tau = R_f C_f$ between pulses. In order to keep the noise contribution small (see subsection 5.2.4), R_f has to be large, typically 1 or 2 GΩ for germanium detectors. Resistors of such high values are far from ideal and switched integrators were therefore investigated long ago [Gou69, Rad70]. Depending on the method employed to remove charge from the integrating capacitor, charge sensitive preamplifiers are usually divided into: optical, transistor or resistor reset. The switch needed to remove the accumulated charge must be placed directly at the input terminal of the operational amplifier where any parasitic capacitance reduces the SNR. The advantages of switched integrators are however limited to low energies and “reset” preamplifiers have not replaced the traditional resistor feedback configuration for in-beam γ-ray experiments.

In order to investigate the importance of these non-idealities, an Impedance/Gain-Phase analyser (Hewlett Packard 4194A) was used to measure the frequency dependence of several feedback networks provided by EURISYS. The feedback components were mounted on Printed Circuit Boards (PCBs) as used with CLUSTER modules, and had nominal values of 1 GΩ in parallel with 0.5 pF, typical of those used with large volume germanium detectors. One of the measured impedances is shown in Fig. 5.3. In the frequency range studied, between 100 Hz and 40 MHz, this network was approximated as the parallel combination of a 929.845 MΩ and 1.84935 pF. The excess stray capacitance ($\simeq$ 1.3 pF) cannot be unambiguously attributed to the resistor, as the PCB was not mounted on top of a ground plane, as is the case in the capsule. The frequency characteristic of the impedance presents nearly ideal behaviour above 600 Hz with constant 90° phase lag. As a result of these measurements, it was decided to rely on the components provided by EURISYS for the “cold” circuit board.

In resistor feedback preamplifiers, R_f also sets the DC voltage at the input of the preamplifier. A side effect of the high values used for this resistor is that the input voltage cannot be directly measured. Any voltage measuring instrument has an input impedance considerably lower than the other impedances at that circuit node, modifying the operating point of the input stage. When no current flows through the detector, there is no voltage drop across R_f and the input voltage is the voltage at the preamplifier output. Any DC voltage drop resulting when the preamplifier is directly connected to the low voltage terminal of the detector, exploiting the virtual ground at its input, must be due to the detector leakage current and can therefore be used to measure this very small current

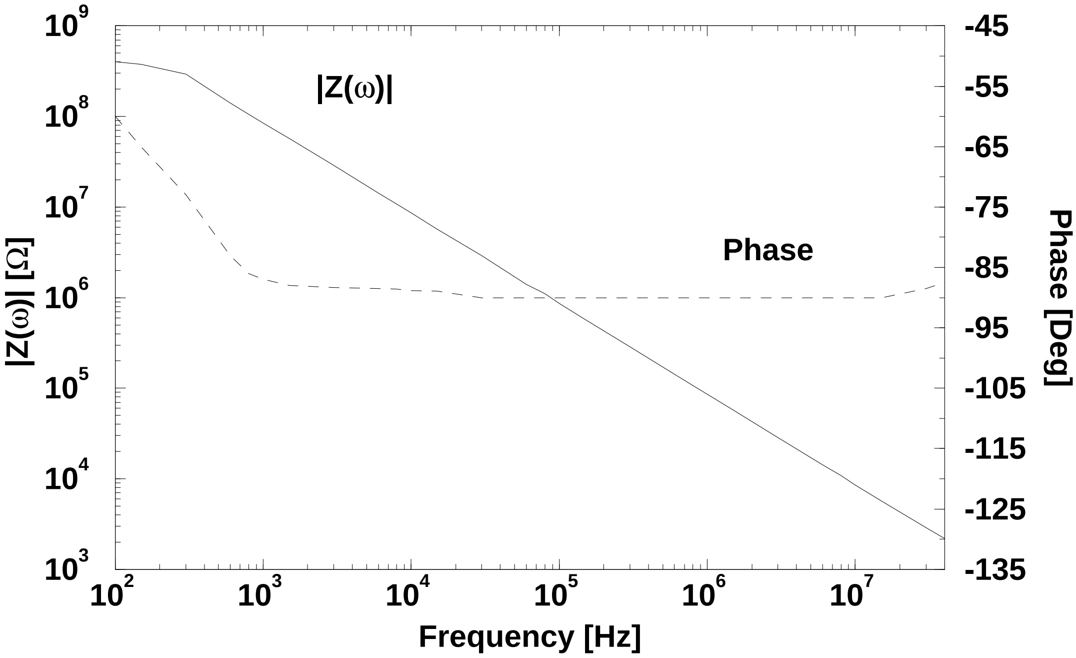

Figure 5.3: Measured frequency dependence of the feedback impedance magnitude (solid line) and phase (dashed) for nominal values of 1GΩ in parallel with 0.5 pF.

($\lesssim$ 100 pA)

Specification of the operational amplifier

Germanium preamplifiers still today use operational amplifiers made from discrete transistors in order to better handle the peculiarities of the signals and achieve the best resolution possible. The fact that the detector has to be operated at around 100 K presents the possibility of cooling the components critical for noise performance to cryogenic temperatures and results in a physically long connection between the input transistor and the following stage. The low temperature components have to be selected for operation under the high vacuum necessary for maintaining the low detector temperature. Outgassing prevents the use of components in porous packagings, for which the package has to be "pumped empty" before cooling the cryostat in order to avoid establishing a

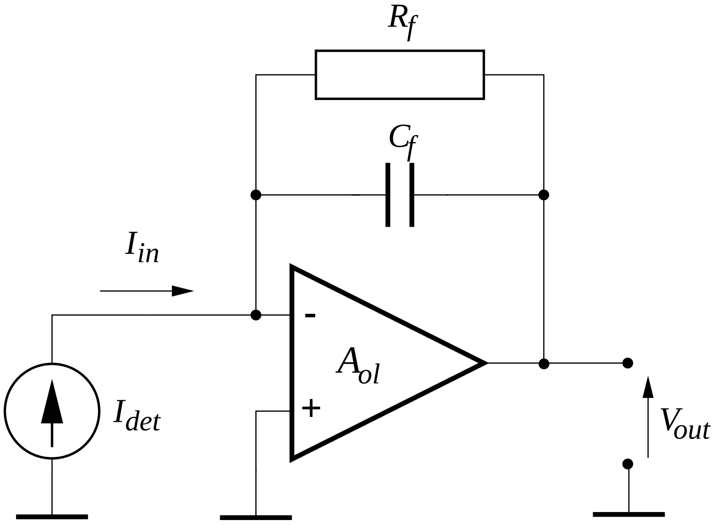

Figure 5.4: Schematic circuit for a charge sensitive amplifier

thermal conduction path to the cryostat walls.

Even though Fig. 5.4 has been drawn using the general symbol for an operational amplifier, the input signal is a current and this application does not require a differential input operational amplifier. Hence, the input stage need not be a differential amplifier, as is usual in most other operational amplifiers.

As is also obvious from Fig. 5.4, any current not flowing into the integrating capacitor will not contribute to the generation of the output voltage and thus reduce the SNR. As far as the operational amplifier is concerned, this translates to the lowest possible bias input current specification, pointing towards an input stage using a Field Effect Transistor (FET). Furthermore, the leakage current flowing through the detector produces a voltage drop in R_f, shifting the DC level at the preamplifier output from that observed without a detector. With $R_f = 1$ GΩ, each 100 pA of leakage current, typical for large volume HPGe detectors, results in a 100 mV level shift at the output of the integrating loop.

The highest input impedance configuration using a FET is the common source circuit. In order to achieve good noise performance, the input stage should also have high gain, commonly leading to the use of a FET-bipolar cascode as the input stage in order to obtain large gain over a reasonable frequency range. There are nevertheless commercial preamplifiers using different input stage configurations, although the timing resolution that can then be achieved is accordingly inferior.

5.2.4 Noise analysis of charge sensitive preamplifiers

The input FET

The FET is the main contribution to preamplifier noise and is, whenever possible, placed in the detector cryostat in order to have a low operating temperature and the shortest possible connection to the detector. Silicon Junction FETs are selected as the input transistors for the following reasons:

- Silicon JFETs have the lowest low frequency noise of all FET devices.
- JFET white noise can be accurately described using the small-signal transconductance g_m.
- Their noise spectral density is affected by the absorbed radiation dose to a lesser extent than other transistor types.
- They can operate at cryogenic temperatures.

The best results up to now have been achieved by diffusing the gate, source and drain regions into an epitaxial channel. The equivalent input noise spectral density shows a minimum between 100 and 150 K and follows the calculated spectral density considering only thermal sources above 120 K [Re95]. These temperatures correspond to the thermal equilibrium that the FET reaches in the cryostat. The cold finger responsible for cooling the germanium crystal also cools the FET through the electric conductors and a stable temperature is reached.

This FET operates at a higher temperature than the crystal, since the dissipated power ($\simeq$ 50 mW) heats up the transistor.

The equivalent noise current and voltage spectral densities at the gate of the JFET are commonly quoted as

$$\begin{aligned} \overline{S_{i_n}(f)} &= \frac{\omega^2 C_{\text{int}}^2}{g_m} kT + 2|e|I_g \\ \overline{S_{v_n}(f)} &= 4kT\frac{2}{3}\frac{1}{g_m} + \frac{A_f}{f} \ , \end{aligned} \tag{5.7}$$

where C_{int} is the internal input capacitance and can be approximated to $0.75 \cdot C_{GS}$ [Net81] with C_{GS} the gate-source capacitance, I_g is the gate leakage current, k is Boltzmann's constant and T is the transistor operating absolute temperature. The contribution from gate leakage current, or the input bias current of the operational amplifier, can be neglected as a result of the selection of FET types and cryogenic operation. From eq. 5.7, an equivalent noise resistance for the FET can be defined as

$$R_{n_{eq}} = \frac{2}{3}\frac{1}{g_m} \ , \tag{5.8}$$

and considered the sole noise contribution above the noise corner frequency. Thorough analysis of preamplifiers for radiation detectors [Man95] has shown that the spectral density of the equivalent noise at the gate of a JFET operated at constant current density can be described in terms of the intrinsic parameters for channel thermal noise Γ, for $1/f$ noise $H_{f^{-1}}$, and for Lorentzian noise H_L as

$$\overline{S_{v_n}(f)} = \frac{1}{C_i}\left[2kT \cdot \frac{\Gamma}{\omega_T} + \frac{H_{f^{-1}}}{f} + \frac{H_L}{f^2}\right] \ , \tag{5.9}$$

where C_i is the total input capacitance of the transistor and $\omega_T = g_m/C_i$ is the transition frequency. In transistors from the same process and operating at equal current densities, the spectral noise density increases with the input capacitance, as expected from experience. For the low noise processes studied, the values for the intrinsic noise parameters were found to be typically: $H_{f^{-1}} \simeq 5 \times 10^{-28}$ Joule,

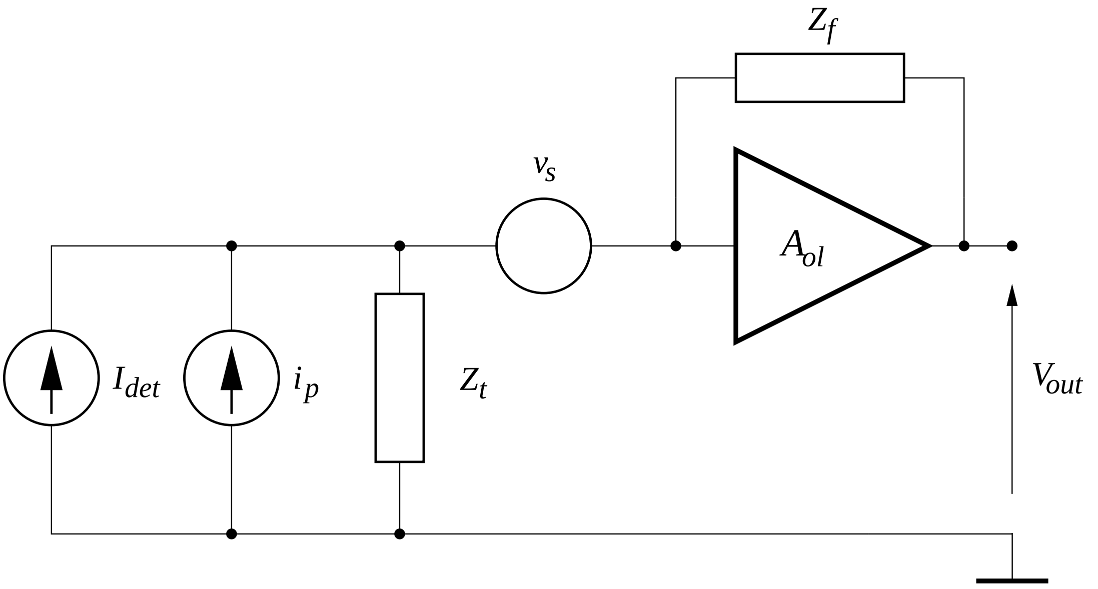

Figure 5.5: Equivalent noise circuit of detector and preamplifier.

$H_L \simeq 3 \times 10^{-28}$ Watt, $\Gamma = 4/3$ and $\omega_T \simeq 2 \times 10^9$ rad/s. The noise behaviour thus largely follows

$$\overline{S_{v_n}(f)} = 4kT\frac{2}{3}\frac{1}{g_m} , \tag{5.10}$$

except at low frequencies, where the two additional terms cannot be neglected.

Matching the detector and FET capacitances

Fig. 5.5 shows the noise equivalent circuit of a charge sensitive preamplifer, where Z_t represents the impedance at the input due to the detector load, the detector capacitance, the amplifier input capacitance and any stray capacitances. This equivalent circuit can be transformed into that of Fig. 5.6 with $Z_{in} = 1/C_f\omega_1$ (eq. 5.6) for the frequency range of interest. The signal is developed across the total capacitance presented to the detector despite the resistive input impedance of the charge sensitive preamplifier, so that the signal spectral density $\overline{S_s(f)}$ will be proportional to $1/{C_t}^2$, where C_t is the total capacitance at the input circuit node. For the signal to noise ratio,

$$\mathrm{SNR}^2 = \frac{(\mathrm{Signal})^2}{\overline{S_{v_n}(f)}} \propto \frac{C_i}{(C_{\mathrm{Detector}} + C_i)^2} \, , \tag{5.11}$$

which has a maximum when $C_i = C_{\mathrm{Detector}}$. As a result of this dependence, the input FET in charge sensitive preamplifiers for radiation detectors are selected to match the detector capacitance in order to obtain the best resolution possible.

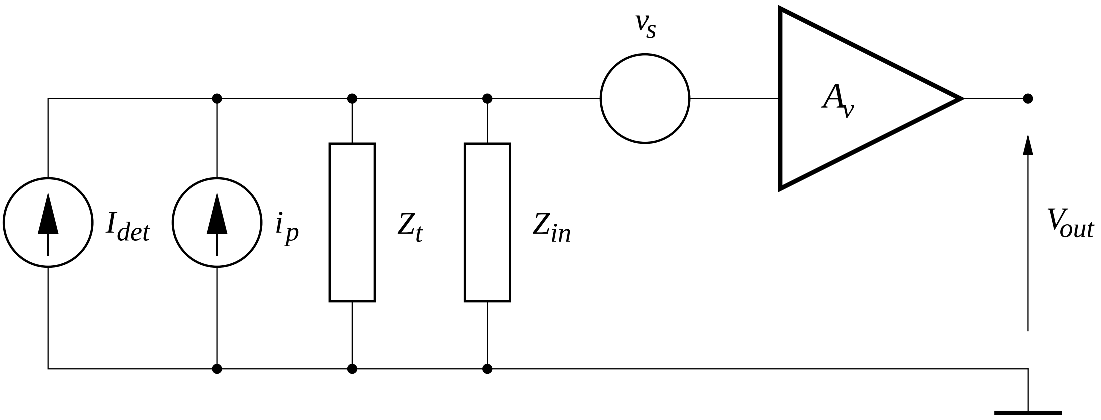

Figure 5.6: Equivalent noise circuit of a charge sensitive preamplifier.

The feedback network

A further contribution to the noise spectral density is due to the feedback network and in the case of a resistor in parallel with a capacitor ($R_f \parallel C_f$), it is

$$\overline{S_f(\omega)} = \frac{4kT}{R_f} \frac{1}{\omega^2 C_t^2} + 4kT \left(1 + \frac{C_f}{C_t}\right) \tan\delta \, , \tag{5.12}$$

where $\tan\delta$ is the loss factor of the capacitors. From the first term, the feedback resistor has to be as large as possible in order to limit its noise contribution but in practice the non-idealities associated with high valued resistors limit the feedback resistor to below a few gigaohm. The second term, accounting for dielectric losses in the capacitors, can be reduced by selecting a low loss feedback capacitor.

Coupling the detector to the preamplifier

When the preamplifier input is not used as a virtual ground for the high voltage supply (DC coupled detector), there are two possibilities for coupling the detector signal to the preamplifier (Fig. 5.7). The coupling capacitor reduces the input signal, as it forms a charge divider with the detector capacitance and should hence be at least an order of magnitude larger than C_{Detector}. If the preamplifier is connected as in Fig. 5.7(a), the value of the resistor must be high in order to keep its current noise contribution low. In Fig. 5.7(b), the value of C_{coupl} is limited by the available values for the biasing voltage employed. The high voltage across C_{coupl} also introduces excess noise into the channel. For the CLUSTER modules, the connection in Fig. 5.7(b) has to be employed as a result of having the capsules and outer contacts at ground potential. For the segmented modules, C_{coupl} has preliminarily been set to 560 pF/10 kV. The energy resolution of the EUROBALL CLUSTER modules was nevertheless only worse by less than 0.3 keV than could have been achieved by DC coupling the preamplifers if it had been possible.

Equivalent Noise Charge Calculation

As the signal is integrated for a finite duration in order to produce the amplitude that is measured, a whole formalism has been developed for analysing noise contributions in the time domain, using the so-called residual functions in place of the filter transfer function and delta and step noise in place of current and voltage noise, respectively [Gou72], also referred to as weighting functions and parallel and series noise contributions [Rad88].

In general, the spectral density of the equivalent noise at the preamplifer input can be described by

$$\overline{S_n(\omega)} = a^2 + \frac{b^2}{\omega} + \frac{c^2}{\omega^2}\ . \tag{5.13}$$

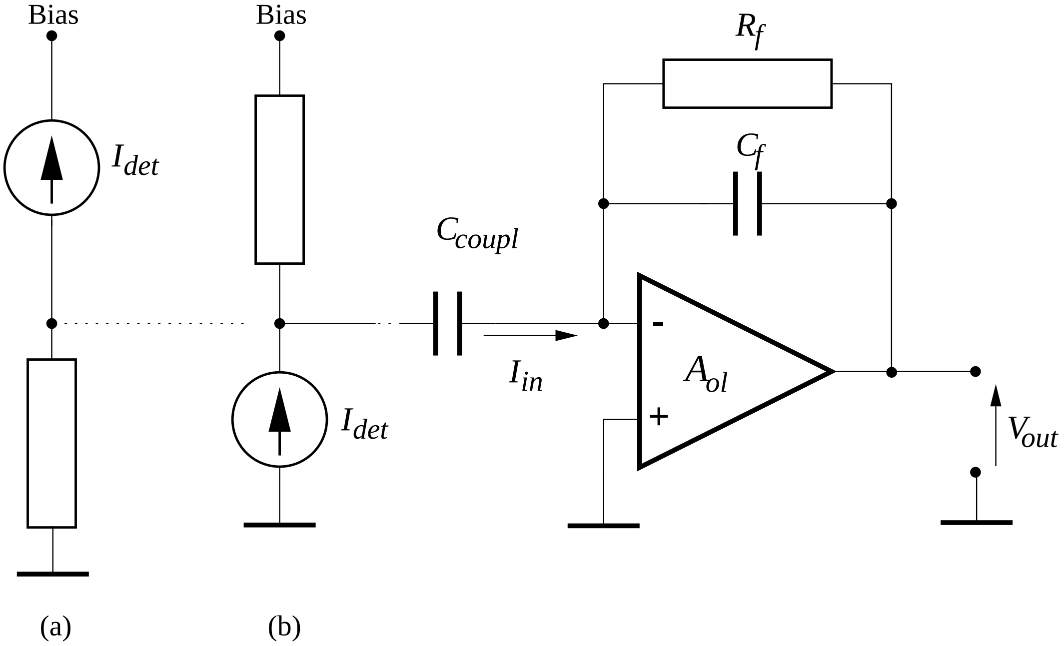

Figure 5.7: Possible connections for AC coupling the detector to a charge sensitive preamplifier.

Assuming that the detector current is integrated in a capacitor C_{gain} and that the preamplifier signals are ideally filtered, corresponding to the so-called cusp shaping, the Equivalent noise charge is

$$\mathrm{ENC}_{\infty} = C_{\text{gain}}\sqrt{2\pi ab} \ , \tag{5.14}$$

which is used as a normalisation factor for all other shaping filters, leading to

$$\mathrm{ENC}^2 = \mathrm{ENC}_{\infty}^2 \frac{F^2}{2}\left(\frac{\tau_{\text{opt}}}{\tau} + \frac{\tau}{\tau_{\text{opt}}}\right) \ , \tag{5.15}$$

where F is a factor of "demerit" related to the integral of the correspondingly filtered different noise contributions, τ is the shaping time constant used and τ_{opt} is the time constant that results in a noise minimum. When the optimal shaping time constant is selected, F gives directly the noise contribution relative to the ideal ENC. Some shaping filters are named after the shaping networks used (CR-RC, CR-(RC)^2), while others are called by the time dependent shapes of their impulse response functions: triangular, trapezoidal, Gaussian. For a triangular shaper ($F = 1.075$) of peaking time t_p, the contributions to the equivalent noise charge from the different sources as a function of the mismatch coefficient $m = C_{\text{Detector}}/C_i$ are:

1) From channel thermal noise:

$$\text{ENC}^2_{th} = 2kT\frac{\Gamma}{\omega_T}\left(m^{1/2} + m^{-1/2}\right)^2 \frac{A_1}{t_p}\, C_{\text{Detector}}. \tag{5.16}$$

2) Due to 1/f noise:

$$\text{ENC}^2_{1/f} = 2\pi H_{f^{-1}}\left(m^{1/2} + m^{-1/2}\right)^2 A_2 C_{\text{Detector}}\ . \tag{5.17}$$

3) From Lorentzian noise:

$$\text{ENC}^2_{L} = (2\pi)^2 H_L\left(m^{1/2} + m^{-1/2}\right)^2 A_3 t_p C_{\text{Detector}}\ . \tag{5.18}$$

4) From the feedback resistor:

$$\text{ENC}^2_{R} = \frac{4kT}{R_f C_t} A_3 t_p\ . \tag{5.19}$$

Where $A_1,\ A_2,\ A_3$ are the weighting integrals:

$$A_1 = \int_0^\infty |H(j\omega t)|^2\, d(\omega t)\ ,\ A_2 = \int_0^\infty \frac{|H(j\omega t)|^2}{\omega t}\, d(\omega t) \text{ and}$$
$$A_3 = \int_0^\infty \frac{|H(j\omega t)|^2}{\omega^2 t^2}\, d(\omega t)\ , \tag{5.20}$$

where $H(\omega)$ is the transfer function of the channel.

In order to measure the ENC of a preamplifier, a known charge is injected into the gate of the FET using a calibrated capacitor and a precision pulse generator, and the main amplifier gain adjusted for the corresponding voltage. Different, very stable, calibrated capacitors are then connected simulating different detector capacitances and the output amplitude then corresponds directly to the ENC in keV. The dependence on the detector capacitance can be established by this procedure. The input of the preamplifier is extremely sensitive and this point must always be adequately protected. When the connection is made with a BNC connector, a protective cover is mandatory in order to obtain a stable reading.

5.3 Performance of the preamplifier designed

In order to obtain a high quality current signal for each γ-event without compromising the energy resolution, a preamplifier was designed as part of this project (see appendix A for a detailed description). This section reviews the measured performance of this preamplifier.

The solution adopted first integrates the current pulse in the highly stable environment present in the detector cryostat in order to obtain a stable, low noise charge output. The detector current pulse is transformed to a voltage pulse by this integration and a subsequent differentiation is used to recover the detector signal. Since this differentiation is performed after the original pulse has already been transformed into a voltage waveform, the whole charge delivered by the detector is used for generating the energy signal.

As usual in germanium preamplifiers, the high voltage bias resistor, the coupling capacitor, the input FET and the feedback network are placed inside the cryostat on the so-called “cold” Printed Circuit Board (PCB). The critical connection between signal generator and preamplifier input is thus kept as short as possible.

The alternative of digitally deconvoluting the measured transfer function of the integrator from the energy output was considered, but had to be abandoned due to the poor quality of the test input. This input seems to be exclusively used for testing whether the FET is operating properly or not and the test pulse

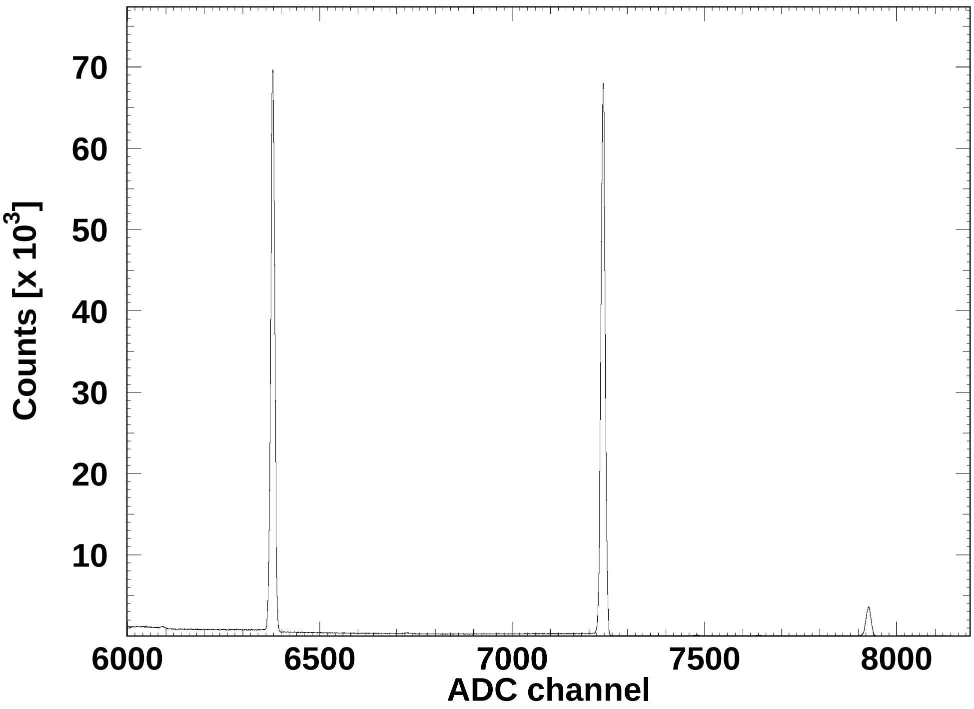

Figure 5.8: Upper part of the energy spectrum for a ^{60}Co source (lines at 1173.238 keV and 1332.502 keV) for the two-fold segmented CLUSTER module. The ^{40}K background line (1460.830 keV) is clearly visible on channel 7930.

was coupled so strongly to the other connections on the "cold" PCB that digital deconvolution proved impossible. Moreover, storing the full current pulses on tape would increase the event length beyond permissible levels and at the same time compromise the event throughput of the data acquisition system.

A sample energy spectrum acquired with the preamplifier designed and with a cooled input FET and Gaussian shaping with $t_{sh} = 3$ μs (Ortec 572) is shown in Fig. 5.8 for a ^{60}Co source. The peak FWHM under these conditions is 2.30 keV at 1333 keV and 2.27 keV at 1173 keV. This circuit has been implemented by the nuclear electronics group at the University of Cologne using Surface Mount Devices (SMD) as a candidate for use in the MINIBALL project and the measured resolution, with an unsegmented CLUSTER module, for their first prototype was also 2.3 keV at 1333 keV and 1.4 keV at 122 keV, where the contribution of the detector to FWHM is no longer noticeable. With a room temperature FET, as envisaged for the segment preamplifiers in MINIBALL, the measured resolution at the central contact was 2.9 keV at 1333 keV and 2.1 keV at 122 keV. The values that can be expected from the segments are worse than these measurements, due to the difference in output capacitance between the central contact ($\sim$ 56 pF) and the segments ($\sim$ 30 pF from the segment-capsule capacitance and $\sim$ 60 pF from the long cable demanded by the CLUSTER cryostat).

Further tests with the first 6-fold segmented CLUSTER module prototype [Pas97] have shown an improvement of the segment resolution from 3.5 keV (EURISYS segment preamplifier) to 2.9 at 1.33 MeV and room temperature FETs. Moreover, the resolution at the central contact was seen to be independent of whether the segments were grounded or connected to a preamplifier and was measured at 2.1 and 2.2 keV at 1.17 and 1.33 MeV, respectively, as opposed to 2.5 and 2.6 keV with the preamplifier provided by EURISYS (both using the same cold FET).

The intrinsic noise contribution of the preamplifier was measured with an FET operating at room temperature and seen to follow $\mathrm{ENC}\,(\mathrm{in\,eV}) = 650 + 35 \cdot C_D\,(\mathrm{in\,pF})$, using also a Gaussian shaping amplifier (Tennelec 242) and a slightly different shaping time (4 μs). The change in main amplifiers was used to discard any unreported influence of a particular main amplifier on the measurement. This measurement was repeated ($t_{sh} = 3$ μs) by the Cologne group for the SMD version of the preamplifier and a result of ENC (in eV) $= 1100 + 20 \cdot C_D$ (in pF) obtained.

The rise time of the preamplifier was measured using a warm FET at 12 ns with $C_D = 0\,\mathrm{pF}$, 45 ns with 54 pF, and 65 ns at 100 pF, without ringing present on the output pulse. No variations were observed at the output amplitude, indicating that the open loop gain of the amplifier is sufficiently large. The poor quality of the test input connection in the cryostat precluded performing these measurements with a cold FET. The stability against oscillations was tested by connecting a 250 pF capacitance, which is unrealistically large for a coaxial detector, as C_D. The energy output pulse then presented one full ringing period with a maximum overshoot of 38 % above the final amplitude. When the FET is cold, the long connection to the FET drain can be a source of undesired oscillations, but the final prototype of the preamplifier did not oscillate during any of the tests performed.

On the basis of the preamplifier performance and the compactness of the PCB (25 mm width, 40 mm length and 11 mm height) produced by the Cologne group for the SMD version, this circuit has been selected as the present candidate for both MINIBALL preamplifiers. The other candidates were two designs from EURISYS and commissioning the development of the preamplifiers to the nuclear electronics group at the Lawrence Berkeley Laboratory.

Chapter 6

Experimental Verification of the Interaction Radius Determination

Most of the considerations in previous chapters concerning the determination of the interaction radius have been performed employing ideal current pulses. The finite bandwidth of the electronics used to process the detector current pulses and any noise present on the signals can be expected to influence the radial resolution yielded by the various algorithms discussed in chapter 4. The non-ideal amplitude resolution when processing the current pulses will influence the applicability over a range of energies of the different methods and also needs investigating. In order to test the different radial determination methods that can realistically be employed with coaxial HPGe detectors for in-beam experiments, a series of measurements has been performed with the first prototype of a two-fold segmented CLUSTER module and the collimator, described in section 3.1, positioned at 0, 9, 17, 25 and 33 mm along one radius on the frontal surface of the module.

Of the alternatives presented in chapter 4, that of Strauss and Sherman was not included in this evaluation due to it being restricted to low γ-energies. The method proposed by Eschenauer was also discarded as a result of its sensitivity to the particular crystal, making it unsuitable for a detector array like MINIBALL. The T_{30}–T_{90} method was tested and an evaluation of this algorithm when the current pulses are integrated digitally can be found in [Gun97]. Due to the absence of a clear hardware implementation for in-beam experiments that would not compromise the event rate it will not be further discussed here.

Hence, only the time to maximum and the steepest slope methods are considered in this chapter, since both algorithms can be realised using analogue circuits and would therefore not compromise the event rate. However, in order to retain maximum flexibility for the present evaluation, the event current pulses were sampled with a 250 MHz flash ADC and stored on tape for each event together with the γ-energy. Two sources (^{137}Cs and ^{60}Co), providing three lines at 661.660, 1173.238 and 1332.502 keV, were employed for the measurements with the collimator. A third, monoenergetic, collimated source (^{57}Co, 122.0614 keV) was also used (see [Pal96, Gun97]) and seen to yield little radial resolution, since the γ-rays are stopped in the planar region of the detector.

Since the detector was not completely shielded from the surrounding environment, only those events corresponding to one of the γ-source energy lines have their entry position defined by the collimator. In the data analysis, the radial determination is therefore only performed when the measured γ-energy matches one of the γ-source lines. First results have been reported in [Pal96] and [Gun97].

6.1 The experimental setup

In order to investigate the radial resolution that can be expected when using CLUSTER crystals, the first prototype of a two-fold segmented CLUSTER module was employed to perform the measurements reported in this chapter. Since this work is concerned with the determination of the entry radius of γ-rays, only the signal from the central contact was used to evaluate the different algorithms. In a segmented detector, each segment electrode generates a signal dependent on the interactions that influence a mirror charge on the electrode, which includes interactions from a neighbouring segment occurring close to the segmentation plane. The signals at the segment electrodes therefore lead to ambiguous radial determination.

A detailed comparison between the time-to-maximum and the steepest slope algorithms was performed using the preamplifier delivered by EURISYS Mesures with the two-fold segmented CLUSTER module. This preamplifier does not have a "current" output and the event current pulses were regained by differentiating ($\tau_{\text{diff}} = 8$ ns) the "charge/energy" waveform. In order to bandlimit the signals, an integrator ($\tau_{\text{int}} = 11$ ns) was also included in the Timing Filter Amplifier (TFA) built by the electronics workshop of the Max-Planck-Institut für Kernphysik. The output of the TFA was digitised in one of the four channels of an 8 bit, 250 MHz flash ADC card designed by the nuclear electronics group at the University of Heidelberg [Wal92].

A second set of measurements was performed with the preamplifier designed as part of this project instead of the EURISYS preamplifier. The block diagram of the electronics used is shown in Fig. 6.1. With both preamplifiers, the "charge/energy" signal was processed by a traditional nuclear spectroscopy germanium channel and the event energy converted with a 13 bit spectroscopy ADC designed at the Max-Planck-Institut für Kernphysik. The "current" output of the preamplifier was bandlimited before it was sampled using the mentioned flash ADC.

An event was acquired whenever a CFD output pulse was produced and the data acquisition system was not busy collecting event data. In order to reduce

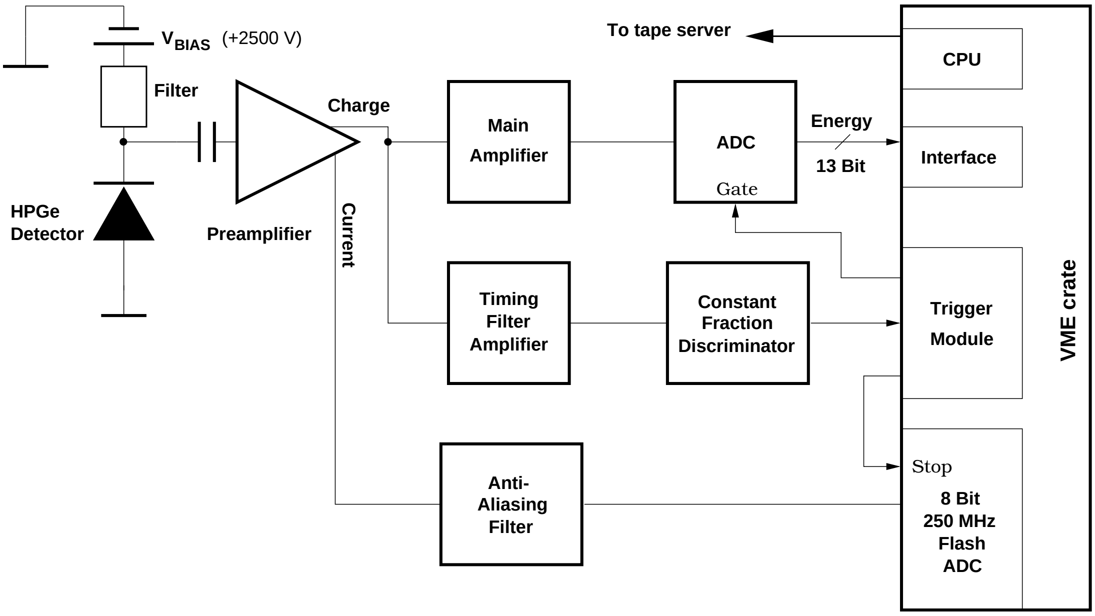

Figure 6.1: Block diagram of the electronics used for the acquisition of data when using the new preamplifier.

the amount of events not corresponding to one of the γ-source lines, the threshold for the CFD was set at a comparatively high energy. The continuously sampling flash ADC was then stopped by a delayed copy of the CFD signal, ensuring that the event current pulses were stored in the 2 kByte/channel ($\sim$ 8.2 μs) sample memory. The data were collected by a VME CPU (Cetia VMTR2) in the same crate where the trigger card, the interface card for the spectroscopy ADC and the flash ADC card were located.

The event throughput was limited by the number of flash ADC samples that were read out, since the same number of samples must be read out for all four channels. In order to minimise the dead time, only the last part ($\sim$ 2 μs) of the 2 kByte sample memory was read out and two PowerPC CPUs were used, one for gathering the event data on the VME crate and the other for transporting the data via Ethernet to the workstation where the tape drive is located. The on-line analysis running on this workstation could perform the time to maximum and the steepest slope algorithms for over 90 % of events corresponding to one γ-source energy line. When the current pulses were not included as part of the event data, the maximum rate measured was $\lesssim$ 2000 Events/s with an uncollimated source. When sufficient samples from the current pulse at the core electrode were read out for the determination of the entry radius, the maximum count rate was $\sim$ 750 Events/s. With collimated sources, the event rate when the current pulses were acquired was position dependent and varied between 100 and 300 Events/s.

The performance of the flash ADC channels was tested by sampling delta-like pulses produced by an AVTECH AVP-1-C pulse generator. These pulses had 2 ns pulse width, 135 ps fall- and rise-times and amplitudes that were varied over the -2 to 0 V ADC input range. The response to those pulses was either no change in the small DC offset or one sample at the correct amplitude, depending on the position of the delta-like pulse relative to the ADC sampling clock (4 ns). The flash ADC and its associated input stages can therefore be considered as having no influence on the sampled signals.

Although the variations in maximum amplitude among current pulses are smaller than those of charge pulses, the 8 bit dynamic range of the available flash ADC is the major limitation to the possible γ-energies for which the entry radius was determined simultaneously. At the lower end of the dynamic range, the pulses become indistinguishable from the noise level at the ADC input and neither the maximum nor the derivative can be calculated. At the other extreme of the dynamic range, where the 8 bit range corresponds only to the lower amplitude values of event current pulses, the sampled pulses take the maximum ADC value (clipping distortion) for almost the complete pulse duration: They rise quickly to the maximum value, stay there for the duration of the pulse and then quickly drop to the DC level. In those pulses, the t_{max} value is assigned to the first sample reaching the maximum amplitude since no later sample has a greater value. The absolute minimum of the first derivative occurs at the last clipped sample and

t_{slope} is accordingly assigned to this sample. The structure of the current pulses is lost in both cases.

In the measurements with the new preamplifier, a single order Butterworth filter was used as anti-aliasing filter in order to modify the phase information of the current pulses as little as possible. The transfer function of this type of filter imposed a rather low -3 dB frequency ($\tau = 6$ ns, $f_{-3\mathrm{dB}} = 38$ MHz). Although this is less than a third of the 125 MHz Nyquist frequency, the highest frequency that can be resolved, it will be seen that the radial resolution would be preserved even when sampling at $(1/4) \cdot 250$ MHz. A gain stage was also included in this anti-aliasing module in order to exploit the full input range of the flash ADC. The gain was adjusted to provide adequate amplitude resolution for γ-energies between 600 and 1400 keV and a compromise gain setting for both energies used.

In the measurements performed using the EURISYS preamplifier, the gain on the "current" signals was adjusted for each γ-ray source energy to overcome the limited dynamic range of the flash ADC. It should however be mentioned that this limitation in the dynamic range will be overcome in the final, analogue implementation of the radial determination algorithm.

6.2 Analysis and Results

From the buffer memory where the current pulses were stored, 500 samples (2 μs) were read out and written on tape. In order to eliminate the variations (jitter) between the occurrence of the stop signal (CFD logic pulse) and the actual start of the current pulse, a time origin was extracted from each pulse in the digital domain. The restriction to just one γ-energy and the abrupt rising edge present on all event current pulses enabled the determination of this time origin by simply comparing the samples with a fixed amplitude threshold (leading edge timing

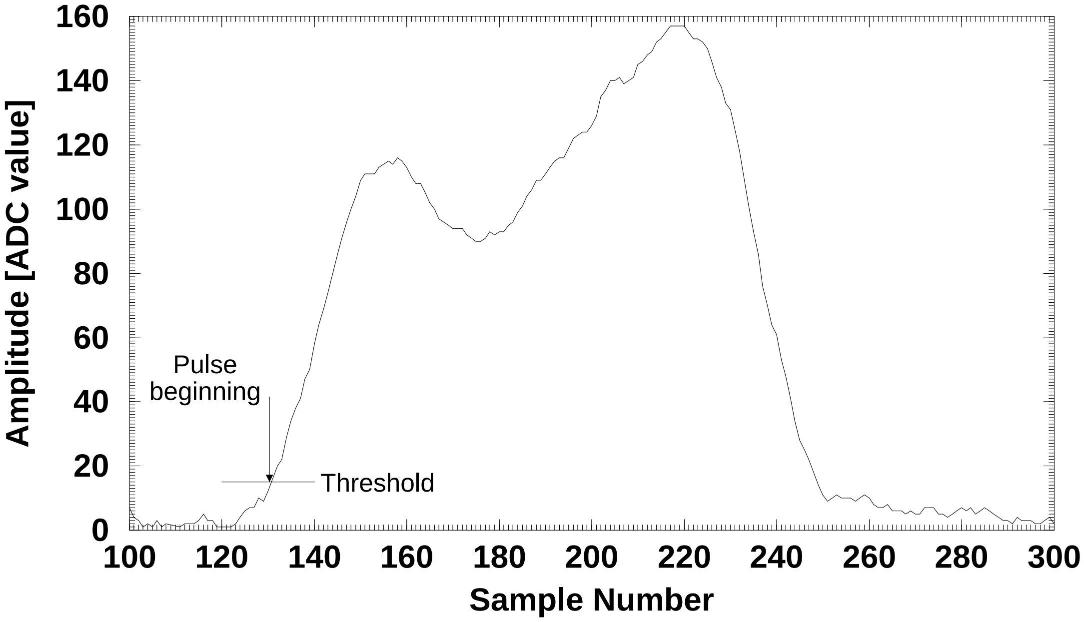

Figure 6.2: Sampled “single interaction”-like current pulse for a collimated 1333 keV beam centred at $r = 33$ mm. The sampling period is 4 ns.

in nuclear electronics terms). The time origin is used to time-align all event current pulses and both t_{max} and t_{slope} are measured relative to this time origin. The amplitude threshold was also used to determine if the current pulse had been completely missed by the flash ADC sampling window and those few events discarded.

Fig. 6.2 shows as an example a “single-interaction” event current pulse, acquired using the new preamplifier, for 1333 keV γ-rays entering the detector at $r = 33$ mm. Both leading and final edges, which are ideally abrupt, show 80 ns rise- and fall-times ($90\% - 10\%$), much longer than expected from the bandwidth at the current output of the preamplifier (17 MHz, see Fig. A.3), the anti-aliasing filter and the ADC: total $t_{\text{rise}} \sim 20$ ns. The dominating contribution to this slow rise-time must be due to the detector and/or the coupling to the input stage of the preamplifier. Further investigations are required to completely understand this reduction of bandwidth on the sampled event current pulses.

6.2.1 The difference function

While t_{max} can be determined by simply scanning the samples, t_{slope} requires the evaluation of the difference function introduced in section 2.3.1. For the sampled current pulses $i[kT_s]$, the difference function $d[kT_s]$ is calculated from

$$d[kT_s] = i[kT_s] - i[(k - \Delta k)T_s] \ , \qquad (k = \Delta k + 1, 2, \ldots) \ , \tag{6.1}$$

where $T_s = 4$ ns is the sampling period and k is the sample number. The value of kT_s for which the absolute minimum of $d[kT_s]$ occurs is assigned to t_{slope}.

A basic difference between an analogue and a digital differentiator should be pointed out here. In an analogue differentiator, increasing the differentiation time constant, intuitively equivalent to increasing Δk, reduces the high-frequency components present in the signal and is therefore done in order to eliminate high-frequency noise. In the digital domain, however, increasing Δk affects the frequency response in a different manner. The Z transform of eq. 6.1 is

$$H(z) = \frac{D(z)}{I(z)} = 1 - z^{-\Delta k} \ , \tag{6.2}$$

which corresponds to a finite impulse response filter of length Δk. This filter introduces a group delay $(\Delta k)/2$ on $d[kT_s]$ relative to $i[kT_s]$. When Δk is odd, there is an uncertainty as to whether the resulting group delay is $(\Delta k - 1)/2$ or $(\Delta k + 1)/2$. As each pulse $i[kT_s]$ is individually time aligned, the group delay in $d[kT_s]$ can vary among pulses and produce a "comb" effect in the resulting event distributions. The group delay is well defined for even Δk and only displaces the absolute position of the event distributions.

The transfer function of the digital differentiator (eq. 6.2) has a pole of order Δk at the origin ($z = 0$) and Δk zeros on the unit circle. Each zero on the unit circle, $z_0 = \mathrm{e}^{j\varphi_z}$, corresponds to a notch filter at the frequency $f_z = (\varphi_z/2\pi) \cdot f_s$, where f_s is the sampling frequency. Since the Nyquist frequency $f_N = (1/2)f_s$,

Δk	Centre frequencies [MHz]					
1	0					
2	0	125.0				
3	0	83.3				
4	0	62.5	125.0			
5	0	50.0	100.0			
6	0	41.6	83.3	125.0		
7	0	35.7	71.4	107.1		
8	0	31.3	62.5	93.8	125.0	
9	0	27.8	55.6	83.3	111.1	
10	0	25.0	50.0	75.0	100.0	125.0

Table 6.1: Centre frequencies of the notch filters introduced by the digital differentiator as a function of the sample distance Δk for 250 MHz sampling frequency.

the highest frequency that can be resolved, corresponds to $\varphi = \pi$, all notch filter centre frequencies from zeros with $\varphi_z > \pi$ do not affect the signal bandwidth and are therefore not listed in table 6.1.

The centre frequencies of the notch filters are listed in table 6.1 for $\Delta k \leq 10$. There is always a zero at DC ($\varphi_0 = 0$, $f_0 = 0$), as expected for a differentiator, and the effect of increasing Δk is to reduce the first corner frequency of the differentiator. Since the anti-aliasing filter has a bandwidth of 38 MHz, no noticeable effects can be expected in the measurements with the new preamplifier for $\Delta k \leq 7$.

6.2.2 Comparison of the time to maximum and the steepest slope methods

The measured event distributions for t_{slope}, $N(t_{\text{slope}})$, (see Figs. 6.3(a),(b)) reproduce closely the calculated distributions (Fig. 4.5) and of drift times of majority carriers from the main interaction, confirming the predicted $r_{\text{main}}/t_{\text{slope}}$ correspondence. Note that the tails to shorter t_{slope} agree very closely with those in

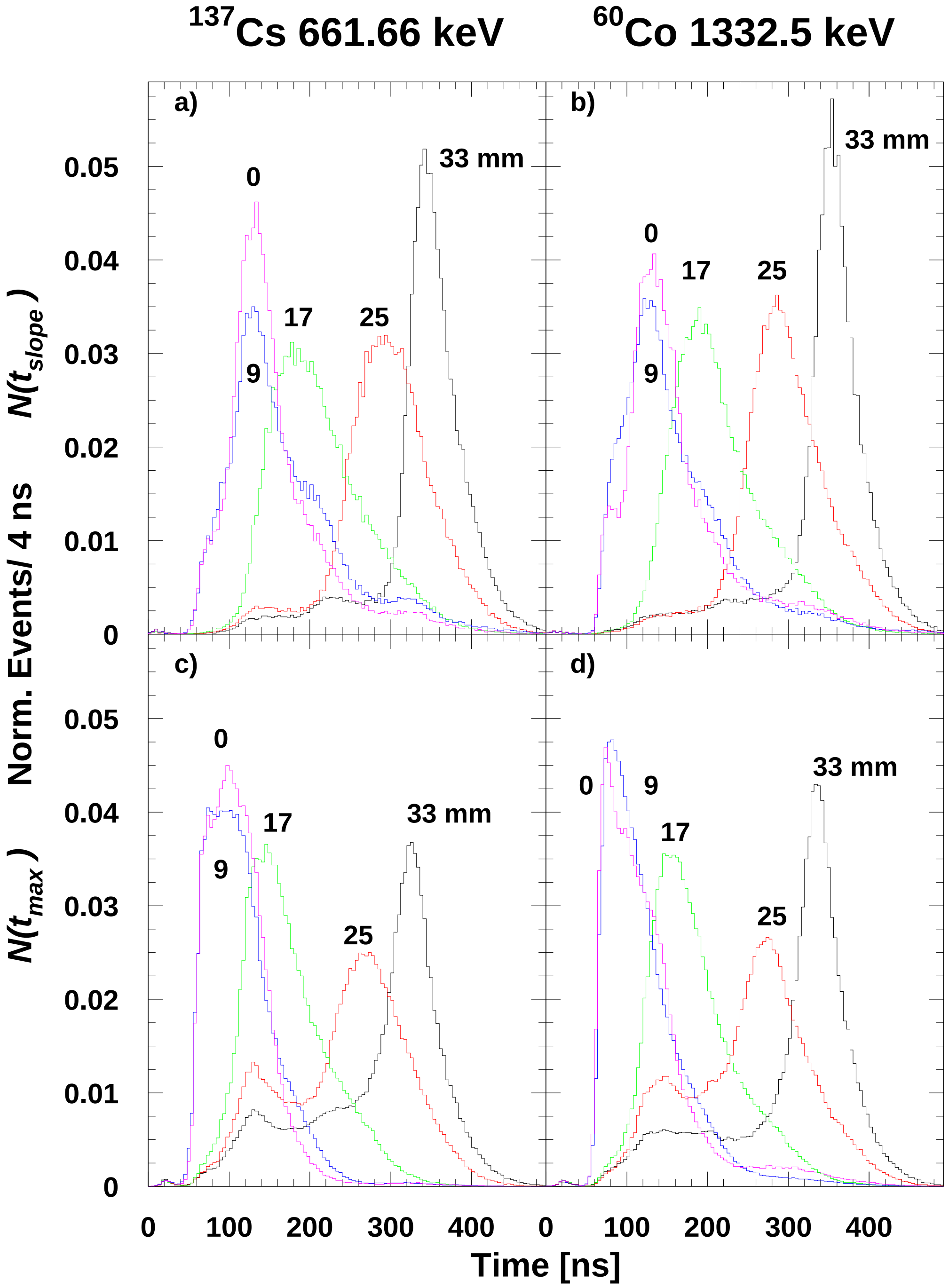

Figure 6.3: Normalised event distributions $N(t_{\text{slope}})$ (a,b) and $N(t_{max})$ (c,d) at the energies shown. The collimator was centred at r = 0, 9, 17, 25 and 33 mm and the gain for the current pulses adjusted for each γ-energy.

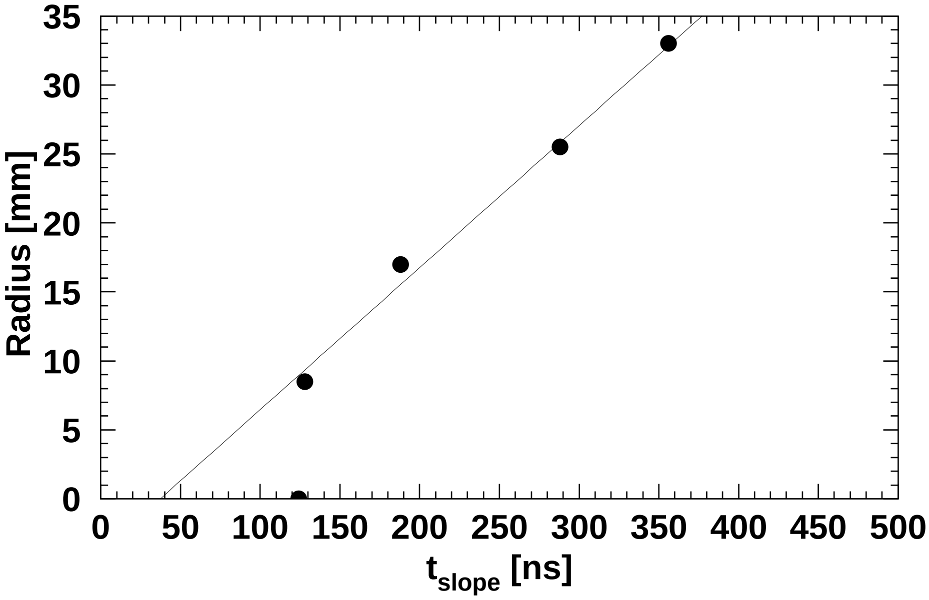

Figure 6.4: Experimental dependence of the interaction radius as a function of t_{slope}. The data points show the median of the $N(t_{\text{slope}})$ distributions at the respective collimator position.

the predicted distributions. All distributions present an offset of about 60 ns, due to the finite bandwidth of the electronics used to process the event current pulses. Once this offset is removed, the largest difference between the median of the distributions and the calculated values is 15 ns, equivalent to 1.5 mm, for both γ-energies.

It is therefore possible to use these data to perform a calibration

$$r \text{ (mm)} = 0.1 \cdot t_{\text{slope}} \text{ (ns)} - 3.8 \ , \tag{6.3}$$

as shown in Fig. 6.4 and which confirms the predicted (see section 3.2.4) 10 ns/mm. The calibration is independent of γ-energy since the median values of the distributions are the same for the γ-energies investigated. At lower energies, an energy dependence is expected due to the increasing fraction of events, as the γ-energy decreases, with their main interaction outside of the coaxial region of the crystal.

From the $N(t_{\text{slope}})$ distributions, the average radial resolution for $r \geq 9$ mm is $<\Delta r>$ (FWHM) $\sim$ 10 mm. From the predicted event distributions, the average contribution of the collimator is $< \Delta r >$ (FWHM) $\sim$ 6 mm. Therefore, the resolution of the steepest slope method can be estimated at $<\Delta r>$ (FWHM) $\sim$ 8 mm.

The measured event distributions for t_{max}, $N(t_{max})$, (Figs. 6.3(c),(d)) do not show such a good agreement with the predicted distributions (shown in Fig. 4.1), which were calculated using ideal, noise-free event current pulses and nearly ideal amplitude resolution. There is a considerable faction of events assigned to smaller radii than the irradiation radius. This was not as clearly visible in the predicted event distributions, so it is clear that the finite bandwidth and amplitude resolution compromise the time to maximum method more severely than they affect the steepest slope determination.

6.2.3 First measurements with the new preamplifier

The new preamplifier developed as part of this thesis (see section 5.3 and appendix A) has a “current” output (a voltage replica of the detector current pulse) with higher bandwidth than the EURISYS preamplifier, without compromising the energy resolution. In order to test the quality of the current output, first tests have been performed with the final prototype of the preamplifier. Further tests will be performed with the definitive version of the SMD preamplifier currently being developed in collaboration with the University of Cologne nuclear electronics group. Fig. 6.5 shows that the resolution and linearity are comparable to the measurements using the EURISYS preamplifier (Fig. 6.3).

The event current pulses were digitally re-sampled at $(1/4)\cdot f_s = 62.5$ MHz and processed by the steepest slope method (see Fig. 6.6). The bandwidth limitation

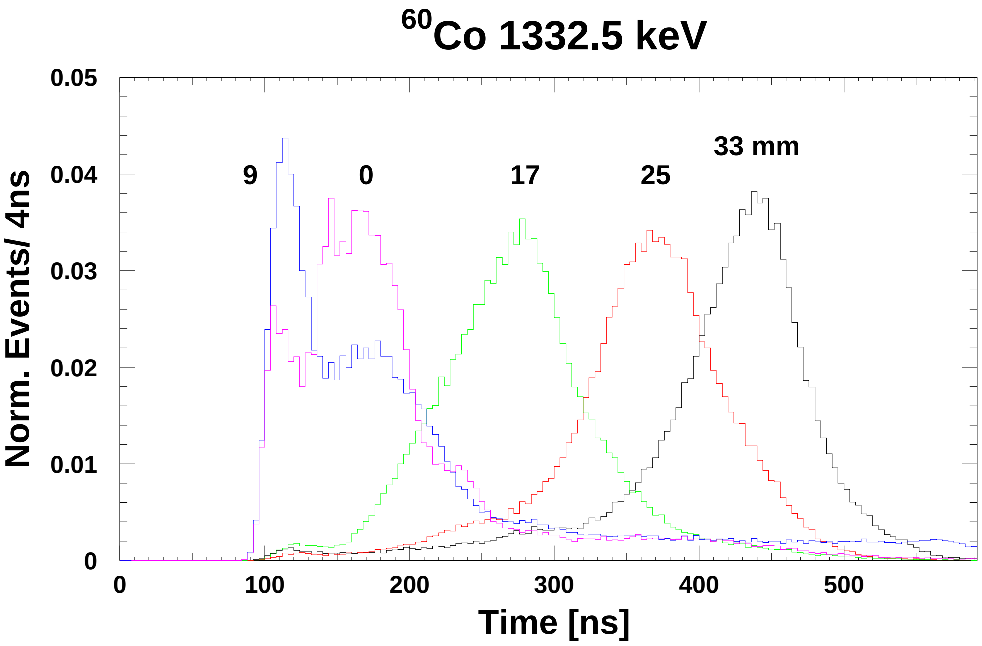

Figure 6.5: Normalised event distributions $N(t_{\mathrm{slope}})$ at 1333 keV γ-energy. The collimator was centred at r = 0, 9, 17, 25 and 33 mm.

indicated by the $\sim$ 80 ns rise- and fall-times guarantees that the signals are bandlimited and no further anti-aliasing filtering was performed. Note that the time uncertainty becomes four times larger (16 ns), resulting in the larger bin width seen in Fig. 6.6. The minimum t_{slope} is nevertheless roughly equivalent to 1.6 mm. It is still much smaller than the radial resolution, which is left unchanged at ± 8 mm.

The negligible loss of radial resolution when using the resampled event current pulses relaxes the bandwidth specification of the steepest slope analogue implementation. Furthermore, it indicates that an ADC with sampling frequency $f_s \gtrsim 50\ MHz$, which could easily have a dynamic range larger than the 8 bits used in these measurements, would not compromise the radial resolution that can be achieved with a CLUSTER module. In order to leave the event throughput unaffected, though, the processing would have to be integrated locally to these

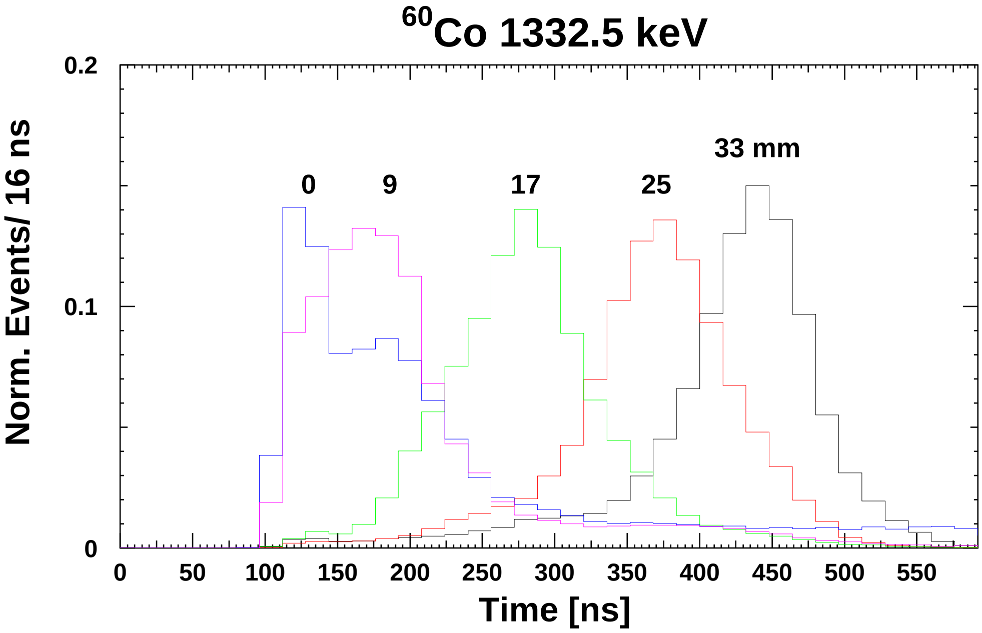

Figure 6.6: Normalised event distributions $N(t_{\text{slope}})$ for the shown collimator positions when the current pulses are re-sampled at $(1/4) \cdot f_s = 62.5$ MHz.

ADCs.

6.3 Applicability to in-beam experiments

The measurements reported show that the t_{slope} parameter can successfully determine the radius of the main interaction for full energy events. Comparing the measured and the predicted event distributions at both γ-energies (662 keV, 1333 keV) results in an average resolution for the radial determination of ±4 mm.

The radial resolution enables the division of the CLUSTER module electronically into at least 4 radial regions. If each region is assigned a number k, the radius r can be determined following $(k-1) \leq r$ (mm) $\leq k \cdot 9$. The six-fold segmentation of the outer electrode of the crystal (denoted by l), which produces φ domains and yields $(l-1) \cdot 60 \leq \varphi$ (deg) $\leq l \cdot 60$. Combining both coordinates, a $6 \cdot 4 = 24$ fold subdivision of the solid angle subtended by each crystal is achieved.

This increased granularity will improve the energy resolution of these segmented detectors when measuring γ-rays from a moving source and therefore must be Doppler corrected.

A digital alternative to the analogue implementation of the steepest slope method, presently under development, could use a flash ADC with $\sim$ 50 MHz sampling frequency and still retain the ± 4 mm radial resolution. In order to leave the event throughput unaffected, though, the processing would have to be integrated locally to these ADCs. The reduction in sampling frequency would at present enable the use of at least a 12 bit ADC, which would increase the range of γ-energies for which the entry radius could be determined without using two ADC channels.

Chapter 7

Conclusions

A method for the determination of the entry position of γ-rays in coaxial germanium detectors over a range of γ-energies is needed to reduce the Doppler broadening of energy peaks in many in-beam nuclear spectroscopy experiments. The steepest slope method (see section 2.3.1) was introduced as a possibility of determining the main interaction radius r_{main}. The method measures the drift time of majority charge carriers liberated by the main interaction in an event by studying the current pulse generated by the HPGe detector as a result of the energy liberated in the detection process.

As part of the evaluation of the steepest slope method for determining r_{main}, a new preamplifier for germanium detectors has been developed (see section 5.3 and appendix A). This circuit presents the basis of the present Heidelberg-Cologne surface mount preamplifier, which is a strong candidate for MINIBALL and is also being considered by the American project GRETA and the French EXOGAM. The "current" signal (in Volt) is output without compromising the performance of the traditional "charge/energy" pulses, as proved by the measured energy resolution (2.30 keV at 1333 keV with cold input FET). Furthermore, the energy resolution with room temperature FET (2.9 keV at 1333 keV), as envisaged for the segment energy signals, shows a substantial improvement over the EURISYS segment preamplifier (3.5 keV at 1333 keV). The input impedance is also superior, since the new preamplifier does not affect the energy resolution at the central electrode. Additionally, the increased bandwidth at the "charge/energy" output, compared to the EURISYS preamplifier employed in the EUROBALL CLUSTER composite detectors, should result in an improved time resolution.

The non-deterministic nature of γ-ray detection poses a limit to the position resolution that can be achieved in a germanium crystal. A thorough Monte Carlo simulation of the interactions (positions and energies) needed to completely stop a γ-ray in a germanium detector has been performed (chapter 3) in order to investigate the distribution of the event energy among interactions. It was seen that the position of the main interaction is a good measure of the entry position over a wide range of γ-energies and therefore can be used for determining the direction of γ-rays. The drift time of majority carriers $t_{\mathrm{drift}_{maj}}$ (section 3.2.4) present a clear radial dependence for most of a CLUSTER crystal volume of approximately 10 ns/mm. Calibrating a detector for radial resolution involves restricting the possible γ-entry radii. It is necessarily a time consuming process when several detectors have to be calibrated for the different radii, as would be required in MINIBALL. It was also shown that the $t_{\mathrm{drift}_{maj}}$ differences for different impurity concentrations are small. Therefore, crystals with similar impurity concentration need not be individually calibrated. Furthermore, radial resolution methods based on majority carrier drift time should not present a high sensitivity to neutron damage in the crystal.

The results predicted when irradiating a CLUSTER module with a collimator (see chapter 4) have been confirmed by the measurements performed (see chapter 6). The reduced resolution at small irradiation radii subtends a small solid angle compared to the rest of the crystal and is therefore of little relevance for in-beam experiments, where the full frontal surface of the detector is exposed to γ-

rays. The energy independent, linear correlation between the radius of the main interaction in a detector event and the measured time t_{slope} has been confirmed, enabling the determination of the γ entry radius in the detector. The measured radial resolution is better than ± 4 mm, even when the event current pulses are re-sampled at a fourth of the original 250 MHz sampling frequency.

The electronics employed in this thesis to perform the steepest slope radial determination provide a very high flexibility for investigating the influence of different parameters. They are however impractical, without further development, for a multi-detector array. Sampling the event current pulses would only be practical if dedicated logic is developed and only the resulting t_{slope} value is added to the event data. Although the radial resolution is maintained at the much lower sampling frequency of 62.5 MHz, each event current pulse requires some 50 samples. Even with an 8 bit ADC, this data volume for one crystal is equivalent to the entire conventional parameter set (energy and time) of nearly 14 detector elements and would seriously compromise the event throughput of the data acquisition system. Therefore, an analogue implementation of the steepest slope method is currently under development at the Max-Planck-Institut für Kernphysik in Heidelberg. Since 8 bit would divide the detector into 256 radial sectors, the increment in data for each multi-detector event is just one Byte for each crystal in the event.

The combination of the measured radial resolution and the segmentation of the outer electrode in a six fold segmented CLUSTER module enables an increase in the granularity of the detector array by a factor of 24. Therefore, a substantial improvement of the energy resolution for γ-rays emitted by a moving source is possible using the method proposed in this thesis.

Bibliography

[Arm74] G. A. Armatrout *et al., Encapsulation of High-Purity Germanium Detectors,* IEEE Tr. Nucl. Sci., 21, 1, 1974, 344-346.

[CER84] CERN Program Library, *Poiscr, Solution of Poisson's or Laplace's Equation in Two-Dimensional Regions,* CERN, Geneva, 1984, Publication T604.

[CER93] CERN Application Software Group , *GEANT 3.21 - Detector Description and Simulation Tool*, CERN, Geneva, 1993.

[Cor74] R. A. Corley, *An improved technique for the growth of ultra-pure Germanium,* IEEE Tr. Nucl. Sci., 21, 1, 1974, 342-343.

[Deb88] K. Debertin and R.G. Helmer, *Gamma- and X-ray Spectrometry with Semiconductor Detectors*, North-Holland, Amsterdam, 1988.

[Ebe92] J. Eberth, *Development of a Composite Ge Detector for EUROBALL,* Prog. in Part. and Nucl. Phys., 28, 1992, 485-504.

[Ebe97] J. Eberth *et al., Development of Segmented Ge Detectors for Future γ-Ray Arrays,* Prog. in Part. Nucl. Phys., 38, 1997, 29-37.

[Esc94] M. Eschenauer *et al., Resolution enhancement of gamma-spectroscopy data from neutron -damaged coaxial n-type HPGe-detectors,* Nucl. Instr. & Meth., A340, 1994, 364-370.

[Eur92] *EUROBALL III, European γ-ray facility, Version 4.1,* J. Gerl and R.M. Lieder, eds., Dec. 1992.

[Fis97] C. Fischbeck, Diploma Thesis, LMU Munich, *in preparation.*

[Gat75] E. Gatti, P.F. Manfredi, *Low Noise Current Preamplifiers for Large Capacitance Semiconductor Detectors and high Counting Rates,* Proc. 2nd. ISPRA Nucl. Electr. Symp., Publication EUR 5370 e, 1975, 33-45.

[Gat78] E. Gatti, P.F. Manfredi, *Signal Coupling from a Semiconductor Detector to a Cold Resistance Preamplifier through a Cable or a Delay-Line transformer,* IEEE Trans. on Nucl. Sci., 25, 1, 1978, 66-74.

[Gou69] F.S. Goulding *et al., An opto-electronic feedback preamplifier for high resolution nuclear spectroscopy,* Nucl. Instr. & Meth., 71, 1969, 263-275.

[Gou72] F.S. Goulding, *, Pulse-Shaping in Low-Noise Nuclear Amplifiers: A Physical Approach to Noise Analysis,* Nucl. Instr. & Meth., 100, 1972, 493-504.

[Gou94] F.S. Goulding, D.A. Landis, *GAMMASPHERE-Correction Technique for Detector Charge Trapping*, IEEE Trans. on Nucl. Sci., 41, 4, 1994, 1145-1149.

[Gra93] P.R. Gray, R.G. Meyer, *Analysis and Design of Analog Integrated Circuits, 3rd ed.,* John Wiley & sons, new York, 1993.

[Gra96] J.G. Graeme, *Photodiode Amplifiers, op amp solutions,* McGraw-Hill, New York, 1996.

[Gun97] Ch. Gund, *Eigenschaften des zweifach segmentierten Prototypen eines MINIBALL Cluster Moduls*, Diploma Thesis, Max-Planck-Insitut für Kernphysik, Heidelberg, 1997.

[Gut96] D. Gutknecht, Private communication, Eurisys Mesures, Strasbourg.

[Gut97] D. Gutknecht, *Slide report,* MINIBALL user's meeting, Garching, April 1997.

[Hal74] R.N. Hall, *Chemical Impurities and Lattice Defects in High-Purity Germanium,* IEEE Tr. Nucl. Sci., 21, 1, 1974, 260-272.

[IEE93] *IEEE Standard Test Procedures for High-Purity Germanium Crystals for Radiation Detectors,* The Institue of Electrical and Electronic Engineers, New York, 1993.

[Kno89] G.F. Knoll, *Radiation detection and measurement, 2nd ed.*, John Wiley & Sons, New York, 1989.

[Koe95] M. Koenen *et al. , Radiation Damage in Large-Volume n- and p-Type High-Purity Germanium Detectors Irradiated by 1.5 GeV Protons,* IEEE Tr. Nucl. Sci., 42, 4, 1995, 653-658.

[Krö96] Th. Kröll *et al.* , *Analysis of simulated and measured pulse shapes of closed-ended HP-Ge detectors*, Nucl. Instr. & Meth., A371, 1996, 489-496.

[Leo87] W.R. Leo, *Techniques for Nuclear and Particle Physics Experiments,* Springer-Verlag, Berlin, 1987.

[Man95] Manfredi, P.F., Re. V, Speziali, V., *JFET preamplifiers for low noise applicatons in calorimetry and radiation spectroscopy,* Nucl. Phys. B (Proc. Suppl.), 44, 1994, 613-616.

[Mil67] J.K. Millard, T.V. Blalock, *A Low-Noise Wide-Band Current Preamplfier for use with Semiconductor Detectors,* Proc. of the 1967 Gattlingsburg Conf. on Semicond. Nucl. Part. Detectors, Publication 1593, Nat. Acad. of Sciences, Washington, 1969, 476-483.

[Mil72] J.K. Millard, T.V. Blalock, N.W. Hill, *A Broadband Current Preamplifier Configuration for Obtaining High Resolution Energy and Timing Information from Nuclear Radiation Detectors,* IEEE Trans. on Nucl. Sci., 19, 1, 1972, 388-394.

[Muk76] T. Mukoyama , *Range of Electrons and Positrons*, Nucl. Instr. & Meth., 134, 1976, 125-127.

[Net81] Y. Netzer, *The Design of Low-Noise Amplifiers,* Proc. IEEE, 69, 6, 1981, 728-741.

[Nic74] P.W. Nicholson, *Nuclear Electronics*, John Wiley & Sons, London, 1974.

[Ort95] EG&G Ortec, *Modular Pulse-Processing Electronics and Semiconductor Radiation Detectors*, EG&G Ortec, Oak Ridge, 1995.

[Ott75] G. Ottaviani *et al.*, *Charge carrier transport properties of semiconductor materials suitable for nuclear radiation detectors,* IEEE Trans. on Nucl. Sci., 22, 1, 1975, 192-204.

[Pal96] L. Palafox *et al.*, *Position resolution in HPGe hexaconical γ-ray detectors*, Poster presented at the 1996 Spring meeting of the German, Austrian and Swiss Physics Societies, Stuttgart 1996.

[Pas97] G. Pascovici, Private communication, Nuclear Physics Institute, Cologne University.

[Pel82] D. Pelte and D. Schwalm, *Heavy Ion Collisions,* North-Holland, Amsterdam, 1982.

[Poe67] D. Poenaru, *Collection time of Electron-Hole pairs in a Coaxial Ge(Li) Radiation Detector,* IEEE Tr. Nucl. Sci. , 14, 5, 1967, 1-7.

[Rad70] V. Radeka, *Charge amplification without the charge leak resistor,* IEEE Trans. on Nucl. Sci., 17, 3, 1970, 433-439.

[Rad74] V. Radeka, *Signal, Noise and Resolution in Position-Sensitive Detectors,* IEEE Trans. on Nucl. Sci., 21, 1, 1974, 51-64.

[Rad88] V. Radeka, *Low-noise Techniques in Detectors,* Ann. Rev. of Nucl. Part. Sci., 38, 1988, 217-77.

[Rau82] T.W. Raudorf, M.O. Bedwell, T.J. Paulus, *Pulse shape and rise-time distribution calculations for HPGe coaxial detectors*, IEEE Trans. on Nucl. Sci., 29, 1, 1982, 764-768.

[Re95] Re. V, Svelto, F., *High Accuracy Measurement of Low-Frequency Noise in Front-End P-channel FETs,* Nucl. Phys. B (Proc. Suppl.), 44, 1994, 607-612.

[Sch91] C. Schiller and P. Byrne, *A 4-GHz 8-b ADC System,* IEEE Jour. of Sol. State Circ., 26, 12, 1991, 1781-1789.

[Sch92] S. Schwebel, *Pulsform-Analyse von High Purity Germanium-Detektoren mit Flash ADC's*, Diploma Thesis, Max-Planck-Institut für Kernphysik, Heidelberg, 1992.

[She74] I.S. Sherman and M.G. Strauss, *Gamma-ray Position Sensitive Coaxial Ge(Li) Detector,* Nucl. Instr. & Meth. , 117, 1974, 285-294.

[Str72] M.G. Strauss and I.S. Sherman, *Coaxial Ge(Li) gamma-ray camera,* IEEE Trans. on Nucl. Sci., 19, 3, 1972, 219-225.

[Sun92] S. Sun, *Conception et hybridisation d'une chaîne d'amplification spectrométrique a bas bruit de fond,* PhD Thesis, CRN Strasbourg, CRN 92-44, 1992.

[Sze81] S.M. Sze, *Physics of Semiconductor Devices, 2nd ed*, John Wiley & Sons, New York, 1981.

[Tho93] H.-G. Thomas *et al., Neutron induced damage of an n-type Ge detector. Influence of the operating temperature*, Nucl. Instr. & Meth., A332, 1993, 215-219.

[Tho95] H.-G. Thomas, *Entwicklung eines Germanium-CLUSTER-Detektors für das Gamma-Spektrometer EUROBALL*, Verlag Dr. Köster, Berlin, 1995.

[Tov61] P.A. Tove, K. Falk, *Transit time of Charge Carriers in the Semiconductor Ionization Chamber,* Nucl. Instr. & Meth., 12, 1961, 278-290.

[Wal92] P. von Walter, A. Rausch, *A 1 GHz Flash-ADC Module in VME-bus*, IEEE Trans. on Nucl. Sci., 39, 4, 1992, 776-779.

[Wei93] T. Weiland, *MAFIA - The General Purpose Electromagnetic Simulator*, Version 3.21, Darmstadt, 1993.

[Wic74] R. Wichner *et al., High Purity Germanium – Low Temperature Analyses,* IEEE Tr. Nucl. Sci., 21, 1, 1974, 273-278.

Appendix A

A preamplifier for coaxial HPGe detectors

The circuit diagram of the preamplifer designed in order to produce high quality charge/energy and current waveforms from a HPGe detector is shown in Fig. A.1. This is the first time for a number of years that a preamplifier for large volume germanium detectors has been designed in a research group other than the Berkeley one.

The operational amplifier designed for using as a charge sensitive preamplifier with large volume coaxial detectors consists of a FET-bipolar cascode stage (T_{in}, P_1) with active load (T_{curr1}) and an output buffer (P_2, P_3, $op1$). The energy output is produced after shortening the decay time constant of the integrated pulses with a pole-zero cancellation stage (VR_{pz}, C_{pz}; see below) and correcting the DC offset (VR_2) at the output of the integrator. The current waveform results from differentiating the output of the integrator before any further filtering is performed.

The operational amplifiers $op2$ and $op3$ are capable of driving a terminated 50 Ω cable and R_{out} and R_{out2} provide 50 Ω output impedance. Both outputs (energy and current) and the test input use BNC connectors at present. In the further development of this circuit for MINIBALL, it has been decided to use SMA connectors due to their smaller size and good high frequency properties. Commonplace Lemo00 connectors were rejected due to their unsatisfactory ground contact, on the experience that the energy resolution of a germanium channel depends on the rotation angle of the Lemo00 connector used for the charge signal.

The input transistor T_{in}, the feedback network ($R_{fb} \parallel C_{fb}$), the final high voltage biasing resistor R_{bias}, the coupling capacitor C_{hv} and the test capacitor are all placed in the "cold" PCB provided by EURISYS. The test input is not terminated close to the test capacitor, which is in part responsible for the high level of crosstalk observed between the test input and all other signal connections on the "cold" PCB.

A.1 The DC operating point

All supply voltages are filtered on the circuit board with low-ohm inductances and large tantalum capacitors. There is a voltage drop across the inductances and the transistor stages operate with $\pm 11.75\,\mathrm{V}$ instead of the indicated $\pm 12\,\mathrm{V}$. In order to maintain the symmetry of the supply voltages, the high current needed by the FET, filtered by L_1 and C_{fil}, is routed directly from the power supply connector, so that the voltage drops across L_3 and L_4 are equal. The energy resolution improved by 150 eV after separating the supply for the input stage. The supply for the operational amplifiers has a smaller contribution to the output noise and is thus filtered with ferrite beads and large capacitors. All 100 nF blocking capacitors are placed as close to the sensitive pin (base of transistor or operational amplifier supply connection) as possible.

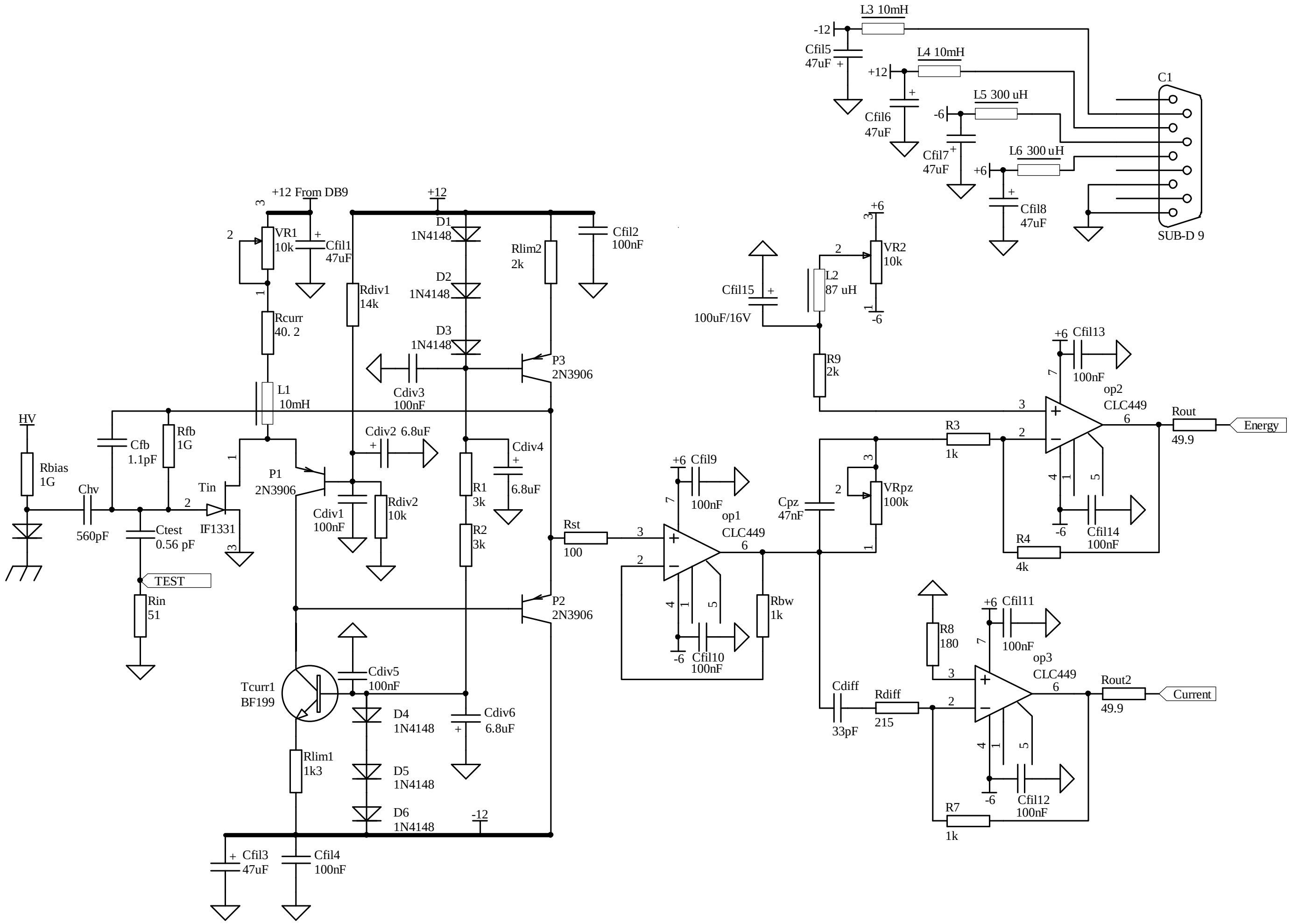

Figure A.1: Circuit diagram of the preamplifer designed in this project.

The operating point of the input FET determines the largest contribution to the total preamplifier noise. The dependence on the drain-source voltage is minimal and it was set at 5.5 V, based on the experience with the unsegmented CLUSTER preamplifiers. The optimal drain current varies from transistor to transistor and can be adjusted up to 45 mA. This maximum value enables the preamplifier to be connected to a variety of detector cryostats, from CLUSTER modules that employ FETs with optimal $I_{DS} \simeq 10\,\mathrm{mA}$ to smaller Ortec crystals ($I_{DS} \simeq 30\,\mathrm{mA}$). The total current for the input stage of the operational amplifier is provided by the potentiometer VR_2 and can be measured by determining the voltage drop on R_{curr}. The drain current of the FET is thus

$$I_{DS} = \frac{\Delta V_{R_{curr}}}{R_{curr}} - I_{C_1}\ . \tag{A.1}$$

From the active load,

$$I_{C_1} \simeq \frac{2 \cdot 0.65}{1.3}\ \mathrm{mA} = 1\,\mathrm{mA}\ . \tag{A.2}$$

The collector emitter voltage of P_1 is determined by the drain voltage of the FET and the output voltage of the integrating loop, according to $V_{C_1} = V_{GS} - 0.65$ V. In order to reduce its noise contribution, the FET is operated at maximal transconductance, resulting in $-100\,\mathrm{mV} \leq \mathrm{V_{E_2}} = \mathrm{V_{FB}} \leq 100\,\mathrm{mV}$ and thus in $V_{CE_1} \gtrsim 6.5\mathrm{V}$. When the detector is directly coupled to the gate of the input FET, $V_{FB} = V_{GS} + I_{Leakage} \cdot R_{fb}$, so that in order to prevent P_1 from saturating and T_{curr1} from dramatically reducing its equivalent output resistance ($V_{CE} > 1\,\mathrm{V}$), the voltage at the feedback connection must lie in the range $-9\,\mathrm{V} < V_{FB} < 4.5\,\mathrm{V}$. This offset is removed from the energy output by VR_2, whose output is filtered to avoid directly coupling the supply rails ripple to the output.

The differentiator is AC coupled, and the offset at the output of the charge sensitive loop is not coupled to the output. Due to the pulsed nature of the detector signals, there is however a small DC offset at the output of the differentiator immediately after a signal pulse occurs. The charge balance on both electrodes of

C_{diff} must be zero and after a positive pulse has been differentiated, a negative offset with a much longer time constant compensates the charge in the pulse.

The emitter follower P_2 also uses a current source (P_3) for biasing in order to avoid loading the cascode stage and at the same time allowing the output voltage to take any value in the range $(11.75-2\cdot0.65-1)\mathrm{V} \leq V_{FB} \leq (-11.75+V_{CE_{sat}})\mathrm{V}$, although the first stage only functions properly when $(4.5+0.65)\mathrm{V} \leq V_{FB} \leq (-9+0.65)\mathrm{V}$. The design value of $I_{C_1} = 750\ \mu\mathrm{A}$ reflects the compromise between the current gain of P_2 and the output impedance of P_3 (see section A.2). The input impedance of $op1$ is isolated from the gain stage only by the current gain of P_2. Hence, the buffer amplifier $op1$ has been selected for its high input impedance and large slew rate specification (2500 V/μs), essential for pulsed signals like those generated by germanium detectors.

A.2 The four AC stages

The input FET-bipolar stage with active load provides the full open loop gain of the operational amplifier in the charge sensitive preamplifier. The output stage of this operational amplifier consists of a buffer amplifier (P_2 and P_3). The integrated operational amplifiers $op1, 2, 3$ are used as a buffer, an inverting gain stage and a differentiator, respectively.

At the drain of the input FET, the emitter resistance of P_1 (r_{e_1}) and the total impedance towards the positive supply rail are connected in parallel, so that a fraction of i_{ds} is diverted from P_1. In order to reduce this fraction, the inductance L_1 should be as large as possible, but high current, high value inductors are far from ideal and have resonant frequencies much lower than the desired bandwidth. Of all tested types of high current 10 μH inductors, a satisfactory compromise was found in the Siemens Neosid Sd 75 type, whose resistance is 105 Ω. It is specified for a 48 mA maximum current and has a Q value of 40 at 100 kHz.

The gain of the discrete operational amplifier is, provided that negligible signal current flows through L_1, $A_{ol} \simeq -g_m \cdot (r_{o_1} \parallel r_{o_{curr1}})$, where g_m is the transconductance of the FET. The output resistance of a bipolar transistor can be calculated [Gra93] from

$$r_o = \frac{1}{g_m \cdot \eta} = \frac{\mathrm{V_A}}{\mathrm{I_C}} \ , \tag{A.3}$$

where g_m and η are the transistor transconductance and Early factor, I_C is the DC collector current and V_A is its Early voltage. The BF199 transistors were selected for the active load in preference over 2N3904s as a result of their larger Early voltage. The collector current I_{C_1} might initially be designed to minimise $r_{e_1} \simeq 26\,\mathrm{mV/mA}$, but then $r_{o_{\mathrm{curr1}}}$ would be reduced and thus also the open loop gain of the amplifier. All *pnp* transistors are of the 2N3906 type as a result of the low parasitic capacitance, reasonably high frequency cut-off frequency and large Early voltage.

In the *op*1 buffer, the high bandwidth of any operational amplifier having adequate slew rate, 1.2 GHz at $A_v = +2$ in the case of Commlinear's CLC449, recommends the inclusion of R_{st} *and* R_{bw} in order to remove high frequency oscillations. In the first prototype PCB of this circuit, oscillations at 912 and 425 MHz were observed before the shown values for R_{st} *and* R_{bw} were adopted.

The decay time constant of the integrated pulses, $\tau = \mathrm{R_{fb}} \cdot \mathrm{C_{fb}} = 1.1\,\mathrm{ms}$, is replaced by the shorter one, $\tau' = (R_3 \parallel R_{pz}) \cdot C_{pz} \simeq R_3 \cdot C_{pz} = 45\,\mu\mathrm{s}$. The use of a single potentiometer allows maintaining the original decay time constant, if desired. Deviations from the nominal values in the feedback components can be balanced by adjusting VR_{pz}. Furthermore, the range of time constants that can be compensated with this pole-zero cancellation network allows using the preamplifier with different "cold" PCBs, provided their decay time constants are shorter than 4.7 ms.

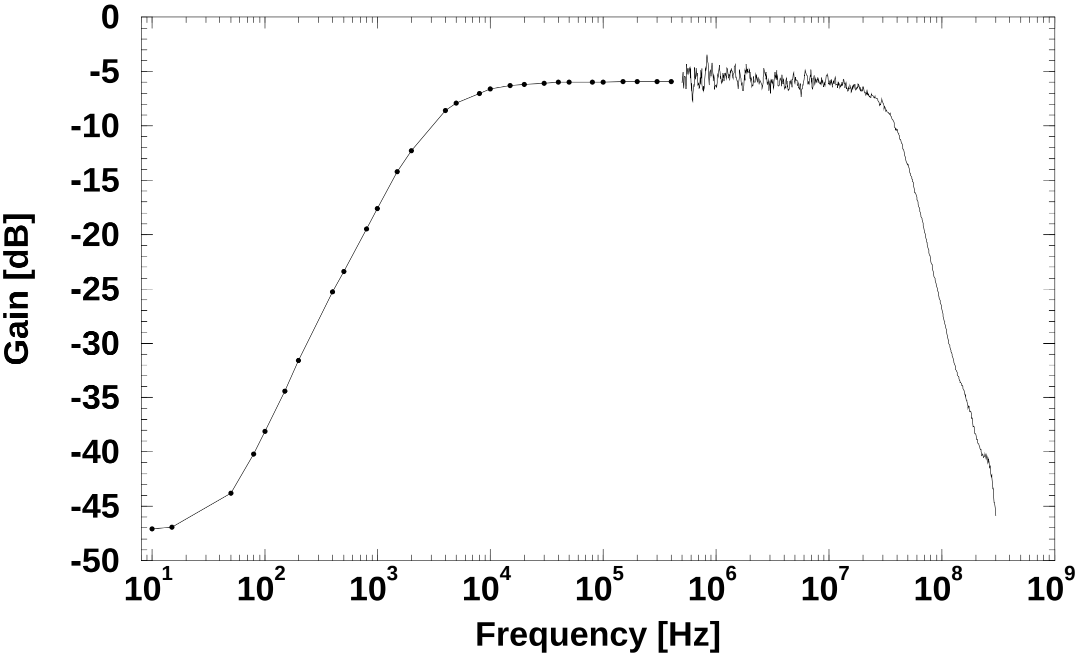

Figure A.2: Measured transfer function between the energy output and the test input with a room temperature FET. Above 500 kHz, a HP4396A network analyser was used to perform the measurement (at 3 kHz bandwidth) and no data points are indicated for clarity.

The DC offset present at the output of the buffered integrator is removed by adjusting VR_2. In order to filter the noise coupled from the power supply rails, an LC filter (L_2, $C_{fil_{15}}$) is included and the equivalent impedance is roughly matched by R_9.

The nominal gain between the test input and the energy output is 0.5 ($\frac{0.56\text{pF}}{1.1\text{pF}} \times \frac{2\text{k}\Omega}{1\text{k}\Omega} \times \frac{50\Omega}{2\times50\Omega}$) and the measured performance using a room temperature FET is shown in Fig. A.2. The frequency response is not constant at low frequencies due to the high-pass filter from the signal coupling capacitor C_{test}. The signal from the central detector electrode is AC coupled, but the coupling capacitance is 3 orders of magnitude larger (560 to 0.56 pF) and the frequency response correspondingly extends to lower frequencies.

The detector current pulse is recovered by differentiating the output of the

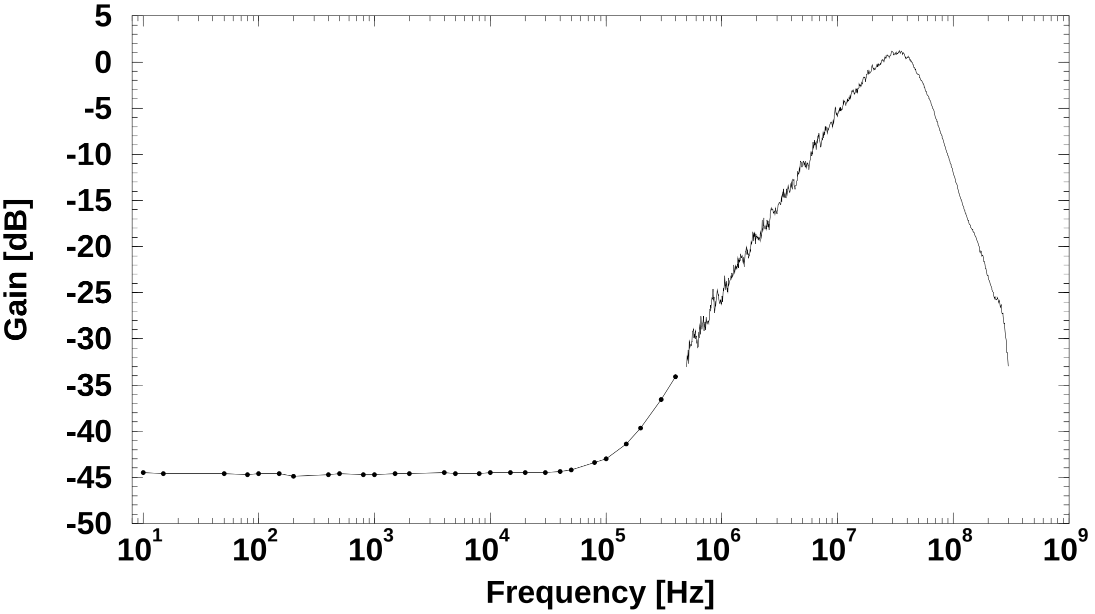

Figure A.3: Measured transfer function between the current output and the test input with a room temperature FET. Above 500 kHz, a HP4396A network analyser was used to perform the measurement (at 3 kHz bandwidth) and no data points are indicated for clarity.

buffered integrator. The virtual ground at the input of an operational amplifier is used to implement the desired transfer function

$$H(\omega) = \frac{R_7 C_{diff} j\omega}{1 + R_{diff} C_{diff} j\omega} \tag{A.4}$$

and the input signal is differentiated with time constant $R_{diff}C_{diff} = 7\,\mathrm{ns}$. Proper biasing of the non-inverting input of the current feedback operational amplifier is provided by R_8. Note that due to the pulse nature of the signals, C_{diff} introduces an offset at the output of the differentiator (see e.g. [Nic74]). Total charge on both C_{diff} electrodes must be zero after the signal pulse has ceased, resulting in a small, long time constant, negative amplitude DC offset at the output after a positive signal pulse. The measured frequency response between the current output and the test input (see Fig. A.3) shows close agreement with the predicted differentiation time constant. The fact that the test input is AC coupled influences the frequency response below 100 kHz.

A.3 Noise analysis

The noise contribution from the input FET above the noise corner frequency follows (see section 5.2.4)

$$\overline{S_{v_n}(f)} = 4kT\frac{2}{3}\frac{1}{g_m} \ . \tag{A.5}$$

The input-referred contribution from the rest of the preamplifier is

$$\begin{aligned} \overline{S_{v_{nr}}(f)} &= 2|e|(I_{B_1} + I_{B_{\mathrm{curr1}}} + I_{B_3})\frac{1}{g_m^2} + \\ &+\frac{4kT}{R_{lim1}}\frac{1}{g_m^2} + \frac{4kTr_{bb'_{\mathrm{curr1}}}}{R_{curr1}^2}\frac{1}{g_m^2} + \frac{4kTr_{bb'_1} + 4kTR_{curr_T}}{\mathrm{R}^2_{\mathrm{curr_T}}\left(1 - 4\pi^2 f^2\frac{\mathrm{L}_1^2}{\mathrm{R}^2_{\mathrm{curr_T}}}\right)}\frac{1}{g_m^2} \ , \end{aligned} \tag{A.6}$$

where I_B and $r_{bb'}$ are the base current and base spreading resistance of the respective transistor, g_m is the FET transconductance and R_{curr_T} is the total biasing resistance between L_1 and +12 V. The contribution from R_{lim_1} is comparable to the total contribution from the base currents. Assuming $r_{bb'} = 50\,\Omega$, the base spreading resistances do not contribute appreciably to the total spectral density.

The calculated equivalent input noise spectral density with a cold FET and assuming $g_m = 40\,\mathrm{mS}$ and $r_{bb'} = 50\,\Omega$ is shown in Fig. A.4. Despite being operated at 100 K, the largest contribution is due to the FET (eq. A.5), followed by the drain-source biasing network (R_{curr_T}, L_1), which is nevertheless more than a factor two smaller. The calculated noise spectral density could not be confirmed with a measurement. The −110 dBm input noise level for frequencies below 10 MHz of the best spectrum analyser (HP 4396) that could be used was higher than the noise level at the "charge" output of the preamplifier at the relevant frequency range.

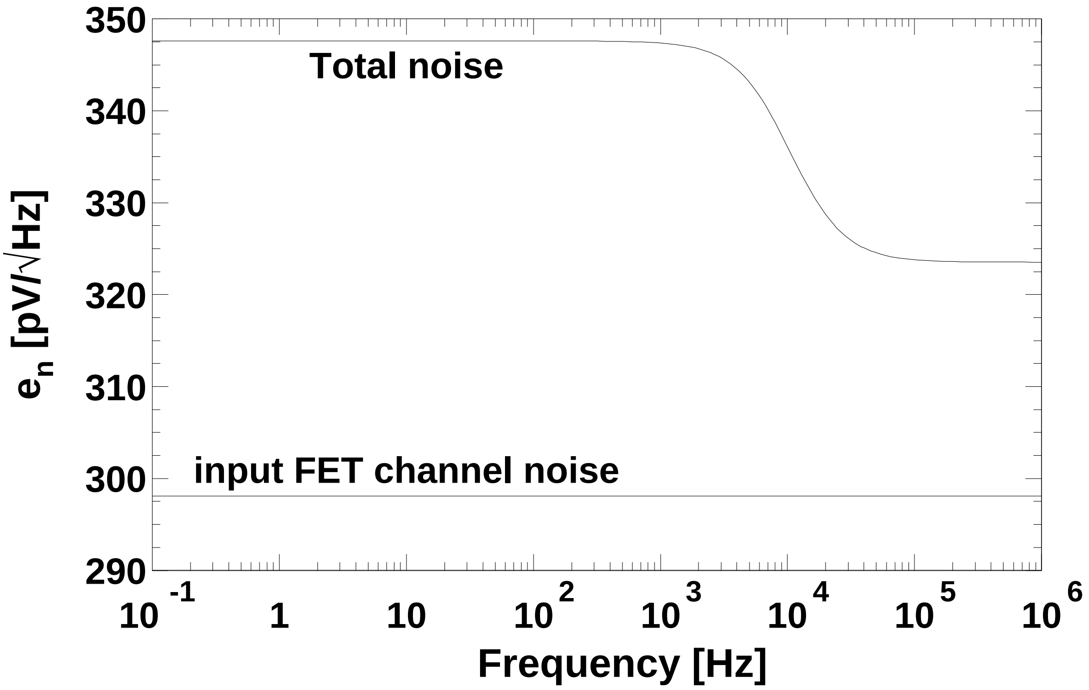

Figure A.4: Calculated equivalent input noise spectral density for the preamplifer. The contribution due to the equivalent FET noise resistance is also shown.

Appendix B

Source code of the computer programs

B.1 calculate_ E

```
#include <stdio.h>
#include <stdlib.h>
#include <string.h>
#include <math.h>

float phie[122][122][192];
float e_x[74][74][160],e_y[74][74][160],e_z[74][74][160];

float
gradient_x(int i, int j, int k, float weight1, float weight2)
{
  float result;
  result=weight1*(phie[i-1][j][k]-phie[i][j][k])+
         weight2*(phie[i][j][k]-phie[i+1][j][k]);
  return result;
}
float
gradient_y(int i, int j, int k, float weight1, float weight2)
{
  float result;
  result=weight1*(phie[i][j-1][k]-phie[i][j][k])+
         weight2*(phie[i][j][k]-phie[i][j+1][k]);
```

```
  return result;
}
float
gradient_z(int i, int j, int k, float weight1, float weight2)
{
  float result;
  result=weight1*(phie[i][j][k-1]-phie[i][j][k])+
         weight2*(phie[i][j][k]-phie[i][j][k+1]);
  return result;
}

void
vary_z(int i, int j, int fine_i, int fine_j, float dist1_x,
       float dist2_x, float dist1_y, float dist2_y)
{
  int k,fine_k;

  for(k=1;k<119;k++)
    {
      /*            fine_k=k; */
      /* 5000. is 0.5/1e-4 */
      e_x[i][j][k]=gradient_x(fine_i,fine_j,k,dist1_x,dist2_x);
      e_y[i][j][k]=gradient_y(fine_i,fine_j,k,dist1_y,dist2_y);
      e_z[i][j][k]=gradient_z(fine_i,fine_j,k,1000.,1000.);
    }
  e_x[i][j][119]=gradient_x(fine_i,fine_j,119,dist1_x,dist2_x);
  e_y[i][j][119]=gradient_y(fine_i,fine_j,119,dist1_y,dist2_y);
  e_z[i][j][119]=gradient_z(fine_i,fine_j,119,3.3333333e2,8.3333333e3);
  /* after the value for the non-equal distances have been */
  /* calculated, continue with the 0.1 mm spacing in z */

  for(k=120;k<127;k++)
    {
      fine_k=5*(k-119)+119;
      e_x[i][j][k]=gradient_x(fine_i,fine_j,fine_k,dist1_x,dist2_x);
      e_y[i][j][k]=gradient_y(fine_i,fine_j,fine_k,dist1_y,dist2_y);
      e_z[i][j][k]=gradient_z(fine_i,fine_j,fine_k,5000.,5000.);
    }
  e_x[i][j][127]=gradient_x(fine_i,fine_j,159,dist1_x,dist2_x);
  e_y[i][j][127]=gradient_y(fine_i,fine_j,159,dist1_y,dist2_y);
  e_z[i][j][127]=gradient_z(fine_i,fine_j,159,8.3333333e3,3.3333333e2);
  /* after the value for the non-equal distances have been */
  /* calculated, continue with the 0.5 mm spacing in z */

  for(k=128;k<158;k++)
```

```
    /* last point can't be calculated since the gradients */
    /* are calculated on both sides */
    {
      fine_k=k+32;
      e_x[i][j][k]=gradient_x(fine_i,fine_j,fine_k,dist1_x,dist2_x);
      e_y[i][j][k]=gradient_y(fine_i,fine_j,fine_k,dist1_y,dist2_y);
      e_z[i][j][k]=gradient_z(fine_i,fine_j,fine_k,1000.,1000.);
    }
  /* And this loop completes the z axis */
}

void
vary_yz(int i,int fine_i, float coeff1_x, float coeff2_x)
{
int j,fine_j;

for(j=1;j<13;j++)
/* j=13 is 6.0 mm, where the grid spacing becomes larger */
  {
    fine_j=5*(j-1)+1;
    vary_z(i,j,fine_i,fine_j,coeff1_x,coeff2_x,5000.,5000.);
  }
/* j=13; */
/* fine_j=61; */
/* corresponds to 6.0 mm, where the mesh starts its 0.5mm spacing */
vary_z(i,13,fine_i,61,coeff1_x,coeff2_x,8.3333333e3,3.3333333e2);
/* Now I have to loop in y (j) until its end */
for (j=14;j<72;j++)
  {
    fine_j=j+48;
    vary_z(i,j,fine_i,fine_j,coeff1_x,coeff2_x,1000.,1000.);
  }
/* And this loop completes the y axis */
}

main(int argc, char ** argv)
{
  FILE *eout, *phi_in;
/* coordinates run from 1 to 121, 1 to 121 and 1 to 191, all included */
  float x,y,z,data;
  char exstrng[100],eystrng[100],ezstrng[100],outstrng[200];
  char mafianame[100],outname[100];
  int i,j,k,l,fine_i,fine_j,fine_k;

/* The new mesh for mafia was:                               */
```

```
/* x in [0, 6] spacing 0.1 mm ; x in ]6,35] spacing 0.5 mm  */
/* y in [0, 6] spacing 0.1 mm ; y in ]6,35] spacing 0.5 mm  */
/* z in [0, 59] spacing 0.5 mm; z in ]59,63] spacing 0.1 mm;*/
/* z in ]63,78] spacing 0.5 mm;                             */
/* glitches were thus removed */

if (argc < 2 || argc > 3)
  {
    printf("usage: %s phifile fieldfile\n",argv[0]);
    printf("calculates the electric field corresponding to\n");
    printf("the potentials stored in phifile (mafia printout)\n");
    exit(1);
  }
strcpy(mafianame,argv[1]);
strcpy(outname,argv[2]);

phi_in = fopen (mafianame, "r");
if (phi_in==NULL)
  {
    printf("input file %d not found\n",mafianame);
    exit(1);
  }
eout = fopen (outname, "r");
if (eout!=NULL)
  {
    printf("output file %d already present\n",outname);
    exit(1);
  }
eout = fclose (outname);
eout = fopen (outname, "w");
fprintf(eout,"  index_x  index_y  index_z ex\
                                     ey          ez\n");

for(i=0;i<74;i++)
  {
    for(j=0;j<74;j++)
      {
        for(k=0;k<160;k++)
          {
            phie[i][j][k]=0.;
            e_x[i][j][k]=0.;
            e_y[i][j][k]=0.;
            e_z[i][j][k]=0.;
          }
      }
```

```
  }
/* clear the storing matrices before reading the voltage values */

  for(l=1;l<192;l++)
    /* l is the counter for the z axis */
  {
    do
      fgets(exstrng, 90, phi_in);
    while(strncmp(exstrng,"  ix  iy  iz ",12)!=0);
    /*Remove the header printed by mafia every time */
    /* a new block of data is printed */
       while (fscanf(phi_in," %d %d %d %f %f %f %f \n",
              &i,&j,&k,&x,&y,&z,&(data))==7)
    {
      phie[i][j][k]=data;
    }
  }
  /* The values for phie are now read into the matrix. */
  /* Note that there are empty  */
  /* positions, corresponding to the indeces [0][x][x], */
  /* [x][0][x], [x][x][0]      */
for(i=1;i<13;i++)
  {
    fine_i=5*(i-1)+1;
    vary_yz(i,fine_i,5000.,5000.);
  }
/* Now the border for x has to be dealt with */
vary_yz(13,61,8.3333333e3,3.3333333e2);
for(i=14;i<72;i++)
  {
    fine_i=i+48;
    vary_yz(i,fine_i,1000.,1000.);
  }
for(i=1;i<73;i++)
  {
    for(k=1;k<160;k++)
      {
        e_x[1][i][k]=0.;
        e_y[i][1][k]=0.;
      }
  }
for(i=1;i<73;i++)
  {
    for(j=1;j<73;j++)
      {
```

```
        e_z[i][j][1]=0.;
      }
  }
/* Clear the field components normal to the boundary surfaces */
  fprintf(eout,"\t Printout of the x y z E components on \
          a 0.5mm grid\n");
  fprintf(eout,"\t for a quarter cluster-crystal and rho=0\n");
  fprintf(eout," i j k Ex    Ey     Ez\n");
  fprintf(eout," int int int float\n");
  fprintf(eout,"  #\n");
  for(i=1;i<74;i++)
    {
      for(j=1;j<74;j++)
        {
          for(k=1;k<160;k++)
            {
              fwrite(&i,sizeof(int),1,eout);
              fwrite(&j,sizeof(int),1,eout);
              fwrite(&k,sizeof(int),1,eout);
              fwrite(&(e_x[i][j][k]),sizeof(float),1,eout);
              fwrite(&(e_y[i][j][k]),sizeof(float),1,eout);
              fwrite(&(e_z[i][j][k]),sizeof(float),1,eout);
            }
        }
    }
  close(eout);
  close(phi_in);
  exit(0);
}
```

B.2 r_ cut_ field

```
#include <stdio.h>
#include <stdlib.h>
#include <string.h>
#include <math.h>
#include <malloc.h>
#include <fnmatch.h>
#include <fcntl.h>
#include <sys/types.h>
#include <sys/time.h>
#include <sys/stat.h>
#include <unistd.h>
#define f2cFortran
```

```
#include "cfortran.h"

#define HLIMIT(LIMIT) \
      CCALLSFSUB1(HLIMIT,hlimit,INT,LIMIT)
#define HBOOK1(ID,CHTITLE,NX,XMI,XMA,VMX) \
   CCALLSFSUB6(HBOOK1,hbook1,INT,STRING,INT,FLOAT,FLOAT,FLOAT, \
         ID,CHTITLE,NX,XMI,XMA,VMX)
#define HBOOK2(ID,CHTITLE,NX,XMI,XMA,NY,YMI,YMA,VMX) \
  CCALLSFSUB9(HBOOK2,hbook2,INT,STRING,INT,FLOAT,FLOAT, \
              INT,FLOAT,FLOAT,FLOAT,ID,CHTITLE,NX,XMI,XMA,NY,YMI, \
              YMA,VMX)
#define HFILL(ID,X,Y,WEIGHT) \
   CCALLSFSUB4(HFILL,hfill,INT,FLOAT,FLOAT,FLOAT,ID,X,Y,WEIGHT)
#define HRPUT(ID,NAME,X)  CCALLSFSUB3(HRPUT,hrput,INT,STRING, \
        STRING,ID,NAME,X)
#define HRGET(ID,NAME,X)  CCALLSFSUB3(HRGET,hrget,INT,STRING, \
        STRING,ID,NAME,X)
#define HIJ(ID,I,J) CCALLSFFUN3(HIJ,hij,INT,INT,INT,ID,I,J)*/
#define HISTSIZE 3000000
struct pawc_ {
  int b[HISTSIZE];
  } pawc_;

FILE *ein,*pro;
int ff;
float e_x[74][74][160],e_y[74][74][160],e_z[74][74][160],
      e_mod[74][74][160];
float x,y,z,r;
float v_x,v_y,v_z;
float data_1,data_2,data_3;
char exstrng[100],outstrng[200];
char sourcename[1024],destname[1024],destfile[1024];
int max_i,max_j;
int tdrift;

main(int argc, char ** argv)
{
  int i,j,k,l,fine_i,fine_j,fine_k;
  float fl_i,fl_k;
  double intermed;
  FILE *fileptr;

  HLIMIT(HISTSIZE);

  if(argc < 2 || argc > 3)
```

```
{
  printf("usage: %s inputfile outputfile \n",argv[0]);
  printf("outputfile.hbook contains a 2D histogram \
          for the x=0, the y=0 cuts from inputfile\n");
  exit(1);
}
strcpy(sourcename,argv[1]);
strcpy(destname,argv[2]);
strcpy(destfile,destname);
strcat(destfile,".hbook");
printf ("Source %s\t Destination %s\n",sourcename,destfile);
if ((ff=open(sourcename,0))==-1)
  {
    printf("Source file %s not found. Exiting",sourcename);
    exit(1);
  }
for(i=1;i<74;i++)
  {
    for(j=1;j<74;j++)
      {
        for(k=1;k<160;k++)
          {
            e_x[i][j][k]=0.;
            e_y[i][j][k]=0.;
            e_z[i][j][k]=0.;
            e_mod[i][j][k]=0.;
          }
      }
  }
ein = fopen (sourcename, "r");
printf("Files opened\n");
do
  fgets(exstrng, 50, ein);
while(strncmp(exstrng,"  #",3)!=0);
/* Remove the header */
printf("Header removed\n");
while (fread(&i,sizeof(int),1,ein)==1)
  {
    fread(&j,sizeof(int),1,ein);
    fread(&k,sizeof(int),1,ein);
    fread(&(e_x[i][j][k]),sizeof(float),1,ein);
    fread(&(e_y[i][j][k]),sizeof(float),1,ein);
    fread(&(e_z[i][j][k]),sizeof(float),1,ein);
  }
/*  First I read the field matrix */
```

```
printf("field values read \n");
for(i=1;i<74;i++)
  {
    for(j=1;j<74;j++)
      {
        for(k=1;k<160;k++)
          {
            intermed=e_x[i][j][k]*e_x[i][j][k];
            intermed=intermed+e_y[i][j][k]*e_y[i][j][k];
            intermed=intermed+e_z[i][j][k]*e_z[i][j][k];
            e_mod[i][j][k]=(float)sqrt(intermed);
          }
      }
  }
HBOOK2(2,"Cut to hexagon corner",72,-0.25,35.75,160,-0.5,159.5,0);
HBOOK2(3,"Cut along tapered side",72,-0.25,35.75,160,-0.5,159.5,0);
HBOOK2(4,"E x, Cut to hexagon corner",72,-0.25,35.75,
       160,-0.5,159.5,0);
HBOOK2(5,"E y, Cut to hexagon corner",72,-0.25,35.75,
       160,-0.5,159.5,0);
HBOOK2(6,"E z, Cut to hexagon corner",72,-0.25,35.75,
       160,-0.5,159.5,0);
HBOOK2(7,"E z, Cut along tapered side",72,-0.25,35.75,
       160,-0.5,159.5,0);
for (i=1;i<74;i++)
  {
    j=200+i;
    k=300+i;
    HBOOK1(j," ",160,-0.5,159.5,0);
    HBOOK1(k," ",160,-0.5,159.5,0);
  }
for(i=1;i<74;i++)
  {
    for(k=1;k<160;k++)
      {
        fl_i=(float)(0.5*(i-1));
        fl_k=(float)(k);
        HFILL(2,fl_i,fl_k,e_mod[1][i][k]);
        HFILL(4,fl_i,fl_k,e_x[1][i][k]);
        HFILL(5,fl_i,fl_k,e_y[1][i][k]);
        HFILL(6,fl_i,fl_k,e_z[1][i][k]);
        HFILL(7,fl_i,fl_k,e_z[i][1][k]);
        /* Cut for x=0, should be the same histogram as 1 */
        /* 158-k is 159-(k-1) and is done so that the axis */
        /* comes at the front of the detector */
```

```
          HFILL((200+i),fl_k,0.,e_mod[1][i][k]);
          HFILL(3,fl_i,fl_k,e_mod[i][1][k]);
          /* Cut for y=0 */
          HFILL((300+i),fl_k,0.,e_mod[i][1][k]);
        }
    }
  HRPUT(0,destfile,"N");
  close(ein);
  exit(0);
}
```

B.3 z_ cut_ field

```
#include <stdio.h>
#include <stdlib.h>
#include <string.h>
#include <math.h>
#include <malloc.h>
#include <fnmatch.h>
#include <fcntl.h>
#include <sys/types.h>
#include <sys/time.h>
#include <sys/stat.h>
#include <unistd.h>
#define f2cFortran
#include "cfortran.h"

#define HLIMIT(LIMIT) \
      CCALLSFSUB1(HLIMIT,hlimit,INT,LIMIT)
#define HBOOK1(ID,CHTITLE,NX,XMI,XMA,VMX) \
   CCALLSFSUB6(HBOOK1,hbook1,INT,STRING,INT,FLOAT,FLOAT,FLOAT, \
         ID,CHTITLE,NX,XMI,XMA,VMX)
#define HBOOK2(ID,CHTITLE,NX,XMI,XMA,NY,YMI,YMA,VMX) \
  CCALLSFSUB9(HBOOK2,hbook2,INT,STRING,INT,FLOAT,FLOAT, \
              INT,FLOAT,FLOAT,FLOAT,ID,CHTITLE,NX,XMI,XMA,NY,YMI, \
              YMA,VMX)
#define HFILL(ID,X,Y,WEIGHT) \
   CCALLSFSUB4(HFILL,hfill,INT,FLOAT,FLOAT,FLOAT,ID,X,Y,WEIGHT)
#define HRPUT(ID,NAME,X)  CCALLSFSUB3(HRPUT,hrput,INT,STRING, \
        STRING,ID,NAME,X)
#define HRGET(ID,NAME,X)  CCALLSFSUB3(HRGET,hrget,INT,STRING, \
        STRING,ID,NAME,X)
#define HIJ(ID,I,J) CCALLSFFUN3(HIJ,hij,INT,INT,INT,ID,I,J)*/
#define HISTSIZE 3000000
```

```
#define r_min 19
#define r_max 26
#define r_step 1
/* These are all in mm, but int values. */
/* r_max is the maximum desired value + 1mm */
#define x_index_max 74
#define y_index_max 74
#define z_index_max 160

struct pawc_ {
  int b[HISTSIZE];
  } pawc_;

FILE *ein,*pro;
int ff;
float e_x[x_index_max][y_index_max][z_index_max],
      e_y[x_index_max][y_index_max][z_index_max],
      e_z[x_index_max][y_index_max][z_index_max];
/* float e_mod[x_index_max][y_index_max][z_index_max]; */
float data_1,data_2,data_3;
char exstrng[100],outstrng[200];
int max_i,max_j;

float
get_component(int i, int j, int k, float dist_x, float dist_y,
              float dist_z, float component_matrix[x_index_max]
              [y_index_max][z_index_max])
{
  float interpol[2][2], interpol_xy[2];
  float result;

  interpol[0][0]= dist_x*component_matrix[i+1][j][k] +
    (1.0-dist_x)*component_matrix[i][j][k];
  interpol[1][0]= dist_x*component_matrix[i+1][j+1][k] +
    (1.0-dist_x)*component_matrix[i][j+1][k];
  interpol[0][1]= dist_x*component_matrix[i+1][j][k+1] +
    (1.0-dist_x)*component_matrix[i][j][k+1];
  interpol[1][1]= dist_x*component_matrix[i+1][j+1][k+1] +
    (1.0-dist_x)*component_matrix[i][j+1][k+1];
  interpol[0][0]= dist_x*component_matrix[i+1][j][k] +
    (1.0-dist_x)*component_matrix[i][j][k];
  interpol[1][0]= dist_x*component_matrix[i+1][j+1][k] +
    (1.0-dist_x)*component_matrix[i][j+1][k];
  interpol[0][1]= dist_x*component_matrix[i+1][j][k+1] +
```

```
    (1.0-dist_x)*component_matrix[i][j][k+1];
  interpol[1][1]= dist_x*component_matrix[i+1][j+1][k+1] +
    (1.0-dist_x)*component_matrix[i][j+1][k+1];

  interpol_xy[0]= dist_y*interpol[1][0] + (1.0-dist_y)*interpol[0][0];
  interpol_xy[1]= dist_y*interpol[1][1] + (1.0-dist_y)*interpol[0][1];

  result= dist_z*interpol_xy[1] + (1.0-dist_z)*interpol_xy[0];

  return result;
}

main(int argc, char ** argv)
{
  int i,j,k,l,mesh_x,mesh_y,mesh_z;
  int histo,histo_new,r_counter,theta;
  FILE *fileptr;
  char sourcename[1024],destname[1024],destfile[1024];
  char name_cut[10],title[80];
  int ff;
  float x,y,z,cut,r,help;
  double theta_rad;
  float dist_x,dist_y,dist_z;
  float fl_i,fl_j,fl_theta,intermed;
  float e1,e2,e3,e_rad,value;

  HLIMIT(HISTSIZE);

  if(argc < 4 || argc > 5)
  {
    printf("usage: %s inputfile z[in mm] outputfile \
            histogram_id\n",argv[0]);
    printf("outputfile.hbook contains a 2D histogram for \
            the cut in z from inputfile\n");
    printf("plus 1000+id for the radial dependence on the \
            y=0 plane, \n");
    printf("2000+id for the radial dependence on the x=0 \
            plane and\n");
    printf("10000+id*100+radius for a scan in theta for radii \
            between %d and %d mm, in %d steps\n",r_min,r_max,r_step);
    exit(1);
  }
  strcpy(sourcename,argv[1]);
  z=(float)((atof(argv[2]))*1.e-3);
  strcpy(name_cut,"z=");
```

```
  strcat(name_cut,argv[2]);
  printf("cut for %s",name_cut);
  strcpy(destname,argv[3]);
  printf("hbook id: >>%s<<",argv[4]);
  histo=atoi(argv[4]);
  strcpy(destfile,destname);
  strcat(destfile,".hbook");
  printf ("Destination %s\n",destfile);
  if ((ff=open(sourcename,0))==-1)
    {
      printf("Source file %s not found. Exiting",sourcename);
      exit(1);
    }

  for(i=1;i<74;i++)
    {
      for(j=1;j<74;j++)
        {
          for(k=1;k<160;k++)
            {
              e_x[i][j][k]=0.;
              e_y[i][j][k]=0.;
              e_z[i][j][k]=0.;
/*            e_mod[i][j][k]=0.; */
            }
        }
    }
  ein = fopen (sourcename, "r");
  printf("Files opened\n");
  do
    fgets(exstrng, 50, ein);
  while(strncmp(exstrng,"  #",3)!=0);
  /* Remove the header */
  printf("Header removed\n");
  while (fread(&i,sizeof(int),1,ein)==1)
    {
      fread(&j,sizeof(int),1,ein);
      fread(&k,sizeof(int),1,ein);
      fread(&(e_x[i][j][k]),sizeof(float),1,ein);
      fread(&(e_y[i][j][k]),sizeof(float),1,ein);
      fread(&(e_z[i][j][k]),sizeof(float),1,ein);
    }
  /*  First I read the field matrix */
  printf("field values read \n");
```

```
  HBOOK2 (histo,name_cut,72,-0.25,35.75,72,-.25,35.75,0);
  HBOOK1 (1000+histo,"Along hexagonal side",72,-0.25,35.75,0);
  HBOOK1 (2000+histo,"Along tapered side",72,-0.25,35.75,0);

  mesh_z= (int)(2000.0*z)+1;
/* mesh_z is [z(in mm)] and the mesh starts counting at 1 */
  help= 2000.0*z;
/* help is an integer in value if z is on the 0.5mm mesh */
  dist_z= help - (float)(mesh_z - 1);
  for(i=1;i<72;i++)
    {
      fl_i=(float)(0.5*(i-1));
      for (j=1;j<72;j++)
        {
          fl_j=(float)(0.5*(j-1));
          e1=get_component(i,j,mesh_z,0.,0.,dist_z,e_x);
          e2=get_component(i,j,mesh_z,0.,0.,dist_z,e_y);
          e3=get_component(i,j,mesh_z,0.,0.,dist_z,e_z);
          value=sqrt(e1*e1+e2*e2+e3*e3);
          HFILL(histo,fl_i,fl_j,value);
          /* j-1, k-1 come from value[1] corresponding to 0 mm,*/
          /* 0.5 comes from 0.5 mm mesh */
        }
      e1=get_component(1,i,mesh_z,0.,0.,dist_z,e_x);
      e2=get_component(1,i,mesh_z,0.,0.,dist_z,e_y);
      e3=get_component(1,i,mesh_z,0.,0.,dist_z,e_z);
      value=sqrt(e1*e1+e2*e2+e3*e3);
      HFILL(1000+histo,fl_i,0.,value);
      e1=get_component(i,1,mesh_z,0.,0.,dist_z,e_x);
      e2=get_component(i,1,mesh_z,0.,0.,dist_z,e_y);
      e3=get_component(i,1,mesh_z,0.,0.,dist_z,e_z);
      value=sqrt(e1*e1+e2*e2+e3*e3);
      HFILL(2000+histo,fl_i,0.,value);
    }
  for(r_counter=r_min;r_counter<r_max;r_counter+=r_step)
    {
      r=r_counter*1.e-3;
      sprintf(title,"Radial component for r=%d mm",r_counter);
      histo_new=(int)(10000+(100*histo)+r_counter);
      HBOOK1(histo_new,title,901,-0.05,90.05,0);
      for(theta=0;theta<901;theta++)
      {
        fl_theta=(float)(theta/10.);
        theta_rad=(double)(fl_theta*(3.14159/180.));
        x=r*(float)(cos(theta_rad));
```

```
        y=r*(float)(sin(theta_rad));
        mesh_x= (int)(2000.0*x)+1;
/* mesh_x is [x(in mm)] and the mesh starts counting at 1 */
        help= 2000.0*x;
/* help is an integer in value if x is on the 0.5mm mesh */
        dist_x= help -(float)(mesh_x - 1);
        mesh_y= (int)(2000.0*y)+1;
/* mesh_y is [y(in mm)] and the mesh starts counting at 1 */
        help= 2000.0*y;
/* help is an integer in value if y is on the 0.5mm mesh */
        dist_y= help - (float)(mesh_y - 1);
        /* mesh_z and dist_z are already calculated */
        e1=get_component(mesh_x,mesh_y,mesh_z,dist_x,dist_y,
                         dist_z,e_x);
        e2=get_component(mesh_x,mesh_y,mesh_z,dist_x,dist_y,
                         dist_z,e_y);
        e_rad=sqrt((e1*e1)+(e2*e2));
        HFILL(histo_new,fl_theta,0.,e_rad);
      }
    }
    if ((ff=open(destfile,0))==-1)
    HRPUT(0,destfile,"N");
  else
    {
      close(ff);
      HRPUT(0,destfile,"U");
    }
  /* If file exists, append histograms */
  close(sourcename);
  exit(0);
}
```

B.4 t_ drift

```
#include <stdio.h>
#include <stdlib.h>
#include <string.h>
#include <math.h>

#define dt  1.0e-9
#define t_offset 10
FILE *exyz,*eout,*vout,*toute,*touth,*fout;
float e_x[74][74][160],e_y[74][74][160],e_z[74][74][160],
      e_int[74][74][160],e_modulus[13][13][160];
```

```
/* Checking the conditions for having reached the */
/* inner contact, E_modulus= 0 and/or v_drift=0 */
int t_drifte[74][74][160],t_drifth[74][74][160];
float field_x,field_y,field_z,field_mod,vel,pre_vel;
float x,y,z,r;
float v_x,v_y,v_z;
float data_1,data_2,data_3;
char exstrng[100],outstrng[200];
int i,j,k,l,fine_i,fine_j,fine_k;
int max_i,max_j;
int tdrifte,tdrifth;
int print1=0,print2=0;

void
get_e(float x, float y, float z, float *ex, float *ey, float *ez)
{
  int mesh_x,mesh_y,mesh_z,i_help;
  float help;
  float inter_x[2][2],inter_y[2][2],inter_z[4][2];
  float inter_xy_x[2],inter_xy_y[2],inter_xy_z[2];
  float dist_x,dist_y,dist_z;

  mesh_x= (int)(2000.0*x)+1;
/* mesh_x is [x(in mm)] and the mesh starts counting at 1 */
  help= 2000.0*x;
/* help is an integer in value if x is on the 0.5mm mesh */
  dist_x= help - (mesh_x -1);
  mesh_y= (int)(2000.0*y);
/* mesh_y is [y(in mm)] and the mesh starts counting at 1 */
  help= 2000.0*y;
/* help is an integer in value if y is on the 0.5mm mesh */
  dist_y= help - (mesh_y -1);
  mesh_z= (int)(2000.0*z);
/* mesh_z is [z(in mm)] and the mesh starts counting at 1 */
  help= 2000.0*z;
/* help is an integer in value if z is on the 0.5mm mesh */
  dist_z= help - (mesh_z -1);

  inter_x[0][0]= dist_x*e_x[mesh_x+1][mesh_y][mesh_z] +
                 (1.0-dist_x)*e_x[mesh_x][mesh_y][mesh_z];
  inter_x[1][0]= dist_x*e_x[mesh_x+1][mesh_y+1][mesh_z] +
                 (1.0-dist_x)*e_x[mesh_x][mesh_y+1][mesh_z];
  inter_x[0][1]= dist_x*e_x[mesh_x+1][mesh_y][mesh_z+1] +
                 (1.0-dist_x)*e_x[mesh_x][mesh_y][mesh_z+1];
  inter_x[1][1]= dist_x*e_x[mesh_x+1][mesh_y+1][mesh_z+1] +
```

```
                (1.0-dist_x)*e_x[mesh_x][mesh_y+1][mesh_z+1];
  /* Note that the indeces are related to the displacements */
  /* along the respective axes [disp_y][disp_z] */
  inter_xy_x[0]= dist_y*inter_x[1][0] + (1.0-dist_y)*inter_x[0][0];
  inter_xy_x[1]= dist_y*inter_x[1][1] + (1.0-dist_y)*inter_x[0][1];
  *ex= dist_z*inter_xy_x[1] + (1.0-dist_z)*inter_xy_x[0];

  inter_y[0][0]= dist_x*e_y[mesh_x+1][mesh_y][mesh_z] +
                (1.0-dist_x)*e_y[mesh_x][mesh_y][mesh_z];
  inter_y[1][0]= dist_x*e_y[mesh_x+1][mesh_y+1][mesh_z] +
                (1.0-dist_x)*e_y[mesh_x][mesh_y+1][mesh_z];
  inter_y[0][1]= dist_x*e_y[mesh_x+1][mesh_y][mesh_z+1] +
                (1.0-dist_x)*e_y[mesh_x][mesh_y][mesh_z+1];
  inter_y[1][1]= dist_x*e_y[mesh_x+1][mesh_y+1][mesh_z+1] +
                (1.0-dist_x)*e_y[mesh_x][mesh_y+1][mesh_z+1];
  /* Note that the indeces are related to the displacements */
  /* along the respective axes [disp_y][disp_z] */
  /* dist_x is 0.0 when x lies on the mesh */
  inter_xy_y[0]= dist_y*inter_y[1][0] + (1.0-dist_y)*inter_y[0][0];
  inter_xy_y[1]= dist_y*inter_y[1][1] + (1.0-dist_y)*inter_y[0][1];
  *ey= dist_z*inter_xy_y[1] + (1.0-dist_z)*inter_xy_y[0];

  inter_z[0][0]= dist_x*e_z[mesh_x+1][mesh_y][mesh_z] +
                (1.0-dist_x)*e_z[mesh_x][mesh_y][mesh_z];
  inter_z[1][0]= dist_x*e_z[mesh_x+1][mesh_y+1][mesh_z] +
                (1.0-dist_x)*e_z[mesh_x][mesh_y+1][mesh_z];
  inter_z[0][1]= dist_x*e_z[mesh_x+1][mesh_y][mesh_z+1] +
                (1.0-dist_x)*e_z[mesh_x][mesh_y][mesh_z+1];
  inter_z[1][1]= dist_x*e_z[mesh_x+1][mesh_y+1][mesh_z+1] +
                (1.0-dist_x)*e_z[mesh_x][mesh_y+1][mesh_z+1];
  /* Note that the indeces are related to the displacements */
  /* along the respective axes [disp_y][disp_z] */
  inter_xy_z[0]= dist_y*inter_z[1][0] + (1.0-dist_y)*inter_z[0][0];
  inter_xy_z[1]= dist_y*inter_z[1][1] + (1.0-dist_y)*inter_z[0][1];
  *ez= dist_z*inter_xy_z[1] + (1.0-dist_z)*inter_xy_z[0];
}

int
calculate_drift_times(float x,float y, float z,
                      int *t_drift_elec, int *t_drift_hole)
     /* Copied from calculate_current in pulses_3D.c */
     /* instead of calculating the current, it just */
     /* increments t every iteration */
     /* references to field_0 have been removed, since */
     /* the drift times are independent */
```

```
     /* Calculates the normalized current (charge = 1) */
     /* for position x,y,z */
     /* Returns the electron and hole currents in */
     /* e_current[pulse_length] and h_current */
{
#define e0e  27500.0/* Volt/m */
#define betae  1.32
#define muee   3.6 /* m^2/(V.s)*/
#define e0h  21050.0/* Volt/m */
#define betah  1.36
#define mueh   4.2 /* m^2/(V.s)*/

  float field_x,field_y,field_z,field_mod;
  float field_x_ini,field_y_ini,field_z_ini,field_mod_ini;
  float f_x,f_y,f_z,x1,y1;

  float x_ini,y_ini,z_ini;
  float v_x,v_y,v_z,pre_vel;
  float radius;
  int t;
  int outside=0,outside_z=0,outside_1=0,outside_2=0,
    outside_3=0,outside_4=0,outside_5=0;

  x_ini=x;
  y_ini=y;
  z_ini=z;
  get_e(x_ini,y_ini,z_ini,&field_x,&field_y,&field_z);
  field_mod= sqrt(field_x*field_x+field_y*field_y+field_z*field_z);

  field_x_ini=field_x;
  field_y_ini=field_y;
  field_z_ini=field_z;
  field_mod_ini=field_mod;

  radius=x*x+y*y;
  if (radius<1.96E-4)
    {
      if (radius>2.3E-5)
/* inside the cylinder where the contact is, leave things alone */
        {
          radius=sqrt(radius);
          x1=radius;
          y1=0.;
          get_e(x1,y1,z,&f_x,&f_y,&f_z);
        }
```

```
    }
  /* Copy all values, so they can be reused for the hole current */

  /* First calculate the electron current */
  t=t_offset;
  while ((field_mod >500.) && ((field_mod >100000.) ||
                               ((x*x+y*y)>3.E-05)) )
    /* Field has to be smaller than 1000V/cm, inside */
    /* the cylinder where the central contact is*/
    /* Should be a geometrical condition, but it would be */
    /* more complicated. The central contact is a cylinder, */
    /* but with the corner rounded off. */
    /* ie section is line,circle,line */
    {
      pre_vel= muee/pow((1+pow((field_mod/e0e),betae)),(1/betae));
      v_x= field_x*pre_vel;
      v_y= field_y*pre_vel;
      v_z= field_z*pre_vel;
/*       e_current[t]= (field0_mod/V_total)*(pre_vel*field_mod);  */
/*       e_current[t]= (pre_vel/V_total)*(field_x*field0_x+ */
/*                      field_y*field0_y+field_z*field0_z);  */
      /* induced current is proportional to the */
      /* scalar product of E(geom) and v_drift */
       if (print1)
         {
           fprintf(fout,"%1.3e %1.3e %1.3e %1.5e %1.5e \
                  %1.5e %1.5e %d\n",x,y,z,v_x,v_y,v_z,field_mod,t);
           fflush(fout);
         }
      x= fabs(x-v_x*dt);
      y= fabs(y-v_y*dt);
      z= fabs(z-v_z*dt);
      t++;
      get_e(x,y,z,&field_x,&field_y,&field_z);
      field_mod= sqrt(field_x*field_x+field_y*field_y+
                      field_z*field_z);
    }
  *t_drift_elec=t-t_offset;
  /* pass the value that will be used to fill the histogram */
  /* for the drift times of elctrons */
  /* Then calculate the hole current */
  x=x_ini;
  y=y_ini;
  z=z_ini;
  field_x=field_x_ini;
```

```
  field_y=field_y_ini;
  field_z=field_z_ini;
  field_mod=field_mod_ini;
  radius=x*x+y*y;
  if(radius<1.44E-4)
    {
      if(radius>2.304E-5)
/* inside the cylinder where the contact is, leave things alone */
        {
          radius=sqrt(radius);
          get_e(radius,0.,z,&f_x,&f_y,&f_z);
          field_x=(x/radius)*f_x;
          field_y=(y/radius)*f_x;
        }
    }
  t=t_offset;
  /* Restore initial values */
  if (z > 77.8E-3)
    outside_z=1;
  if ((x*x+y*y) > 1.21E-3)
    outside_1=1;
  /* r smaller than 34.8*34.8 mm */
  if (z> (-(13.9*x)+486.25E-3))
    outside_2= 1;
  /* z below the triangular section on the x axis */
  /* 13.9 = (78/(35-29.4)); 486.25E-3 = (77.8x35)/(35-29.4) */
  if (z> (-(13.9*(0.5*x+0.866*y))+486.25E-3))
    outside_3= 1;
  /* rotated by 60 Deg due to the symmetry */
  if (field_mod < 2.e2)
    outside_4 =1;
  /* otherwise, v_drift drops to 0 just before getting out */
  /* of the geometry */
  if ((x*x+y*y) > 4.0E-4)
    {
      if ((v_x<0.)||(v_y<0.))
        outside_5=1;
    }
  /* stops carriers moving in a circle, which was allowed */
  /* to happen without it. */
  /* radially, holes move outwards, so both velocities */
  /* must be positive     */
  outside= outside_z + outside_1 + outside_2 + outside_3 +
           outside_4 + outside_5;
  /* all conditions must be false to be outside of the detector */
```

```
  while (outside < 1)
    {
      pre_vel= mueh/pow((1+pow((field_mod/e0h),betah)),(1/betah));
      v_x= field_x*pre_vel;
      v_y= field_y*pre_vel;
      v_z= field_z*pre_vel;
/*       h_current[t]= (pre_vel/V_total)*(field_x*field0_x+ */
/*                      field_y*field0_y+field_z*field0_z); */
      /* induced current is proportional to the scalar product */
      /* of E(geom) and v_drift */
      if (print2)
        {
          fprintf(fout,"%1.3e %1.3e %1.3e %1.5e %1.5e \
                 %1.5e %1.5e %d\n",x,y,z,v_x,v_y,v_z,field_mod,t);
          fflush(fout);
        }
      x= fabs(x+v_x*dt);
      y= fabs(y+v_y*dt);
      z= fabs(z+v_z*dt);
      t++;
      get_e(x,y,z,&field_x,&field_y,&field_z);
      field_mod= sqrt(field_x*field_x+field_y*field_y+field_z*field_z);
      radius=x*x+y*y;

      if (z > 77.8E-3)
        outside_z=1;
      if ((x*x+y*y) > 1.21E-3)
        outside_1=1;
      /* r smaller than 34.8*34.8 mm */
      if (z> (-(13.9*x)+486.25E-3))
        outside_2= 1;
      /* z below the triangular section on the x axis */
      /* 13.9 = (78/(35-29.4)); 486.25E-3 = (77.8x35)/(35-29.4) */
      if (z> (-(13.9*(0.5*x+0.866*y))+486.25E-3))
        outside_3= 1;
      /* rotated by 60 Deg due to the symmetry */
      if (field_mod < 2.e2)
        outside_4 =1;
      /* otherwise, v_drift drops to 0 just before getting out */
      /* of the geometry */
      if ((x*x+y*y) > 4.0E-4)
        {
          if ((v_x<0.)||(v_y<0.))
            outside_5=1;
        }
```

```
      /* stops carriers moving in a circle, which was allowed */
      /* to happen without it. */
      /* radially, holes move towards the outer contact, */
      /* therefore both velocities */
      /* must be positive */

      outside= outside_z + outside_1 + outside_2 + outside_3 +
        outside_4 + outside_5;
    }/* all conditions must be false to be outside of the detector */
  *t_drift_hole=t-t_offset;
}

main(int argc, char ** argv)
{
int print = 0,print_all= 0,print_x=0,print_y=0,print_z=0;

  exyz = fopen ("egesamt.dat", "r");
  toute = fopen ("t_drifte.dat", "w");
  touth = fopen ("t_drifth.dat", "w");
  fout = fopen("t_drift.log","w");
  printf("Files opened\n");
  fprintf(toute,"  index_x  index_y  index_z  t_drift_electrons\n");
  fprintf(toute,"  All integer values, 1mm mesh distance \n");
  fprintf(toute,"  #\n");
  fprintf(touth,"  index_x  index_y  index_z  t_drift_holes\n");
  fprintf(touth,"  All integer values, 1mm mesh distance \n");
  fprintf(touth,"  #\n");
  fprintf(fout," i j  k   tdrifte  e_mod\n");

for(k=1;k<160;k++)
  {
    for(j=1;j<74;j++)
      {
        for(i=1;i<74;i++)
          {
            t_drifte[i][j][k]=-1;
            t_drifth[i][j][k]=-1;
          }
      }
  }
  do
    fgets(exstrng, 50, exyz);
  while(strncmp(exstrng,"  #",3)!=0);
  /* Remove the header */
  printf("Header removed\n");
```

```
  for(l=1;l<159;l++)
  /* l is the counter for the z axis. Mesh distance is 0.5 mm */
    {
      while (fread(&i,sizeof(int),1,exyz)==1)
        {
          fread(&j,sizeof(int),1,exyz);
          fread(&k,sizeof(int),1,exyz);
          fread(&(e_x[i][j][k]),sizeof(float),1,exyz);
          fread(&(e_y[i][j][k]),sizeof(float),1,exyz);
          fread(&(e_z[i][j][k]),sizeof(float),1,exyz);
        }
    }
  /*  First I read the E field components into the matrices */
  printf("Components read into e_x, e_y, e_z\n");
  for(i=1;i<73;i++)
    {
      max_j = (int)((sqrt(5476.0-(i*i)))+1.0) ;
      /*            5476 = 74*74 ;  */
      for(j=1;j<max_j;j++)
        {
          for(k=1;k<160;k++)
            {
              x=(i-1)*0.5e-3;
              y=(j-1)*0.5e-3;
              z=(k-1)*0.5e-3;
              calculate_drift_times(x,y,z,&tdrifte,&tdrifth);
              t_drifte[i][j][k]=tdrifte;
              t_drifth[i][j][k]=tdrifth;
              if (((i>19)&&(j>57))&&(print_z))
                {
                  fprintf(fout,"%d %d %d %d %f\n",i,j,k,
                          tdrifte,field_mod);
                  fflush(fout);
                }
            }
              if ((i>19)&&(print_y))
                printf("%d %d %d %d %f\n",i,j,k,tdrifte,field_mod);
        }
      if (print_x)
        printf("%d %d %d %d %f\n",i,j,k,tdrifte,field_mod);
    }

/*Write as binary file, in order to save space */
  for(i=1;i<74;i++)
```

```
    {
      for(j=1;j<74;j++)
        {

          for(k=1;k<160;k++)
            {
              fwrite(&i,sizeof(int),1,toute);
              fwrite(&j,sizeof(int),1,toute);
              fwrite(&k,sizeof(int),1,toute);
              fwrite(&(t_drifte[i][j][k]),sizeof(int),1,toute);
              fwrite(&i,sizeof(int),1,touth);
              fwrite(&j,sizeof(int),1,touth);
              fwrite(&k,sizeof(int),1,touth);
              fwrite(&(t_drifte[i][j][k]),sizeof(int),1,touth);
            }
        }
    }
  close(toute);
  close(touth);
  close(exyz);
  close(fout);
  exit(0);
}
```

B.5 pulses_ 3D

```
#include <stdio.h>
#include <stdlib.h>
#include <string.h>
#include <math.h>
#include <malloc.h>
#include <fnmatch.h>
#include <fcntl.h>
#include <sys/types.h>
#include <sys/time.h>
#include <sys/stat.h>
#include <unistd.h>
#define f2cFortran
#include "cfortran.h"

#define V_total 3500
#define max_interactions 15
#define pulse_length 550
#define t_offset 10
```

```
#define x_index_max 74
#define y_index_max 74
#define z_index_max 160

#define HLIMIT(LIMIT) \
      CCALLSFSUB1(HLIMIT,hlimit,INT,LIMIT)
#define HBOOK1(ID,CHTITLE,NX,XMI,XMA,VMX) \
   CCALLSFSUB6(HBOOK1,hbook1,INT,STRING,INT,FLOAT,FLOAT,FLOAT, \
         ID,CHTITLE,NX,XMI,XMA,VMX)
#define HBOOK2(ID,CHTITLE,NX,XMI,XMA,NY,YMI,YMA,VMX) \
  CCALLSFSUB9(HBOOK2,hbook2,INT,STRING,INT,FLOAT,FLOAT,INT, \
        FLOAT,FLOAT,FLOAT, ID,CHTITLE,NX,XMI,XMA,NY,YMI,YMA,VMX)
#define HFILL(ID,X,Y,WEIGHT) \
   CCALLSFSUB4(HFILL,hfill,INT,FLOAT,FLOAT,FLOAT,ID,X,Y,WEIGHT)
#define HRPUT(ID,NAME,X)  CCALLSFSUB3(HRPUT,hrput,INT,STRING, \
        STRING,ID,NAME,X)
#define HRGET(ID,NAME,X)  CCALLSFSUB3(HRGET,hrget,INT,STRING, \
        STRING,ID,NAME,X)
#define HNORMA(ID,XNORM) CCALLSFSUB2(HNORNMA,hnorma,INT,FLOAT,ID,XNORM)
#define HIJ(ID,I,J) CCALLSFFUN3(HIJ,hij,INT,INT,INT,ID,I,J)*/
#define HISTSIZE 5000000
struct pawc_ {
  int b[HISTSIZE];
  } pawc_;

FILE *exyz,*exyz0, *eout,*vout,*tout,*fout;
float e_x[x_index_max][y_index_max][z_index_max],
  e_y[x_index_max][y_index_max][z_index_max],
  e_z[x_index_max][y_index_max][z_index_max],
  e_int[x_index_max][y_index_max][z_index_max],
  e0_x[x_index_max][y_index_max][z_index_max],
  e0_y[x_index_max][y_index_max][z_index_max],
  e0_z[x_index_max][y_index_max][z_index_max],
  e_current[pulse_length],h_current[pulse_length],
  tot_current[pulse_length];
float field_x,field_y,field_z,field_mod,vel,pre_vel;
float field0_x,field0_y,field0_z,field0_mod;
float x,y,z,r;
float x_offset=0., y_offset=0.;
#define z_offset 8.17
/* offset in z, expressed in cm */
float v_x,v_y,v_z;
float data_1,data_2,data_3;
float intera_x[max_interactions],intera_y[max_interactions];
float intera_z[max_interactions],intera_e[max_interactions];
```

```
char extrnstrng[100],exstrng[100],outstrng[200],
  geantname[100],outname[100];
char dummy[20];
int tdrift;
int print = 0;
int print2= 0;
int  print_current_pulses=1,print_all_pulses=0;
/* 0 is false, 1 is true.
   Between 10 and 20 MB are needed for the hbook file */

float
get_component(int i, int j, int k, float dist_x, float dist_y,
              float dist_z, float component_matrix[x_index_max]
              [y_index_max][z_index_max])
{
  float interpol[2][2], interpol_xy[2];
  float result;

  interpol[0][0]= dist_x*component_matrix[i+1][j][k] +
    (1.0-dist_x)*component_matrix[i][j][k];
  interpol[1][0]= dist_x*component_matrix[i+1][j+1][k] +
    (1.0-dist_x)*component_matrix[i][j+1][k];
  interpol[0][1]= dist_x*component_matrix[i+1][j][k+1] +
    (1.0-dist_x)*component_matrix[i][j][k+1];
  interpol[1][1]= dist_x*component_matrix[i+1][j+1][k+1] +
    (1.0-dist_x)*component_matrix[i][j+1][k+1];
  interpol[0][0]= dist_x*component_matrix[i+1][j][k] +
    (1.0-dist_x)*component_matrix[i][j][k];
  interpol[1][0]= dist_x*component_matrix[i+1][j+1][k] +
    (1.0-dist_x)*component_matrix[i][j+1][k];
  interpol[0][1]= dist_x*component_matrix[i+1][j][k+1] +
    (1.0-dist_x)*component_matrix[i][j][k+1];
  interpol[1][1]= dist_x*component_matrix[i+1][j+1][k+1] +
    (1.0-dist_x)*component_matrix[i][j+1][k+1];

  interpol_xy[0]= dist_y*interpol[1][0] + (1.0-dist_y)*interpol[0][0];
  interpol_xy[1]= dist_y*interpol[1][1] + (1.0-dist_y)*interpol[0][1];

  result= dist_z*interpol_xy[1] + (1.0-dist_z)*interpol_xy[0];

  return result;
}

void
get_e(float x, float y, float z, float *ex, float *ey,
```

```
      float *ez, float *e0x, float *e0y, float *e0z)
{
  int mesh_x,mesh_y,mesh_z,i_help;
  float help;
  float dist_x,dist_y,dist_z;
  mesh_x= (int)(2000.0*x)+1;
  /* mesh_x is [x(in mm)] and the mesh starts counting at 1 */
  help= 2000.0*x;
  /* help is an integer in value if x is on the 0.5mm mesh */
  dist_x= help -(float)(mesh_x - 1);
  mesh_y= (int)(2000.0*y)+1;
  /* mesh_y is [y(in mm)] and the mesh starts counting at 1 */
  help= 2000.0*y;
  /* help is an integer in value if y is on the 0.5mm mesh */
  dist_y= help - (float)(mesh_y - 1);
  mesh_z= (int)(2000.0*z)+1;
  /* mesh_z is [z(in mm)] and the mesh starts counting at 1 */
  help= 2000.0*z;
  /* help is an integer in value if z is on the 0.5mm mesh */
  dist_z= help - (float)(mesh_z - 1);

  *e0x= get_component(mesh_x,mesh_y,mesh_z,dist_x,dist_y,dist_z,e0_x);
  *e0y= get_component(mesh_x,mesh_y,mesh_z,dist_x,dist_y,dist_z,e0_y);
  *e0z= get_component(mesh_x,mesh_y,mesh_z,dist_x,dist_y,dist_z,e0_z);
  *ex= get_component(mesh_x,mesh_y,mesh_z,dist_x,dist_y,dist_z,e_x);
  *ey= get_component(mesh_x,mesh_y,mesh_z,dist_x,dist_y,dist_z,e_y);
  *ez= get_component(mesh_x,mesh_y,mesh_z,dist_x,dist_y,dist_z,e_z);
}

int
remove_header(FILE *geantfile)
{
  int counter,i;
  counter=0;
  do
   {
     fgets(extrnstrng, 132, geantfile);
     counter++;
   }
  while((strncmp(extrnstrng,
               " ***** DATA CARD CONTENT      GEOM",34)!=0)&&
        (counter<200));
  if (counter == 200)
    return 1;
  sscanf(&(extrnstrng[34]),"%f %f",&x_offset,&y_offset);
```

```
  printf("offsets are: x %f\ty %f\n",x_offset,y_offset);
  do
   {
     fgets(extrnstrng, 132, geantfile);
     counter++;
   }
  while((strncmp(extrnstrng," *  ISTRA =",11)!=0)&&(counter<200));
  if (counter==200)
    return 1;
  /* remove all lines (hopefully shorter than 132 chars) */
  /*   until ISTRA comes */
  /* else come out with error code 1 */
  counter=0;/* reset */
  do
    {
      fgets(extrnstrng, 90,geantfile);
      counter++;
    }
  while((strncmp(extrnstrng," ********************",6)!=0)&&
        (counter<20));
  /*remove until the line with the asterisks */
  /* or 20 lines after that */
  if (counter==20)
    return 2;
  /*error code 2 if second part of the header not found */
  for (i=0;i<3;i++)
    fgets(extrnstrng, 90,geantfile);
  /* remove the three additional empty lines */
  return 0;
}

int
read_event(FILE *geantfile, float *intera_x, float *intera_y,
           float *intera_z, float *intera_e)
{
  int i,fehler,weg,len;
  char interaf[20];
  char line[133];

  for(i=0;i<max_interactions;i++)
    {
      fgets(line,132,geantfile);
      len=strlen(line);
      switch (len)
        {
```

```
        case 3:
          return (i);
          break;
        case 54:
          return -1;
          break;
        default:
          {
          sscanf(line,"%s %s NR %d X %f Y %f Z %f E %f",
                 interaf, dummy, &weg, &(intera_x[i]),
                 &(intera_y[i]),&(intera_z[i]),&(intera_e[i]));
          intera_x[i]=1e-2*(intera_x[i]-x_offset);
          intera_y[i]=1e-2*(intera_y[i]-y_offset);
          intera_z[i]=1e-2*(z_offset-intera_z[i]);
          /* Geant coordinates were in cm,*/
          /* change to m (SI) and correct for the offset*/
          /* detector in GEANT starts at 3.7 mm, stops at 81.7 mm */
          }
          break;
        }
    }
}

int
calculate_current(float x,float y, float z,
                  int *t_drift_elec, float *e_current,
                  float *h_current)
     /* Calculates the normalized current (charge = 1) */
     /* for position x,y,z */
     /* Returns the electron and hole currents in */
     /* e_current[pulse_length] and h_current */
{
#define e0e  27500.0/* Volt/m */
#define betae  1.32
#define muee   3.6 /* m^2/(V.s)*/
#define dt  1.0e-9
#define e0h  21050.0/* Volt/m */
#define betah  1.36
#define mueh   4.2 /* m^2/(V.s)*/

  float field_x,field_y,field_z,field_mod;
  float field0_x,field0_y,field0_z,field0_mod;
  float field_x_ini,field_y_ini,field_z_ini,field_mod_ini;
  float field0_x_ini,field0_y_ini,field0_z_ini;
  float f0_x,f0_y,f0_z,f0_r,f_x,f_y,f_z,x1,y1;
```

```
  float field0_mod_ini;

  float x_ini,y_ini,z_ini;
  float v_x,v_y,v_z,pre_vel;
  float radius;
  int t;
  int outside=0,outside_z=0,outside_1=0,outside_2=0,
    outside_3=0,outside_4=0,outside_5=0;

  x_ini=x;
  y_ini=y;
  z_ini=z;
  get_e(x_ini,y_ini,z_ini,&field_x,&field_y,&field_z,
        &field0_x,&field0_y,&field0_z);
  field_mod= sqrt(field_x*field_x+field_y*field_y+
                  field_z*field_z);

  field_x_ini=field_x;
  field_y_ini=field_y;
  field_z_ini=field_z;
  field_mod_ini=field_mod;
  radius=x*x+y*y;
  if (radius<1.96E-4)
    {
      if (radius>2.3E-5)
/* inside the cylinder where the contact is, leave things alone */
        {
          radius=sqrt(radius);
          x1=radius;
          y1=0.;
          get_e(x1,y1,z,&f_x,&f_y,&f_z,&f0_x,&f0_y,&f0_z);
          field0_x=(x/radius)*f0_x;
          field0_y=(y/radius)*f0_x;
        }
    }
  /* needed here to copy the proper values into _ini field0's */
  field0_x_ini=field0_x;
  field0_y_ini=field0_y;
  field0_z_ini=field0_z;
  /* Copy all values, so they can be reused for the hole current */

  /* First calculate the electron current */
  t=t_offset;
  while ((field_mod >500.) && ((field_mod >100000.) ||
                              ((x*x+y*y)>3.E-05)) )
```

```
    /* Field has to be smaller than 1000V/cm, inside the */
    /* cylinder where the central contact is. */
    /* Should be a geometrical condition, but it would */
    /* be more complicated. The central      */
    /* contact is a cylinder, but with the corner */
    /* rounded off. ie section is line,circle,line */
    {
      pre_vel= muee/pow((1+pow((field_mod/e0e),betae)),(1/betae));
      v_x= field_x*pre_vel;
      v_y= field_y*pre_vel;
      v_z= field_z*pre_vel;
      e_current[t]= (pre_vel/V_total)*(field_x*field0_x+
                     field_y*field0_y+field_z*field0_z);
      /* induced current is proportional to the */
      /* scalar product of E(geom) and v_drift */
      if (print)
        printf("%1.3e %1.3e %1.3e %1.5e \
               %1.5e %1.5e %1.5e %d\n",x,y,z,
               v_x,v_y,v_z,field_mod,t);
      x= fabs(x-v_x*dt);
      y= fabs(y-v_y*dt);
      z= fabs(z-v_z*dt);
      t++;
      get_e(x,y,z,&field_x,&field_y,&field_z,&field0_x,
            &field0_y,&field0_z);
      field_mod= sqrt(field_x*field_x+field_y*field_y+field_z*field_z);

      radius=x*x+y*y;
      if (radius<1.96E-04)
        {
          if (radius>2.304E-5)
/*inside the cylinder where the contact is, leave things alone */
            {
              radius=sqrt(radius);
              x1=radius;
              y1=0.;
              get_e(x1,y1,z,&f_x,&f_y,&f_z,&f0_x,&f0_y,&f0_z);
              field0_x=(x/radius)*f0_x;
              field0_y=(y/radius)*f0_x;
            }
        }
    }
  *t_drift_elec=t-t_offset;
  /* pass the value that will be used to fill */
  /* the histogram for the drift times of elctrons */
```

```
  /* Then calculate the hole current */
  x=x_ini;
  y=y_ini;
  z=z_ini;
  field_x=field_x_ini;
  field_y=field_y_ini;
  field_z=field_z_ini;
  field_mod=field_mod_ini;
  radius=x*x+y*y;
  if(radius<1.44E-4)
    {
      if(radius>2.304E-5)
/* inside the cylinder where the contact is, leave things alone */
        {
          radius=sqrt(radius);
          get_e(radius,0.,z,&f_x,&f_y,&f_z,&f0_x,&f0_y,&f0_z);
          field_x=(x/radius)*f_x;
          field_y=(y/radius)*f_x;
        }
    }
  field0_x=field0_x_ini;
  field0_y=field0_y_ini;
  field0_z=field0_z_ini;
  t=t_offset;
  /* Restore initial values */

  if (z > 77.8E-3)
    outside_z=1;
  if ((x*x+y*y) > 1.21E-3)
    outside_1=1;
  /* r smaller than 34.8*34.8 mm */
  if (z> (-(13.9*x)+486.25E-3))
    outside_2= 1;
  /* z below the triangular section on the x axis */
  /* 13.9 = (78/(35-29.4)); 486.25E-3 = (77.8x35)/(35-29.4) */
  if (z> (-(13.9*(0.5*x+0.866*y))+486.25E-3))
    outside_3= 1;
  /* rotated by 60 Deg due to the symmetry */
  if (field_mod < 2.e2)
    outside_4 =1;
  /* otherwise, v_drift drops to 0 just before */
  /* getting out of the geometry */
  if ((x*x+y*y) > 4.0E-4)
    {
```

```
      if ((v_x<0.)||(v_y<0.))
        outside_5=1;
    }
  /* stops carriers moving in a circle, */
  /* which was allowed to happen without it */
  /* radially, holes move outwards, so both velocities */
  /* must be positive */
  outside= outside_z + outside_1 + outside_2 +
    outside_3 + outside_4 + outside_5;
  /* all conditions must be false to be outside of the detector */

  while (outside < 1)
    {
      pre_vel= mueh/pow((1+pow((field_mod/e0h),betah)),(1/betah));
      v_x= field_x*pre_vel;
      v_y= field_y*pre_vel;
      v_z= field_z*pre_vel;
      h_current[t]= (pre_vel/V_total)*(field_x*field0_x+
                    field_y*field0_y+field_z*field0_z);
      /* induced current is proportional to the */
      /* scalar product of E(geom) and v_drift */
      if (print2)
        printf("%1.3e %1.3e %1.3e %1.5e %1.5e \
               %1.5e %1.5e %d\n",x,y,z,v_x,v_y,v_z,field_mod,t);
      x= fabs(x+v_x*dt);
      y= fabs(y+v_y*dt);
      z= fabs(z+v_z*dt);
      t++;
      get_e(x,y,z,&field_x,&field_y,&field_z,&field0_x,
            &field0_y,&field0_z);
      field_mod= sqrt(field_x*field_x+field_y*field_y+
                      field_z*field_z);
      radius=x*x+y*y;
      if (radius<1.96E-4)
        {
          if(radius>2.304E-5)
/* inside the cylinder where the contact is, leave things alone */
            {
              radius=sqrt(radius);
              get_e(radius,0.,z,&f_x,&f_y,&f_z,&f0_x,&f0_y,&f0_z);
              field0_x=(x/radius)*f0_x;
              field0_y=(y/radius)*f0_x;
            }
        }    /* needed to remove the spikes at t_offset */
```

```
      if (z > 77.8E-3)
        outside_z=1;
      if ((x*x+y*y) > 1.21E-3)
        outside_1=1;
      /* r smaller than 34.8*34.8 mm */
      if (z> (-(13.9*x)+486.25E-3))
        outside_2= 1;
      /* z below the triangular section on the x axis */
      /* 13.9 = (78/(35-29.4)); 486.25E-3 = (77.8x35)/(35-29.4) */
      if (z> (-(13.9*(0.5*x+0.866*y))+486.25E-3))
        outside_3= 1;
      /* rotated by 60 Deg due to the symmetry */
      if (field_mod < 2.e2)
        outside_4 =1;
      /* otherwise, v_drift drops to 0 just before getting out */
      /* of the geometry */
      if ((x*x+y*y) > 4.0E-4)
        {
          if ((v_x<0.)||(v_y<0.))
            outside_5=1;
        }
      /* stops carriers moving in a circle, */
      /* which was allowed to happen without it */
      /* radially, holes move towards the outer contact, */
      /* therefore both velocities must be positive */

      outside= outside_z + outside_1 + outside_2 + outside_3 +
        outside_4 + outside_5;
    }/* all conditions must be false to be outside of the detector */
}

int
maximum_drop( int delta_t, float *current)
{
int t,t_max_drop=0, t_max;
float max_drop=0., drop;

t_max= pulse_length- delta_t;
for(t=0;t<t_max;t++)
  {
    drop=current[t]-current[t+delta_t];
    if (drop >max_drop)
      {
        max_drop= drop;
        t_max_drop=t;
```

```
      }
  }
return t_max_drop;
}

int
time_to_exceed(float value, float vector[pulse_length])
{
int index;

for(index=0;index<pulse_length;index++)
  {
    if(vector[index]>value)
      {
        return index;
        break;
      }
  }
}

main(int argc, char ** argv)
{
FILE  *outfile, *geantfile, *logfile;
int ff;
int i,j,k,l;
int num_events, n_intera;
int t,t_max_drop,t_10,t_20,t_30,t_50,t_90,t_esche;
int histo_1[pulse_length],histo_4[pulse_length],
  histo_36[pulse_length], histo_drift_main[pulse_length],
  histo_t_max[pulse_length],histo_t_esche[pulse_length];
int histo_t_gerl[pulse_length][pulse_length];
int t_drift_e_main=0, t_drift_e=0,t_max=0;
float charge[pulse_length];
float ener_main=0.,event_energy,curr_max=0.,threshold=0.;
float weight,flnum_events,fl_t;
float drop,max_drop,old_current;
#define coeff 5.41182E-17
/* conversion from energy to charge. */
/*coeff = 1.6019E-19/2.96E-3 (because Egamma is in keV) */
float ele,hol;
char title[100],title1[100],title2[100];

HLIMIT(HISTSIZE);

if(argc < 2 || argc > 3)
```

```
  {
    printf("usage: %s geant_file\n",argv[0]);
    printf("reads the interactions from geant_file.txt \n");
    printf("calculates the corresponding current pulses\n");
    printf("and writes the histograms in geant_file.hbook\n");
    exit(1);
  }
strcpy(geantname,argv[1]);
strcpy(outname,argv[1]);
outname[strlen(outname)-4]='\0';
/*strip the .txt at the end of the geant file */
strcat(outname,".hbook");
printf("input file is:%s\t, output file %s\n",geantname,outname);
geantfile = fopen(geantname,"r");
exyz = fopen ("egesamt.dat", "r");
exyz0 = fopen ("egesamt0.dat", "r");

printf("Files opened\n");
do
  fgets(exstrng, 50, exyz);
while(strncmp(exstrng,"  #",3)!=0);
/* Remove the header */

for(l=1;l<z_index_max;l++)
  /* l is the counter for the z axis. Mesh distance is 0.5 mm */
  {
    while (fread(&i,sizeof(int),1,exyz)==1)
      {
        fread(&j,sizeof(int),1,exyz);
        fread(&k,sizeof(int),1,exyz);
        fread(&(e_x[i][j][k]),sizeof(float),1,exyz);
        fread(&(e_y[i][j][k]),sizeof(float),1,exyz);
        fread(&(e_z[i][j][k]),sizeof(float),1,exyz);
      }
  }
/*  First I read the E field components into the matrices */
close(exyz);

do
  fgets(exstrng, 50, exyz0);
while(strncmp(exstrng,"  #",3)!=0);
/* Remove the header */

for(l=1;l<z_index_max;l++)
  /* l is the counter for the z axis. Mesh distance is 0.5 mm */
```

```
  {
    while (fread(&i,sizeof(int),1,exyz0)==1)
      {
        fread(&j,sizeof(int),1,exyz0);
        fread(&k,sizeof(int),1,exyz0);
        fread(&(e0_x[i][j][k]),sizeof(float),1,exyz0);
        fread(&(e0_y[i][j][k]),sizeof(float),1,exyz0);
        fread(&(e0_z[i][j][k]),sizeof(float),1,exyz0);
      }
  }
/*  then I read the E(rho=0) field components into the matrices */
/* printf("E_0 components read into e_x, e_y, e_z\n"); */
close(exyz0);

remove_header(geantfile);
/* logfile= fopen("currents.log","w"); */
num_events=0;
HBOOK1(1,"Delta x=1",pulse_length,0.,(float)(pulse_length),0.);
HBOOK1(2,"Delta x=1",pulse_length,0.,(float)(pulse_length),0.);
HBOOK1(4,"Delta x=4",(int)(pulse_length/4.0),0.,
       (float)(pulse_length),0.);
HBOOK1(5,"Delta x=4",(int)(pulse_length/4.0),0.,
       (float)(pulse_length),0.);
/* HBOOK1(8,"Delta x=8",(int)(pulse_length/4.0),0.,
          (float)(pulse_length),0.); */
/* HBOOK1(12,"Delta x=12",(int)(pulse_length/4.),0.,
          (float)(pulse_length),0.); */
/* HBOOK1(16,"Delta x=16",(int)(pulse_length/4.),0.,
          (float)(pulse_length),0.); */
/* HBOOK1(20,"Delta x=20",(int)(pulse_length/4.),0.,
          (float)(pulse_length),0.); */
/* HBOOK1(24,"Delta x=24",(int)(pulse_length/4.),0.,
          (float)(pulse_length),0.); */
/* HBOOK1(28,"Delta x=28",(int)(pulse_length/4.),0.,
          (float)(pulse_length),0.); */
/* These all look the same, so I have commented them out */
HBOOK1(36,"Delta x=36",(int)(pulse_length/4.),0.,
       (float)(pulse_length),0.);
HBOOK1(37,"Delta x=36",(int)(pulse_length/4.),0.,
       (float)(pulse_length),0.);
HBOOK1(109,"t drift e from main interaction", pulse_length,0.,
       (float)(pulse_length),0.);
HBOOK1(110,"t drift e from main interaction",(int)(pulse_length/4.),
       0.,(float)(pulse_length),0.);
HBOOK1(200,"t max",pulse_length,0.,(float)(pulse_length),0.);
```

```
HBOOK1(201,"t max",(int)(pulse_length/4.),0.,(float)(pulse_length),0.);
HBOOK2(300,"t90 - t30",pulse_length,0.,(float)(pulse_length),
       pulse_length/2,0.,(float)(pulse_length/2),0.);
HBOOK2(301,"t90 - t30",(int)(pulse_length/4.),0.,
       (float)(pulse_length),(int)(pulse_length/8.),0.,
       (float)(pulse_length/2),0.);
HBOOK1(400,"t50 - t20",pulse_length,0.,(float)(pulse_length),0.);
HBOOK1(401,"t50 - t20",(float)(pulse_length/4.),0.,
       (float)(pulse_length),0.);
HBOOK1(350,"Charge vs event_num",5000.,0.,5000.,0.);
HBOOK1(351,"Error estimation",200.,0.5,1.5,0.);

for (t=0;t<pulse_length;t++)
  {
    histo_1[t]=0;
    histo_4[t]=0;
    histo_36[t]=0;
    histo_drift_main[t]=0;
    histo_t_max[t]=0;
    histo_t_esche[t]=0;
    for (i=0;i<pulse_length;i++)
      histo_t_gerl[t][i]=0;
  } /* clear all histograms, since they are only incremented */
do
  {
    /* loop that reads an event from geantfile and calculates */
    /* the corresponding current pulse  */

    /* First reset all variables that are used to store */
    /* the event data */

    for (j=0;j<max_interactions;j++)
      {
        intera_x[j]=0.;
        intera_y[j]=0.;
        intera_z[j]=0.;
        intera_e[j]=0.;
      }
    for (t=0;t<pulse_length;t++)
      {
        tot_current[t]=0.;
        e_current[t]=0.;
        h_current[t]=0.;
      }
    n_intera=0;
```

```
    ener_main=0.;
    event_energy=0.;
    t_max=0;
    curr_max=0.;
    /* All storing variables are clean */

    num_events++;
    if ((num_events<100)&&(print_current_pulses))
      {
        HBOOK1(num_events+500,"Current Pulse",pulse_length,
               -0.5,(float)(pulse_length)-0.5,0.);
        /* Define the histogram for the current pulses */
      }
    n_intera=read_event(geantfile, intera_x, intera_y,
                        intera_z, intera_e);
    for (i=0;i<n_intera;i++)
      {
        intera_x[i]=fabs(intera_x[i]);
        intera_y[i]=fabs(intera_y[i]);
        intera_z[i]=fabs(intera_z[i]);
        if ((print_current_pulses)&&(print_all_pulses)&&(num_events<15))
          {
            sprintf(title1,"Electron current  ");
            sprintf(title2,"Hole current  ");
            sprintf(title,"Energy %.3f, x %.3e, y %.3e z %.3e,\
interaction no. %d",intera_e[i],intera_x[i],intera_y[i],intera_z[i],i+1);
            strcat(title1,title);
            strcat(title2,title);
            HBOOK1(1000+(10*num_events)+i,title1,
                   pulse_length,-0.5,(float)(pulse_length)-0.5,0.);
            HBOOK1(2000+(10*num_events)+i,title2,
                   pulse_length,-0.5,(float)(pulse_length)-0.5,0.);
          }
      }
    for(i=0;i<n_intera;i++)
      {
        if ((intera_e[i]>0.03)&&(intera_z[i]<7.8e-2))
          {
        /* skip the interaction if the energy is */
           smaller than 0.03 keV or energy has been deposited
           in aluminium. In GEANT, photopeak events are defined
           as those that leave neraly the original energy in Ge.
           Agrees with the mesurable photopeak events, but
           calculate_current crashes if the starting point is
           outside the active volume of the detector */
```

```
        calculate_current (intera_x[i],intera_y[i],
                           intera_z[i], &(t_drift_e),
                           e_current, h_current);

        if( intera_e[i] > ener_main )
          {
            t_drift_e_main=t_drift_e;
            ener_main= intera_e[i];
          }
        /* check if the value returned by */
        /* calculate_current is the drift time of the */
        /* electrons for the main interaction */

        for (t=0;t<pulse_length;t++)
          {
            ele=coeff*intera_e[i]*e_current[t];
            hol=coeff*intera_e[i]*h_current[t];
            tot_current[t]= tot_current[t]+ ele + hol;
            if ((print_current_pulses)&&(print_all_pulses)&&
                (num_events<15))
              {
                HFILL(1000+(10*num_events)+i,(float)(t),0.,ele);
                HFILL(2000+(10*num_events)+i,(float)(t),0.,hol);
              }
            e_current[t]=0.;
            h_current[t]=0.;
          }
        event_energy=event_energy+intera_e[i];
      }
  }
/* after the event has been processed, */
/* increment the corresponding histograms */

t_max=0;
curr_max=tot_current[0];
/* Then I can use just one loop for detecting the */
/* maximum and integrating */
charge[0]=tot_current[0]*dt;
for(t=1;t<pulse_length;t++)
  {
    if ((num_events<100)&&(print_current_pulses))
      {
        HFILL((int)(num_events+500),(float)t,0.,
              (float)tot_current[t]);
```

```
          }
        if(tot_current[t]>curr_max)
          {
            curr_max=tot_current[t];
            t_max=t;
          }
        charge[t]=charge[t-1]+tot_current[t]*dt;
      }

    weight=(float)(charge[pulse_length-1]);
    if (num_events<5001)
        HFILL(350,(float)(num_events),0.,weight);
    if(event_energy!=0.)
      {
      weight=weight/(event_energy*coeff);
      HFILL(351,weight,0.,1.);
      }
    /* then calculate the times to exceed 20% */
    /* and 50% of the charge */
    threshold=0.1*charge[pulse_length-1];
    t_10=time_to_exceed(threshold,charge);
    threshold=0.3*charge[pulse_length-1];
    t_30=time_to_exceed(threshold,charge);
    threshold=0.9*charge[pulse_length-1];
    t_90=time_to_exceed(threshold,charge);
    histo_t_gerl[t_30-t_10][t_90-t_10]++;
    threshold=0.2*charge[pulse_length-1];
    t_20=time_to_exceed(threshold,charge);
    threshold=0.5*charge[pulse_length-1];
    t_50=time_to_exceed(threshold,charge);
    t_esche=t_50-t_20;
    histo_t_esche[t_esche]++;
    histo_t_max[t_max]++;
    histo_drift_main[t_drift_e_main]++;
    t_max_drop= maximum_drop(1,tot_current);
    histo_1[t_max_drop]++;
    t_max_drop= maximum_drop(8,tot_current);
    histo_4[t_max_drop]++;
/*     HFILL(1,(float)(t_max_drop),0.,1.); */
/*     t_max_drop= maximum_drop(4,tot_current); */
/*     HFILL(4,(float)(t_max_drop),0.,1.); */
/*     t_max_drop= maximum_drop(8,tot_current); */
/*     HFILL(8,(float)(t_max_drop),0.,1.); */
/*     t_max_drop= maximum_drop(12,tot_current); */
/*     HFILL(12,(float)(t_max_drop),0.,1.); */
```

```
/*     t_max_drop= maximum_drop(16,tot_current); */
/*     HFILL(16,(float)t_max_drop,0.,1.); */
/*     t_max_drop= maximum_drop(20,tot_current); */
/*     HFILL(20,(float)t_max_drop,0.,1.); */
/*     t_max_drop= maximum_drop(24,tot_current); */
/*     HFILL(24,(float)t_max_drop,0.,1.); */
/*     t_max_drop= maximum_drop(28,tot_current); */
/*     HFILL(28,(float)t_max_drop,0.,1.); */
    t_max_drop= maximum_drop(36,tot_current);
    histo_36[t_max_drop]++;
/*     HFILL(36,(float)t_max_drop,0.,1.); */

    /* and then process the next event */
  } while (-1<(n_intera));
/* until all events are processed */
printf ("%d Events processed from %s\n",num_events,geantname);

/* write the histograms, normalized */
flnum_events=(float)num_events;
for(t=0;t<pulse_length;t++)
  {
    fl_t=(float)(t);
    HFILL(1,fl_t,0.,(float)(histo_1[t]));
    weight= (float)(histo_1[t])/flnum_events;
    HFILL(2,fl_t,0.,weight);
    HFILL(4,fl_t,0.,(float)(histo_4[t]));
    weight= (float)(histo_4[t])/flnum_events;
    HFILL(5,fl_t,0.,weight);
    HFILL(36,fl_t,0.,(float)(histo_36[t]));
    weight= (float)(histo_36[t])/flnum_events;
    HFILL(37,fl_t,0.,weight);
    weight= (float)(histo_drift_main[t])/flnum_events;
    HFILL(109,fl_t,0.,weight);
    HFILL(110,fl_t,0.,weight);
    weight= (float)(histo_t_max[t])/flnum_events;
    HFILL(200,fl_t,0.,weight);
    HFILL(201,fl_t,0.,weight);
    weight= (float)(histo_t_esche[t])/flnum_events;
    HFILL(400,fl_t,0.,weight);
    HFILL(401,fl_t,0.,weight);
    for(i=0;i<pulse_length/2;i++)
      {
        weight= (float)(histo_t_gerl[i][t])/
          (flnum_events*flnum_events);
        HFILL(300,fl_t,(float)i,weight);
```

```
        HFILL(301,fl_t,(float)i,weight);
      }
  }
HNORMA(351,(float)(1.0));

 if ((ff=open(outname,0))==-1)
   HRPUT(0,outname,"N");
 else
   {
     close(ff);
     HRPUT(0,outname,"U");
   }
/* If file exists, append histograms */

close(geantfile);
close(logfile);
exit(0);
}
```